OPTOELECTRONIC DEVICES WITH 2D MATERIALS

Thesis

Submitted in partial fulfilment of the requirements for the degree of

DOCTOR OF PHILOSOPHY

by

SANGEETH KALLATT

DEPARTMENT OF PHYSICS
NATIONAL INSTITUTE OF TECHNOLOGY KARNATAKA,
SURATHKAL, MANGALORE – 575 025

October, 2017

DECLARATION

I hereby *declare* that the Research Thesis entitled **"Optoelectronic devices with 2D materials"** which is being submitted to the National Institute of Technology Karnataka, Surathkal in partial fulfillment of the requirements for the award of the **Degree of Doctor of Philosophy** in **Physics** is *a bonafide report of the research work carried out by me*. The material contained in this Research Thesis has not been submitted to any University or Institution for the award of any degree.

Mr. Sangeeth Kallatt

(Reg. No. 135030PH13P03)

Department of Physics

Place: NITK, Surathkal

Date: October 17, 2017

CERTIFICATE

This is to *certify* that the Research Thesis entitled **"Optoelectronic devices with 2D materials"** submitted by Sangeeth Kallatt (Register Number135030PH13P03) as the record of the research work carried out by him, is accepted as the *Research Thesis* submission in partial fulfillment of the requirements for the award of degree of Doctor of Philosophy.

Prof. Navakanata Bhat
Research Guide

Prof. G. Umesh
Research Guide

Chairman-DRPC

Acknowledgments

Firstly, I would like to express my deep sense of gratitude towards my research advisor, Prof. G. Umesh, for all his support and guidance over the last 4 years. He has been always available, and I have received a tremendous amount of advice from him. He has given me enough freedom to choose the topic of research. I sincerely acknowledge all his efforts to patiently correct this thesis.

I would like to thank my co-advisor, Prof. Navakanta Bhat, for being such an inspiring personality and constant source of motivation throughout this period.

I would like to thank Prof. Kausik Majumdar for all the technical discussions. I also acknowledge all his efforts in spending long hours in the lab to help me in the measurements. I am grateful to my research committee members, Dr. Laxminidhi and Dr. M. N. Satyanarayana for their suggestions for improving the quality of work. I would like to extent my thanks towards Prof. K. N. Bhat, Prof. Digbijoy Nath, Prof. M. M. Nayak and Prof. S. Mohan for the technical discussions. I would like to thank Dr. Vijayaraghavan, Dr. Prabhakar Rao, R. Dwarakanathan and Dr. TUMS Murthy for keeping me motivated throughout.

I am also greatly indebted to my colleagues at Department of Physics, NITK for their support throughout.

I am fortunate to work with a bunch of wonderful colleagues at CeNSE. I would like to acknowledge all my colleagues at NNFC and MNCF. I am grateful to Smitha Nair for being a best friend and colleague throughout. I also would like to acknowledge Pandyan for all the help I received in wire bonding.

I would like to express my gratitude to my wife Sreedevi Korappilly for taking care of our family affairs. I wasn't home most of the time and she was understanding about it. In my absence, she had to bring up our child almost alone.

I would like to express my gratitude to my family members for raising me quietly.

Lastly, I would like to thank all the other known or unknown factors in this world, which helped me in this pursuit of knowledge.

ABSTRACT

This thesis reports various optoelectronic properties of Transition Metal Dichalcogenides (TMDs) such as MoS_2, WS_2 WSe_2 and $MoSe_2$, Photoluminescence (PL) spectra of these materials were investigated in detail using linearly polarized laser beam as the excitation source. The PL spectrum shows few broad peaks and a large number of sharp Raman-peaks, close to the excitation wavelength. It is seen that the peaks close to the excitation wavelength are sensitive to the relative orientation of the plane of polarization of the laser light, wherein the change in the intensity of such peaks is as high as 40% as the plane of polarization is changed from vertical to horizontal. From the analysis of PL spectra, the temperature of the charge carriers in the TMD films has been estimated. Photoconductivity measurements on these materials indicated that MoS_2 has the highest electrical conductivity. Hence, the photo-response of MoS_2 based heterojunction photo-detectors was investigated extensively. To study the photoresponse from MoS_2 devices, two terminal devices were fabricated using nanofabrication techniques. Devices of uniform channel thickness and varying channel thickness (heterojunction) were fabricated. Photocurrent mapping, over the device surface, was done by scanning a laser beam across the device together with the electrical measurements. In devices with uniform channel thickness, the photocurrent is seen to be maximum when the laser beam is incident on the edge of the source electrode (metal) of the device. This suggests injection of hot electrons from metal to MoS_2 film thereby generating the photocurrent. Heterojunction devices showed maximum current generation when the laser beam was incident at the junction separating mono-layer and multi-layer zones of the MoS_2 film. It is also seen to depend on the magnitude of the bias voltage which may be understood on the basis of band offset at the junction. In this context, various other photocurrent generation mechanisms have been considered to understand the device performance. Heterojunction devices were made by combining a bi-layer or few-layer or many layer MoS_2 along with a mono-layer MoS_2. Photo-response measurements on these devices revealed that the speed of photo detection was highest in devices having multi-layers. Response time up to 26ms was obtained for such devices as against a few sec for the device made using mono-layer alone. The mechanism of charge transfer from metal electrode to the MoS_2 device was also studied. The amount of charge transfer at the metal-MoS_2 junction was studied using Kelvin Probe Force Microscopy for gold and nickel metals as electrodes. At higher gate bias, these devices show nearly zero potential barrier, wherein the contact resistance is limited by the air gap between metal and 2D layer. Based

on these investigations a new model has been proposed for the barrier formation at metal-TMDs junction and thereby understand the nature of contact resistance. These studies have been exploited for proposing a better structure for photodetectors based on TMDs.

Keywords: 2D materials, MoS_2, photoluminescence, Valleytronics, hot electron transfer, in-plane heterojunction, photodetectors, charge transfer, contact resistance, Schottky barrier.

Contents

NOMENCLATURE

AFM	Atomic Force Microscopy
Al	Aluminium
Au	Gold
Cr	Chromium
E_c	conduction band
E_F	Fermi energy
E_g	band gap
eV	electron volt
E_v	valence band
FWHM	Full Width Half Maximum
I_{ds}	Drain current
K_B	Boltzmann constant
KPFM	Kelvin Probe Force Microscopy
LCP	Left Circularly Polarized
Mo	Molybdenum
MoS_2	Molybdenum Disulphide
$MoSe_2$	Molybdenum Diselenide
MSM	Metal Semiconductor Metal
Ni	Nickel
PDMS	Polydimethylsiloxane
PL	Photoluminescence
q	Electronic charge
RCP	Right Circularly Polarized
SEM	Scanning Electon Microscopy
STM	Scanning Tunneling Microscopy
TLM	Transfer Length Measurements
TMD	Transition metal Dichalcogenide
TMDs	Transition metal Dichalcogenides

V	Voltage
V_g	Gate voltage
W	Tungsten
WS_2	Tungsten Disulphide
WSe_2	Tungsten Disulphide
XPS	X-ray Photoemission Spectroscopy

CHAPTER 1

INTRODUCTION

Overview:

Chapter 1 presents a brief overview of the two dimensional materials and their various properties. Electrical and optical properties of two dimensional materials are discussed in detail. Further, the important parameters which influences the two dimensional material based photodetectors are also discussed. These is a section on the present status of these devices and the challenges. Lastly, the scope and objectives of the thesis are presented followed by a summary of all the chapters in the thesis.

1. Introduction:

Microelectronic devices and systems have undergone a sea-change over the last 5 decades in tune with the famous Moore's Law. Technology has now reached the 10nm domain and further miniaturization is encountering limitations dictated by Quantum Physics. Nano-materials and nanotechnology have provided avenues for ultimate miniaturization of devices. In this context, the simplest nanoscale materials are 2-D materials and have a significant role to play due to their extraordinary physical properties(Koppens et al. 2014). The fact that such materials have a one atom thick planar structure, leads to physical properties which are fully governed by quantum mechanics. The possibility of fabricating ultra-thin channels in TFT devices results in greater gate control over the channel barrier and also, to reduced short-channel effects(Zhang 2015). Si based electronic devices show poor performance when channel lengths are reduced below 10nm due to quantum mechanical tunneling and other effects due to short channel. Hence, there is a need for new materials that can either replace silicon or compatible with silicon(Chen 2016). Apart from 2D materials, many other materials, including nanowires, Graphene, carbon nanotubes, etc., are also being explored(Sun and Chang 2014). While each of these materials have their advantages and disadvantages, the 2D materials deserve special attention because of the ease of preparation, integration with Silicon Technology, planar device architecture, higher current carrying capacity, very good mechanical properties, favorable electro-optic properties, etc.(Wang et al. 2012a Fiori et al. 2014 Xia et al. 2014).

Bulk 2D materials occur in nature as a very large number of atomically thin layers stacked over each other. Although the atoms within a layer are connected by very strong covalent bonds, the neighboring layers interact through the very weak Van der Waal's force. Be-

cause of this, 2D materials are also called Van der Waal's solids. Since the interlayer coupling between these layers in two dimensional materials is very week, they can be removed from each other without much difficulty either mechanically or chemically(Huang et al. 2015). Graphene was the first 2D material discovered in 2004 by Nobel Laureates Konstantin Novoselov and Andre Geim. Recently, group of new two dimensional materials having the same bonding nature as Graphene, have also been invented. They are generally called Transition Metal Dichalcogenides (TMDs). Unlike the case of Graphene, where only Carbon atoms are present in the crystal lattice, TMDs are made of one atom of a transition metal and two atoms of a chalcogen. Apart from TMDs, many other types of 2D materials such as hexagonal Boron nitride, perovskite based 2D materials etc. are also being investigated (Bhimanapati et al. 2015).

In these two dimensional materials, charge carriers are subject to a strong quantum confinement, which arises due to their ultra-small dimensions. This also which leads to many extra-ordinary properties in these materials even in ambient conditions, which cannot be observed in other materials(Navarro-Moratalla and Jarillo-Herrero 2016). This made the research community around the globe to actively explore the new possibilities of device fabrication with two dimensional materials. A variety of techniques have emerged for the preparation of 2D materials and also for their characterization in terms of electrical, optical, thermal and mechanical properties. Procedures have also evolved for the fabrication of devices, including multi-layer heterostructures, using such materials (Duan et al. 2015 Yuan et al. 2015).

Graphene has occupied the lead position among the new branch of two dimensional materials. It is a monolayer of Carbon atoms arranged in the shape of a honey comb lattice. Different carbon atoms in the lattice are connected to each other by the covalent bonding between sp^2- hybridized orbitals. The remaining $p_z$orbitals, which are out of plane orbitals, can function as a path for electron hopping. Because of this peculiar band structure, the free electrons in monolayer Graphene has a zero rest mass and hence, it behaves as a massless Fermions. The energy dispersion curve is a straight line for a monolayer Graphene with energy of carriers directly proportional to the wave number of the electron. Such fermions are called Dirac fermions and behave like massless particles in Graphene. Consequently, such electrons possess very high mobility. For example, a single Graphene layer, suspended in air, has a carrier mobility of as high as $10^6 cm^2V^{-1}S^{-1}$at temperature of 2K. Graphene has zero band gap and is semi-metallic in nature. Though it is very thin as a monolayer (≈35Å),

Graphene is highly impermeable and chemically stable. These properties led to the use of Graphene in various devices, including FET, photo-detectors, gas sensors, bio sensors etc.(Mueller et al. 2010 Akinwande et al. 2014). However, the zero band gap character of Graphene has been a disadvantage in several other applications such as switching transistors which have high stand by power consumption.

In contrast to Graphene, two dimensional flakes of Transition Metal Dichalcogenides possess appreciable band gap even though they have crystal structure similar to that of Graphene. The band gap of these materials are not constant always. It changes its value, depending on the nature of the Transition metal, number of layers in the material etc. It is worth noting that different TMDs have different band gaps which gives us the freedom of selecting the TMD material most appropriate for any specific application. Thus there is tremendous interest in exploiting TMDs in a variety of device applications.

TMDs have the general formula MX_2, where M stands for a transition metal (like Mo, W, Ta, Sn, Nb etc.) and X strands for a chalcogen (such as S, Se, Te etc.). Despite having the same empirical relation, different TMDs have very different physical properties. MoS_2 is one of the most widely studied TMD materials. It exhibits a band gap that varies with the layer thickness, which is the same for most of the TMDs. Moreover, a MoS_2 monolayer is a direct band gap material whereas a multi-layer MoS_2 film is an indirect band gap semiconductor. Monolayer TMDs have honey comb lattice with a layer thickness of $\approx$ 0.75nm (Padilha et al. 2014). Remarkably, such a thin layer absorbs almost10% of light incident on it which is rather unexpected (Mak et al. 2010). Hence, there is a great potential for employing TMDs in photodetectors, solar cells etc.(Pospischil et al. 2014). The Brillouin zone of TMDs is hexagonal with 6 nodes. Each node is called a "valley". Valleys in the TMDs monolayer, especially, show some special properties, which comes from the spin orbit coupling and associated valence band energy splitting. It has been shown that the transport of charge carriers into and out of these valleys can be controlled by applying a bias voltage(Yu et al. 2015). This possibility has enabled us to store information in such quantum states, which has opened up the new field called "Valleytronics". Thus, TMDs are seen to have the potential to function as atomically thin transistors, vertical tunnel transistor, vertical field effect transistor etc.(Han et al. 2011 Li et al. 2015). Hence, a detailed study of the band structure of TMD and their electronic and optoelectronic properties is vital(Lin et al. 2014).

1.1 Crystal structure of TMDs

The MoS_2 bulk unit cell belongs to the space group $P6_3/mmc$. It contains a total of 6 atoms, out of which 2 are Molybdenum (Mo) atoms and 4 are Sulphur (S) atoms. The hexagonal lattice constants for MoS_2 unit cell are a = 3.122Å and c = 11.986Å, the Mo–S bond length, d_{Mo-S} , is 2.383 Å and the Mo-Mo bond length,d_{Mo-Mo}, is 6.19Å. The S–S separation (3.11Å) in MoS_2 is considerably larger than the S-S bond length d_{S-S} = 1.89 Å in S_2 dimer The values of 'a' and d_{Mo-S} are seen to be independent of the number of layers, the variation being less than 5×10^{-3}Å. On account of this, as the number of layers increases the band gap gets reduced and also tends towards indirect band gap type (Kadantsev and Hawrylak 2012 Padilha et al. 2014).

Figure 1.1(a) shows the crystal structure of MoS_2 as seen from top and Fig. 1.1(b) shows the corresponding Brillouin Zone. Fig. 1.1 (c) shows the edge-on view of a three-layer stack of MoS_2 . The MoS_2 monolayer may be looked upon as consisting of a plane formed by Mo atoms sandwitched between two planes containing S atoms. In the Mos2 crystal, shown in Fig 1.1 (a), the separation between two adjacent Mo layers is 6Å and that of S is 2.9Å.

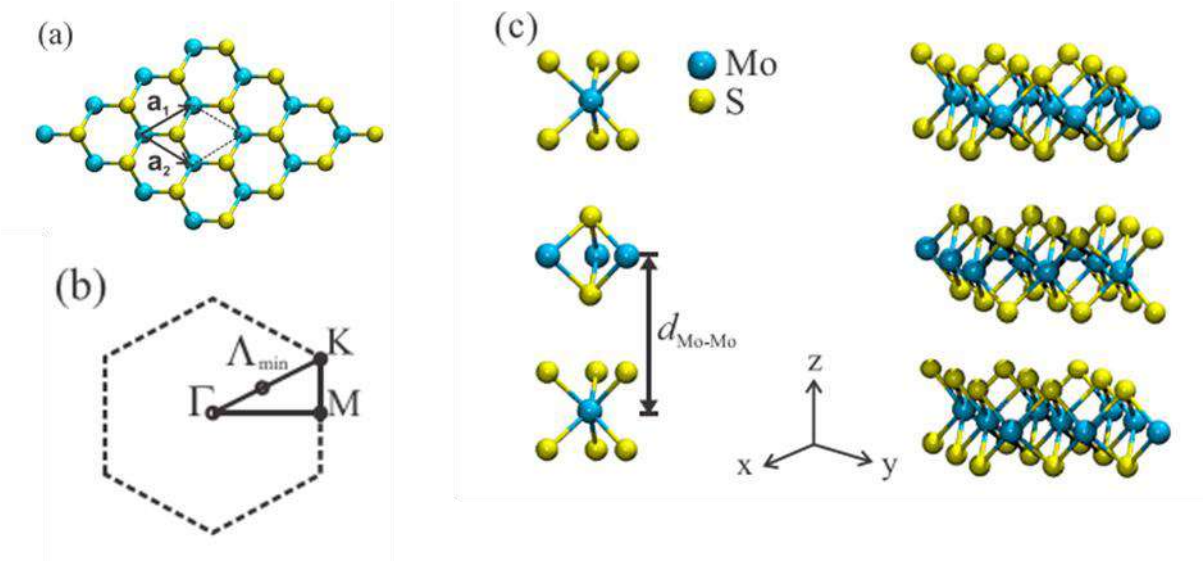

Fig. 1.1 : (a) Top view of a monolayer of MoS_2. (b) The Brillouin zone of MoS_2. (c) The edge view of trilayer MoS_2. Image taken from Padilha et al.

1.2 Electrical Properties of 2D materials

Electrical properties of 2D materials are widely studied. Out of many 2D materials available, Graphene and MoS_2 were the most widely explored materials. In the following sections, we will give more emphasize on the properties MoS_2 based devices.

1.2.1 Band structure of MoS_2

The band structure of MoS_2 is formed primarily by the interaction between Mo-4d orbitals and S-3p orbitals. From atomic calculations, it is seen that the spatial extent of both of these orbitals are almost the same, ≈1.1Å. However, the role of Sulphur orbitals on the band structure is seen to become stronger as the number of MoS_2 layers is increased resulting in the transformation from direct band gap semiconductor (monolayer) to an in-direct band gap material. Mono-layer has a direct bad gap at K point as shown in Fig. 2(d)**.** This is the band gap for the excitons in ground state in MoS_2 and hence it is also called optical band gap. It has been shown that the conduction band states at the K point in a monolayer arise primarily due to the orbitals of Mo atoms. Since this Mo layer is at the middle of two S layers, the Mo orbitals have minimum interaction with other atoms. In other words, the electronic states which are created by the contribution from Mo orbitals have very less dependency in the number of layers. But there are other states at Γ point of the Brillouin Zone as shown in Fig 2 which are from the combination of both Mo and S atoms. As the number of layers changes, this level at the Γ point goes upwards and becomes the Valence band maximum. Hence the MoS_2 multilayers are indirect band gap materials (Splendiani et al. 2010). The evolution of band gap is shown in the Fig 1. 2.

Another important factor in this context is the Spin Orbit Coupling (SOC) at the valence band of the TMD monolayers due to which the valence band is split into two levels. The splitting is prominent close to the valence band maximum resulting in an energy difference of 150 meV at the maxima for monolayer MoS_2. The extent of separation between the energy levels, as a result of SOC, depends on the transition metal atom in the TMD material. However, SOC does not affect the conduction band minimum. In the case of Tungsten containing materials like WS_2, the value of this energy split is 450 meV (Yao et al. 2008). It is also seen that SOC does not lead to any shift in the positions of valence band maximum and conduction band minimum in the band structure. Nonetheless, the absolute values of the band gap reduces because of SOC. Spin orbit coupling and associated valence band energy level split, are the origin for several outstanding optoelectronic properties of TMDs.

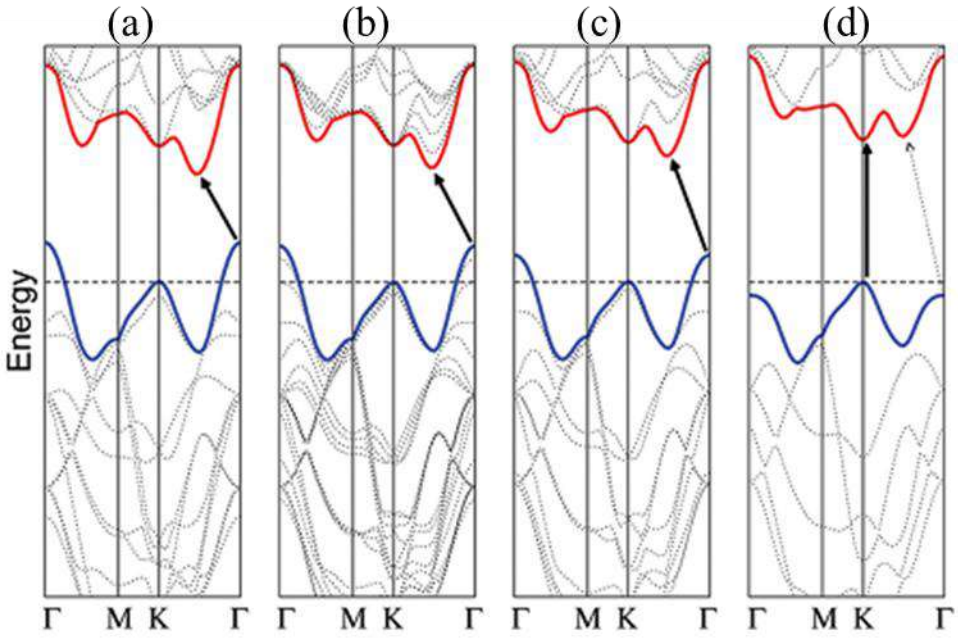

Fig 1.2. Calculated band structures of (a) bulk MoS_2, (b) quadrilayer MoS_2, (c) bilayer MoS_2, and (d) monolayer MoS_2. The solid arrows indicate the lowest energy transitions. Image taken from Splendiani et al.

1.2.2 Electrical properties

Electrical contacts to 2D material has been extensively investigated (Léonard and Talin 2011).This is important because the contact resistance should be low enough to ensure high responsivity in photodetectors made using TMDs. Metal contacts with 2D materials present a number of experimental and conceptual challenges. Conventional model of metal-semiconductor junction is based on the 3D charge transfer. In such junctions sufficient quantity of semiconductor material is present to create bending of energy bands within the semiconductor, thereby creating the potential barrier. However, this picture of band bending is not applicable to the case of metal junction with 2D materials. In 2D materials, the semiconductor is an ultra-thin film and the quantity of semiconducting material is insufficient to cause appreciably band bending as in bulk semiconductor. Similarly, the origin of Schottky barrier is also different in the case of two dimensional material-metal interface (Xu et al. 2016).

Generally the carrier transfer between the metal and the semiconductor depends on the contact resistance. In the case of Si based devices, high concentration doping is applied in the metal contact area. In addition, the metal contacts are annealed at high temperatures to facilitate the diffusion of metal atoms into the bulk of the semiconductor layer. This leads

to a chemical bond between the metal and semiconductor, thus reducing the contact resistance of the metal-semiconductor junction to a very low value. In contrast, for the case of 2D materials, these approaches are inadequate. Conventional high temperature doping methods fail in this case because at high temperatures 2D materials are not structurally stable. Typically, two dimensional materials tend to oxidize when annealed at temperatures above 600C. Moreover, the two dimensional materials have a naturally passivated surface. Consequently, when a metal film is deposited on two dimensional materials, there is no bond formation as is seen in the case of Silicon devices. The absence of dangling bonds is also a reason for the relatively high contact resistance in the case of metal- TMD interface.

Fig 1.3 shows the possible scenarios for metal-bulk semiconductor and metal-two dimensional contacts. In the case of metal film on a bulk semiconductor, diffused contacts are created between metal and semiconductor. Such contacts cause band bending at the semiconductor surface as shown in Fig 1.3(b). In contrast, in the case of two dimensional materials, the metal atoms do not diffuse into the 2D material. Hence, it may be surmised that a thin layer of air separates the metal film and the 2D material. This gap is called Van der Waal gap (VdW gap).Charge carriers have to tunnel through this barrier to enter the 2D material. Further, the nature of band bending is also different as shown in Fig 1.3(d). The potential barrier caused by this air gap is not constant and depends on the extent to which the metal atoms interact with TMD. In the case of metals which interact strongly with TMD, the band bending, and the associated charge transfer, is similar to the case of bulk semiconductor as shown in Fig 1.3(f). An example of such cases is Titanium, a low work function metal, used as the contact metal for MoS_2. In Fig 1.3, E_c is conduction band minimum, E_v stands for valence band maximum, E_f is Fermi level position, TB is the tunnel barrier and SB is the Schottky barrier between metal and semiconductor.

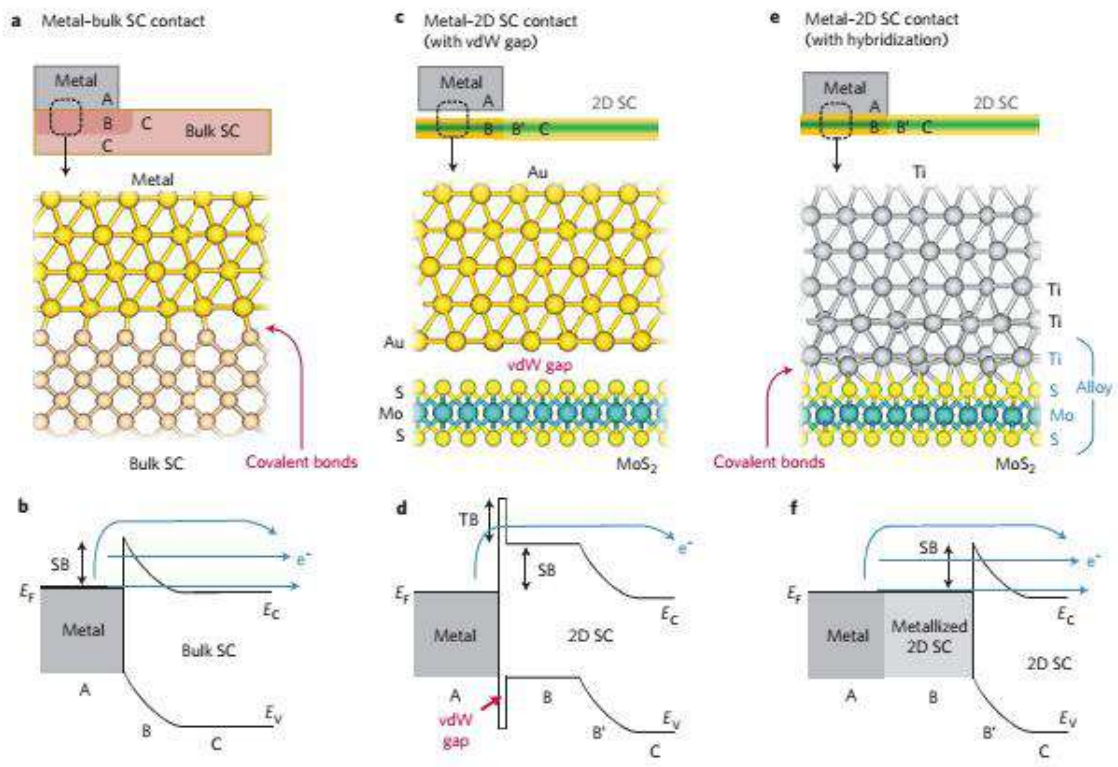

Fig 1.3. Different types of metal–Semiconductor junctions. (a) Schematic of a typical metal/bulk SC interface.(b) band diagram of metal/bulk SC interface; (c) Metal/2D SC interface with air gap; (d)band diagram of Metal/2D SC interface with air gap; (e) Metal/2D SC interface with hybridization; (f) band diagram of Metal/2D SC interface with hybridization. Image taken from Allain et al.

Many methods have been tried to reduce the contact resistance of metal –TMD junctions. It includes (i) doping the entire TMD channel heavily by chemical methods instead of high temperature diffusion process(Yang et al. 2014b), (ii) Use of certain unconventional metals and metal oxides as contact (e.g., use of Mo as contact material to MoS2) to induce the lattice matching with the TMD crystal (Chuang et al. 2014), (iii) Use of Graphene as contact electrode(Lee et al. 2014) and (iv) edge-to-edge contact between metal film and TMD film (Lee et al. 2014). Chemical doping of the TMD channel is one of the most widely used method. In this process, TMD material is soaked in the chemical solution. Many variations of this process have been tried out leading to doping by Chlorine, Sulphur, Gold etc. (Yang et al. 2014b Bhattacharjee et al. 2015 Sarkar et al. 2015). Chloride doping of bulk MoS_2 resulted in a drive current of 0.5mA/μm in FETs(Yang et al. 2014a)

1.3 Optical properties

1.3.1 Optical absorption

Most of the TMDs have direct band gap when they are in the form of a monolayer. Considering the very small thickness of a monolayer, the absorption of light in these materials are substantial; for example monolayer of MoS_2 absorbs10% of the light incident on it (Mak et al. 2010). The optical absorption increases with increase in the number of layers of the TMD material. It may be noted that multi-layer TMD films are indirect band gap semiconducting materials.

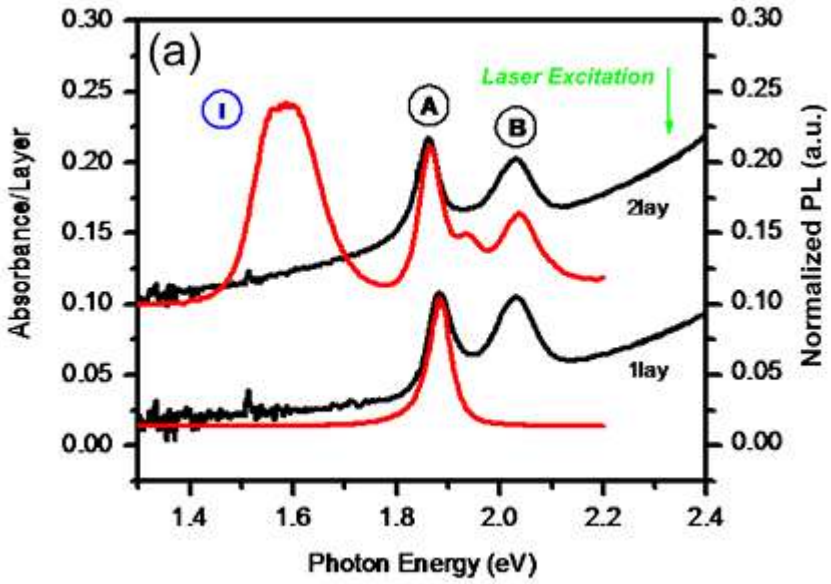

Fig 1.4. Normalized Absorption spectra (left axis) and the corresponding PL spectra (right axis) of MoS_2 monolayer and bilayer. Image taken from Mak et al.

1.3.2 Excitons and trions

In the bulk form, TMDs are indirect band-gap semiconductors. In the case of MoS_2, it has been established, both theoretically and experimentally, that the material remains an indirect band-gap semiconductor until it becomes a monolayer. This is typically evidenced by the emergence of strong photoluminescence in the monolayer. As discussed earlier the valence band maximum of monolayer TMD is split due to Spin Orbit Coupling. In Brillouin Zone, both valence band maximum and conduction band minimum occurs at K point. Hence, upon excitation of TMD using light, electron-hole pairs are generated at K point. These electron-hole pairs will recombine resulting in transition to the ground level by radiative transition in the case of a monolayer. The PL spectrum has the signature of band

splitting in the form of two different peaks in the spectrum. The energy difference between these peaks equals the energy separating the split valence band energy levels. These two peaks in the photoluminescence spectra of monolayer TMDs are called A and B peaks. Due to the ultra-thin nature of the monolayer and very low dielectric constant of TMDs, the photo-excited electron-hole pairs experience strong mutual electrostatic attraction resulting in the formation of excitons. Based on broad similarities in electronic structure within this class of TMDs, as well as the expected decrease in dielectric screening in monolayer samples, strong excitonic effects are expected to dominate in all the monolayer devices. This could lead to unique optoelectronic properties of monolayer TMD devices (Ramasubramaniam 2012).

The band gap estimated from the PL spectra is the optical band gap corresponding to excitons rather than the absolute electronic band gap. It has been theoretically predicted (Ramasubramaniam 2012) that absolute band gap could be much larger than optical band gap. The binding energy of excitons are very high in these materials and is estimated by many groups to be in the range 0.4eV to 0.5 eV. The actual band gap (or the electronic band gap) is the sum of optical band gap and binding energy of the exciton. Consequently, the incident light beam creates a sea of excitons which are rather stable. Fig 1.5 shows a schematic for the formation of excitons. Exciton dynamics in monolayer and few-layer cases deviate significantly from that in a bulk crystal. The binding energy of the excitons reduces when the number of layers increases. In bulk crystals, carrier-carrier scattering and carrier-phonon scattering become the main relaxation mechanisms, whereas, in the case of monolayers the relaxation happens due to intra-band transitions.

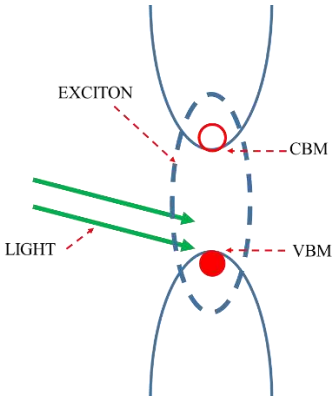

Fig 1.5 schematic diagram of exciton formation in monolayer TMDs. CBM and VBM stands for conduction band minimum and valence band maximum respectively.

Since a high density of excitons is generated during optical illumination, there are good chances for excitons to join with another free charge carrier. While the exciton is a bound state with no net charge, the new particle will have a net positive or negative charge and is called a Trion (Mak et al. 2013). The trion binding energy for monolayer MoS_2 is about 20meV,which indicates the importance of trions for the optical properties of TMDs, even at elevated temperatures (Lui et al. 2014 Mak et al. 2014 Kim et al. 2016). Trions are charged particles and, hence, can be manipulated by external electric or magnetic field (Ross et al. 2013, 2014).In the PL spectra recorded in our experiments the A-peak is an envelope of both exciton peak and trion peak (Mouri et al. 2013 Pei et al. 2015). These two peaks get resolved only at very low temperatures for MoS_2.(Mak et al. 2013 He et al. 2014)

1.3.3 Valleytronics

As we have seen, in monolayer MoS_2, the conduction and valence-band edges are located at the corners (K points) of the 2D hexagonal Brillouin zone, similar to Graphene. The two in-equivalent valleys constitute a binary index for low energy carriers. In Graphene, there can be scattering of electrons from one valley to the other as they are having similar energy. But in the case of MoS_2, these valleys are separated from each other, sufficiently, in momentum space. Because of the large valley separation, the valley index is expected to be robust against scattering phonons. So an electron which is trapped in one of the valleys is expected to stay there for very long time. So we can identify electrons as electrons in K valley or K' valley. Since K and K' points behave separately towards many other physical parameters, this valley number can be used as an information carrier. This opens up great enthusiasm to manipulate valley electrons and this relatively new branch of physics is called "Valleytronics". (Xiao et al. 2012)

MoS_2 monolayers have two important features distinct from Graphene. Inversion symmetry is explicitly broken in MoS_2 samples having odd number of layers, whereas samples with even number of layers possess inversion symmetry. Inversion symmetry breaking, leads to valley dependent quantum selection rules for inter-band transitions at K points. More interestingly, there is a strong spin orbit coupling at the valence band maximum, originating from the "*d*" orbitals of the transition metal atoms. This spin orbit coupling splits valence band maximum at K point, into two levels. The energy separation between these levels depends on the transition metal in the TMDs as shown in Table 1. Experimentally, in the case of Mo, this separation is around 150meV and In the case of W based

materials, the energy split is around 450meV (Table 1 shows the calculated valance band split using HSE method). Thus Brillouin Zone of MoS_2 contains set of three K points with "spin –up" state in the higher energy level and the set of three K' points with "spin-down" state in the higher level.

Table 1: comparison of band gap and valance band split of various TMDs

TMD	Structural Parameter(a and d in Å)	Calculated valence band in meV(HSE method) due to SOC	Band gap (calculated, in eV)	Bandgap(measured in eV)
MoS_2	3.18, 1.56	193	2.05	1.85
$MoSe_2$	3.32, 1.67	261	1.75	1.57
WS_2	3.19, 1.57	521	1.87	2.1
WSe_2	3.32, 1.68	586	1.68	1.65

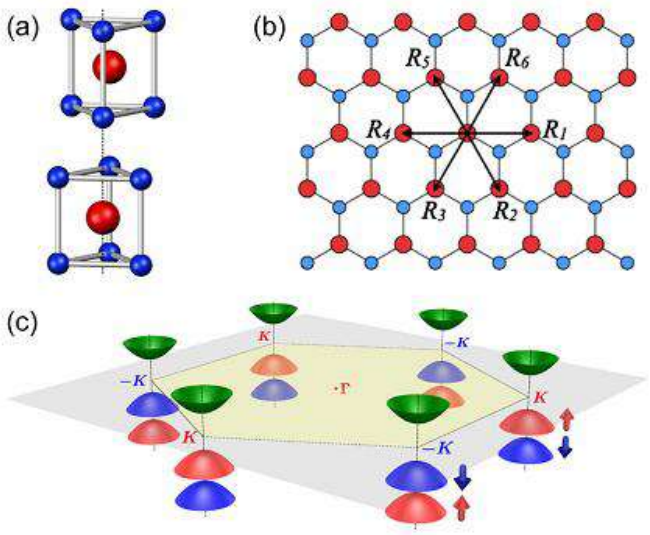

Fig 1.6 symmetry and spin orbit coupling in TMDs; (a) side view which shows breakage of inversion symmetry in monolayer MoS_2 and its restoration in bilayer MoS_2 (b) (b) Top view of theMoS2 monolayer. R_1 to R_4 are the vectors connecting nearest Mo atoms. (c) Schematic drawing of the band structure at the band edges located at the K points, showing "spin-up" and "spin-down" states(-K is similar to K'). Image taken from Xiao et al.

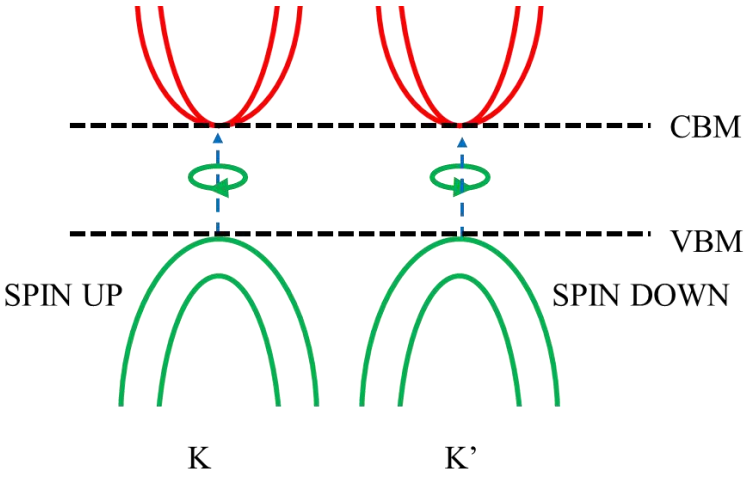

Fig 1.7 Schematic drawing of the optical excitation of K and K' valleys in monolayer TMDs with circularly polarized light. Direction of the green circles indicates the chirality of the circularly polarized light

Thus, the valence band splitting is actually spin-dependent selection rules for the transitions and is tied up with inversion symmetry breaking. One may expect a sign reversal for magneto-optical effects such as Faraday rotation and Kerr rotation by spin-polarized electrons. Selective excitation of carriers with various combinations of valley index becomes possible using optical fields of different circular polarizations and energies. By using circularly polarized light, selective excitation of K or K' valleys is possible. Optical field with Right Circular Polarization (RCP) can generate spin-up electrons in valley K, while the excitation in the K' valley is simply the time-reversal of the above. i.e., a Left Circularly Polarized (LCP) light can populate the other valley. Such a spin and valley-dependent selection rule can be used to generate long lived spin and valley accumulations on sample boundaries in a TMD sample. If an in-plane electric field and light excitation is applied, the electrons originating from the two different valleys will move two directions with opposite velocities, which is similar to Hall Effect.

The reverse of this process is also observed. By the application of electric field, circularly polarized light was produced from TMDs based p-n junction. This is shown in Fig 1.8 (a). The chirality of the emitted light was controlled by the electric field applied(Zhang et al. 2014). Even few layer thick WSe_2 was also used for the light emission. The p-n junction was made on TMDs with electrical double layer transistor architecture. Under a static electric field, the hole distribution shifts parallel to the field in the momentum space, whereas the electron distribution shifts to the opposite direction. As a result, the electron-hole overlap shown in Fig. 1.8(b) differs between the two valleys because the carrier distributions

in TMDs are not isotropic(Kormanyos et al. 2013).This is called Valley Overlap Polarization (VOP). The shift discussed here is much larger than the Fermi surface shift in metals because the carrier density in the intrinsic region is substantially low and the field strength is much stronger. VOP provides an intensity difference in the luminescence from two valleys, leading to circularly polarized luminescence. The above scenario is widely applicable to TMDs that have two isolated anisotropic valleys with different chirality.

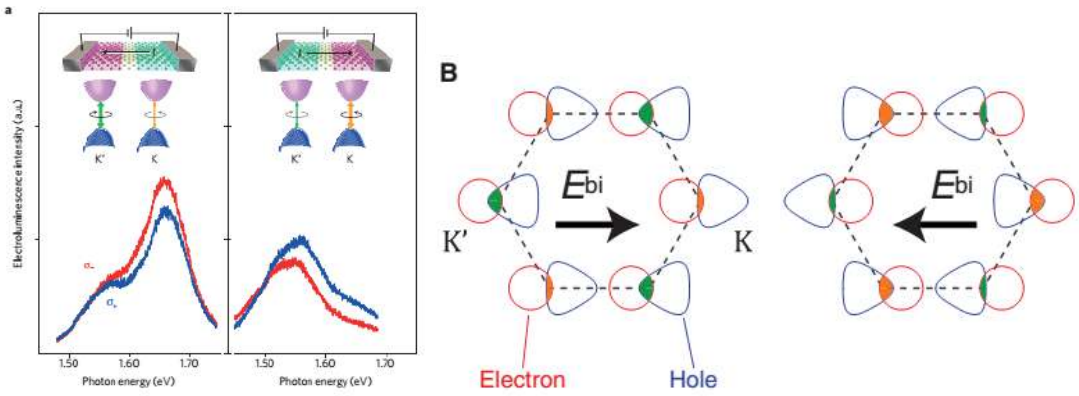

Fig 1.8 Polarized light emission from monolayer TMDs; (a) electroluminescent (EL) spectrum of the light emission from the p-n junction formed by monolayer TMDs. corresponding status of the current flow in the device is shown at the top; (b) schematic representation of valley overlap polarization. Electric field controls the valley overlap polarization to produce the polarized light. Image taken from Zhang et al.

1.4 2D Heterojunctions

1.4.1 Concept of Heterojunctions

For many years, the concept of heterojunction (or heterostructure) has been used in the semiconductor industry. The properties which a single semiconductor cannot perform, can be done by making a heterojunction. In the case of Si and III-V devices, such heterojunctions are created by epitaxial growth like Molecular Beam Epitaxy (MBE). This condition, many times, restrict the epitaxial growth of many interesting combinations of materials as lattice matching with the substrate might not be possible for them. But the recently discovered 2D materials does not suffer from this lattice matching restriction as they have very minimal out of plane interaction. In ideal case, any 2D material can be integrated with any other materials just by placing them on top of each other.

With recent advancement in the 2D material processing, aligned placement of two different kinds of 2D flakes on top of each has made possible. It will function as atomically thin heterojunction. This will assure high quality hetero-interface. A lot of 2D materials are

available with different band gaps and band off sets. Heterostructure of two dissimilar materials, hence, will equip us to tune properties for specific applications. The fact that the density of states in most of these materials can be controlled by gate voltage, also make heterojunctions more important. Though single layer TMDs are, in general, direct band gap materials, it absorbs only 10% of the incident light. Though it is a high absorption in the absolute scale, this absorption cannot be scaled up by increasing the number of layers as the TMDs become indirect band gap material. But fabrication of heterostructures circumvent this problem to a certain extent as heterostructures are having more interaction length for photons and at the same time, it is not an indirect band gap material. Most of the heterojunctions are having a Type- II arrangement of bands. This helps to separate electrons and holes more efficiently. The time delay in injecting charge carriers from one layer to the other is sub-pico seconds. Electrons and holes are thus transferred to different TMDs and they make indirect excitons(Ceballos et al. 2014) electron in the exciton is in one material and associated hole is in the other material. The life time of these indirect excitons is much more than normal excitons (as they are physically more separated).

MoS_2 is generally n-type in nature. It is difficult to make a p-type doping in MoS_2. Similarly WSe_2 is a p- type material. So if we can keep these two materials on top of each other, that will constitute a p-n junction device which is otherwise not possible(Lee et al. 2014).These two materials make a Type –II heterojunction when they are stacked on top of each other. The valence band off set is more than the conduction band off set. This makes the potential barriers for electron and hole transfer different. This results in an asymmetric current-voltage relation as we see in a p-n junction diode. But we need to remember that the microscopic origin of this is junction different from lateral (conventional) p-n junction. In the conventional p-n junction (lateral), the properties of the junction are mainly dependent on the depletion region formed between p and n regions. But in the case of vertical heterojunctions, quantum tunneling of electrons become increasingly important. More importantly, this tunneling can be tuned by the application of an external gate field. The photoresponse of these materials are also gate dependent. Short circuit current density becomes maximum when gate voltage is absent. Short circuit current reduces by the application of gate voltage of any polarity. The spatial photocurrent mapping of these devices also shows that the maximum photocurrent emission happens from the overlapping area between two layers. The photoluminescence data goes in line with this observation. The direct band gap of monolayer MoS_2 is 1.9eV and that of WSe_2 is 1.65eV. Hence at the junction area, there is a strong

quenching of the PL intensity. This also proves the fact that there is a separation of charge carriers in the junction area. Large band offsets between two materials will also be a reason for photon mediated carrier creation. As mentioned earlier, the band off sets for electrons and holes are not the same. So it results in an asymmetric transfer rates for electrons and holes. The excitons which are created in monolayer TMDs are dissociating in a much faster rate in these devices compared to its monolayer counterpart (with single 2D material). This quick dissociation of excitons could also be originating from the sharp potential step happening in atomic layer perfection. The observed band off sets will also increase the rate at which excitons are broken at the junction region (as the electric field across the junction will be tremendous because of the sharp junction).

One modification which researchers could do to this heterojunction is the use of Graphene as an electrode. We know that Graphene is highly transparent and electrically conducting when it is monolayer. Also, the density of states in Graphene can be adjusted with the gate voltage (as the gate voltage changes the Fermi level position and hence the conductivity in Graphene) so as to get the required band alignment (and hence controlled current injection) with the TMDs. In normal heterostructure devices, though charge carriers are created in vertical junction, the collection of these charge carriers are happening at the metal electrodes which are at the lateral side. This will reduce the efficiency of this kind of devices as typical TMDs are low mobility materials. By the time the electrons and holes reach the electrode, there could be fair amount of recombination happening in the channel. So in order to reduce the effect of this recombination, Graphene is used as transparent electrode. So the device architecture is modified as MoS_2/WSe_2 stack sandwiched between two Graphene electrodes. The short circuit current in this case is slightly higher than the previous case. The current-voltage relation is a linear curve when TMDs are monolayers (because of the direct quantum tunneling) and becomes rectifying as the TMDs used are multilayers. Hence changing the number of layers in this architecture gives another handle to tune the device performance. This will be discussed later in the context of photodetectors using heterojunctions.

Heterojunction between Graphene/TMDs has also attracted much interest. MoS_2monolayer is exfoliated on Graphene. The conducting AFM (c-AFM) studies (which measures the total conductivity of the substrate) reveals that the total conductivity of Graphene is reduced when it is sitting on MoS_2. As mentioned earlier, there is very minimal electronic coupling between 2D materials. Hence this reduction in the conductivity cannot be explained by the

electronic structure change of Graphene when it is on MoS_2 as against the Graphene sitting on SiO_2. From the Raman line width broadening, the doping densities of Graphene in the cases of different substrate environments were calculated and it is seen that Graphene on MoS_2 is less doped than that on SiO_2. The way to explain this is MoS_2 delivers more electrons to Graphene when they are on top of each other. Because of this electron transfer, the original p-type doping of Graphene comes down. Hence the Fermi level in Graphene moves much closer to the Dirac point. As we know that the density of states in Graphene decreases as Fermi level moves closer to the Dirac point in Graphene. Hence the whole conductivity reduces. In other words, the electrons transferred from MoS_2hole dopes Graphene. This charge transfer can also result in the barrier formation between the two. This Schottky barrier can separate the electron hole pairs produced by the light. Hence the PL intensity is also quenched at the interface (Shih et al. 2014).

1.5 Photodetectors using 2D materials

Photodetectors are one of the main active devices in optoelectronics. They convert light energy to electrical energy. For photodetectors, there are certain figure of merits. If E_{in} is the incident photon energy, P_{in} is the incident photon power and A is the area of the active area of the photodetector, then External Quantum Efficiency

$$EQE = (I_{ph}/q)*(Pin/E_{in})* A \text{ ---------- } (1)$$

where I_{ph} is the photo-induced current. It is the number of photons required to produce the necessary electron-hole (e-h) pairs which constitute a photocurrent $I_{ph.}$ Another important parameter is the responsivity of the photodetectors. This is the ratio of photocurrent with incident power.

$$\text{Responsivity } R= I_{ph}/P_{in.} \text{ ---------- } (2)$$

Noise Equivalent Power (NEP) is the power at which signal to noise ratio is unity.

Specific detectivity, D*, of photo detection is defined as

$$D^* = (A*BW)^{0.5}/NEP \text{ ---------- } (3)$$

where BW is the Band Width. If there is an internal gain in the photodetectors (such as avalanche photodetectors), gain of the photodetector is defined as

$$G_{ph}= (I_{ph}/q)*(P_{in}/E_{in})* EQE \text{ ---------- } (4)$$

1.5.1 Basic concepts of 2D photodetectors

Basic design of a photoconductor includes a p-n junction diode. When photons hit the depletion region, electron-hole pairs are generated. If a reverse bias is applied across this diode, these charge carriers are pulled to the respective electrodes and thus changing the total current in the circuit. Semiconductors like Silicon, Germanium, and Indium Phosphide etc. are conventionally used for making photodetectors.

2D materials also find its own applications in photodetection. The qualities of TMDs such as ultra-thin body, direct band gap, decent optical activity even in monolayer, flexibility etc. are few of those qualities. Graphene has been investigated as a photodetector by many groups. Now Graphene based photodetectors are almost compatible with commercial silicon based devices. The fact that Graphene is compatible with Silicon technology opens up the possibility of its use in low cost optoelectronic circuits.

1.5.2 Mechanisms of photodetection in 2D materials

The photodetector absorbs the photons and converts photon in to electron hole pairs. In the case of 2D materials where situation is different from a bulk semiconductor based diode, several mechanisms are proposed to explain the photodetection mechanism. It is mainly due to (i) Photovoltaic effect (ii) Photothermoelectric effect (iii) Photo gating effect (iv) Plasmonic effect (v) Hot electron transfer(Koppens et al. 2014).

1.5.2.1Photovoltaic effect

This is the most common mechanism used in photodetection. The electron-hole pairs formed by the photons are moved in opposite directions by the electric field produced due to external bias across the channel or the band bending in the channel by the metal electrode (due to difference in the work functions of two different metal contacts as in asymmetric Metal Semiconductor Metal type photodetector). The reverse bias applied in the case of Graphene has to be controlled carefully so that the dark current is below the allowed level (as the dark current can linearly increase with external bias because of zero band gap of Graphene). In the case of TMDs where there is sufficient band gap, dark current is relatively less compared to Graphene. In Graphene, different mechanisms are tried to realize in plane p-n junction along the channel so that there is a better collection of electron-hole pairs at the electrodes. This includes chemical doping of Graphene channel in to p and n type portions, use metals which by itself Graphene, applying two different gate fields (called as split gates) etc. Many of these processes are not so efficient in the case of TMDs. Each

TMDs has its own behavioral patterns towards each of the above mentioned techniques. E.g., chemical doping of MoS_2 to create p-n junction has not seen much of a progress. Split gate technology works for Tungsten based TMDs, but not so efficient on MoS_2. Graphene has some peculiar property in this regard. The photoelectrons created in the Graphene will undergo a lot of scattering before relaxing to its ground state. Since it is a zero band gap material, each of these scattering can ideally give rise to generation of another free electron in Graphene. In other words, a high energy single electron can give rise to many electrons in the material with varying energy. This is carrier multiplication mechanism which makes Graphene photodetectors a gain more than unity.

1.5.2.2 Photo thermoelectric effect

Photo thermoelectric effect comes from the fact that different materials have different Seebeck coefficients. In the case of TMDs, the measured Seebeck coefficients are higher than the numbers obtained for materials like Graphene. Seebeck coefficient is ≈ 30mV/K in the case of MoS_2 at 280K, which is remarkably larger than comparable materials like Graphene (≈ 100µV/K), carbon nanotubes (≈ 300µV/K), Bi_2Te_3(≈ 200µV/K) and InAs (≈ 5mV/K). this high value of Seebeck coefficients makes in interesting for thermionic applications (Wu et al. 2014). When light falls on the edge between MoS_2 and metal electrode, thermoelectric voltage will be generated. Thermoelectric electrons, or hot electrons, which are created because of the asymmetry in materials will be diffused in all the directions, irrespective of the external bias conditions. So this property is shown to be used for detection of wavelengths even below the wavelength. The photodetection properties are qualitatively same for wavelengths above and below the band gap. (Buscema et al. 2013a)

1.5.2.3 Photo gating effect

Photo gating effect uses the selective trapping of one type of charge carriers from entering the 2D material channel. These charge carriers are used to modulate the conductivity of the 2D material. Electrons or holes, which are not entered in to the 2D material channel can reside in the nearby layers and their presence there will function as a gate field. This can influence the metal-TMD barrier. This effect is generally used in Graphene-TMD hybrid heterostructure devices. This is because influence of gate electric field is predominant in the conductivity of Graphene channel. But these type of devices which involves Graphene, typically suffer from high dark current(Roy et al. 2013).

1.5.2.4 Plasmonic effect

Plasmonic nanoparticles sitting on top of TMDs (typically Au nanoparticles) can make large changes in the way in which TMDs responds to incident light. Firstly, plasmonic nanostructure will facilitate the reflection of light from the edges. This will increase the interaction volume of light in TMDs. Secondly, the surface plasmons generated in the nanoparticle surface will act like a light guiding mechanism and hence to increase the interaction volume between light and TMDs. (Eda and Maier 2013). It is shown that Au nanoparticles of 5-10 nm placed on TMDs enhances the photocurrent by a factor of ten (Britnell et al. 2013). The advantage of plasmonic effect is that it is very easy to fabricate. Typically, annealing of very thin Au film (10nm) coated on TMDs at relatively low temperature will make it to break in to nanoparticle array. By changing the thickness of the gold film and the annealing temperature, the size of the nanoparticles can be varied. This in turn, to a certain extent, will change the peak absorption wavelength of the detector also.

1.5.2.5 Hot electron transfer

When light is shone in the metal-TMDs junction, the metal can absorb the light and gets heated up. This can produce hot electrons in the metal, even though the wavelength is less than the work function of the metal. Thus produced hot electrons can be trapped in to the TMDs since they are in very close proximity. Once trapped in to TMDs, these electrons will behave like normal photoelectrons and collected at the electrodes. There is a subtle difference between hot electron transfer and photo thermoelectric effect in this way. We can easily differentiate between these two as the later will be independent of the external bias.

1.5.3 Photodetectors: different architectures

Based on the above discussions on the variety of process involved in the photodetection mechanisms, different designs are developed. We cannot exactly copy the designs used in the case of Si photodetector due to the lack of reliable doping methods. It is seen generally that general photodetection happens as a result of one or more above mentioned methods.

1.5.3.1 Metal Semiconductor Metal (MSM) photodetectors

This is one of the earliest designs of photodetectors. Two metal electrodes are placed on the semiconductor slab (which is 2D material here). Bias voltage is applied across this electrodes. Light is illuminated, either globally or locally. In the case of global exposure, photovoltaic effect make electron hole pairs in the channel. These free carriers will change

the total resistance of the channel and hence, change in current will be observed. We have to note that, at the same time, the metal electrodes are also getting heated up and this can eventually add up to the current by photo thermoelectric effect and hot electron transfer(also by plasmonic effect in a small scale). In order to differentiate between the roles of different effects, typically, scanning probe microscopy is used where the laser is made in to a spot using objective and shine locally in the semiconducting channel(Lopez-Sanchez et al. 2013).

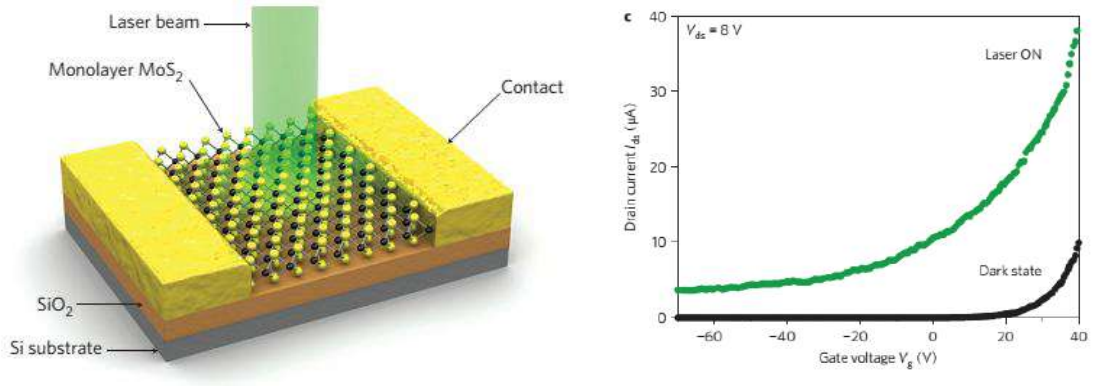

Fig 1.9 Photocurrent generation with monolayer MoS_2; (a) Schematic of the device where monolayer MoS_2 is contacted by two metal electrodes. Green beam represents the green laser illumination; (b) photocurrent and dark from the device. Image taken from Lopez sanchez et al.

There are some specific observations in the case of Graphene. It gets strongly doped by the presence of metal electrode. One high work function metal and low work function metal kept the two ends of Graphene makes a differential doping concentration in the channel as shown in Fig 1.10. So this can create a band bending in the channel without any extra effort. Ideally, this band bending is enough to drift the photo generated electrons and holes in different directions(Xia et al. 2011).

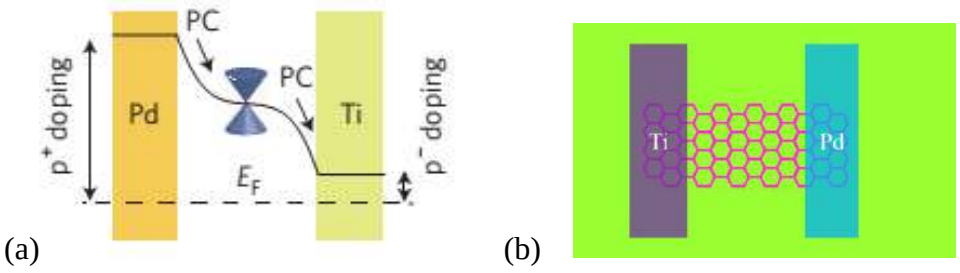

Fig 1.10 asymmetric metal electrode MSM device (a) band profile which shows bult in electric field (b) schematic of the top view of the device. Image taken from Xia et al.

1.5.3.2 Hybrid photodetectors

Hybrid photodetectors use the combination of Graphene with TMDs. Typically they make use of the photo gating property of Graphene. One of the highest responsivity numbers in the field of photodetectors are shown by using this method (Roy et al. 2013b). Graphene channel is used for conduction which is kept on top a thin slab of MoS_2. Bottom gate is used to modulate the charge concentration in MoS_2, which in turn put corresponding charges in the Graphene layer. If a negative voltage is applied at the gate, MoS_2 generates holes in the top layer of it. As Graphene layer is on top of MoS_2, this positive charge can change the density of states in Graphene and hence the conductivity of Graphene is modulated. This photo gating effect can be amplified by the changing the gate bias or the drain bias. Responsivity goes up to $\approx 10^{10}$A/W with the application of 60V gate voltage. Responsivity is a function of illumination power and decreases with increase in power. The issue in this technique is the very slow recovery which will be coming from the trap states in MoS_2 and SiO_2.

1.5.3.3 Heterostructure photodetectors

Heterostructures fabricated using two different kinds of 2D materials offer wide range of applications. Generally it is difficult to change the doping nature of the TMDs from n to p and p to n reliably. In heterostructures, two different materials are taken which are n and p type by nature. This results in an atomically thin p-n junction diode, which is the basic requirement of an optoelectronic device. Enhanced absorption of light is another advantage. With the built-in field developed across this layers, these devices can work as a self-driven photodetector. The responsivity numbers are generally low if the metal electrodes are contacted at the sides of two TMD layers (since these materials are having low mobility). But this can be increased by the application of a Graphene electrode at both sides. Graphene helps to increase the photodetectivity and speed of detection because of its high mobility (hence less charge transport through TMDs), high transparency (better light absorption by the active layer) and carrier multiplication due to it zero band gap (increases the gain).

In the table 2, different types of photodetectors made using two dimensional materials, are compared. This table includes the device architecture and the underlying physical process for light detection. The responsivity numbers for each of this devices with corresponding wavelength of detection is also given in the table.

Table 2. Comparison of the properties of various photo detector configurations

Device	**Type**	**Responsivity(AW^{-1})**	**Wave-length**	**Reference**
Graphene-metal	Photoelectric	$6.1x10^{-3}$	Visible to IR	Xia et al, 2009
Graphene p-n junction	Photoconduc-tive	10^{-2}	Visible	Lemme et al, 2009
Hybrid Graphene quantum dots	Photo gating	10^{8}	0.5 to 2 µm	Konstanta-tos et al, 2012
Graphene MoS_2 hybrid	Photo gating	10^{10}	Visible	Roy et al, 2013
MoS_2	Photovoltaic	10^{3}	Visible	Sacnhez et al, 2013
WSe_2 p-n junction	Photodiode	$16x10^{-3}$	Visible	Pospischil at al, 2014

1.5.4 Typical applications and challenges

High speed applications: Graphene photodetectors are promising in the speed of detection. It is comparable with the commercial Si of III-V detectors. Also since it is semi-metallic in nature, it has wide spectrum for detection. Also, integration of Graphene with Si is not as difficult as integration of III-V. Challenges for Graphene devices are relatively low responsivity and the high leakage current. TMDs based heterostructure devices overcome this issues to a certain extent. Picosecond response is shown with Graphene integrated TMDs photodetector (Massicotte et al. 2015). Even then, reliable fabrication of stacks of 2D materials need to be tuned and integration of this in to a device is still a challenge.

Highly sensitive detection: Another area of interest here is the high sensitive detection of various objectives, such as gas sensing and biomedical imaging. Si based devices are not

really suitable for this applications as it cannot measure above far IR and more. 2D materials photodetector, on the other hand, can be tuned to specific applications by the careful selection of 2D materials. Also, 2D photodetectors can work with low operating voltages. It is shown that bulk layers of MoS_2 can work in harsh environments also (Tsai et al. 2014).

1.6 Challenges in the field of 2D devices

1.6.1 Material Preparation

Growing large area 2D materials is still a big challenge, though large sheets of Graphene have been prepared. TMDs are typically grown to the extent of a few tens of micrometers in size by Chemical Vapor Deposition (CVD). Even in CVD, special care must be taken to assure the quality of the TMD film, including its stoichiometry. Mechanically exfoliated flakes from a crystal produces high quality TMD films. But this process offers TMD flakes of very small surface area. Further, a single layer flakes are generally seen as connected to a multi-layer flake. Thus, fabricating devices with monolayer flakes may require the use of various techniques such as electron beam lithography and other nanofabrication techniques for device fabrication.

1.6.2 Doping Techniques

Most of the TMDs exhibit either P-type or N-type conductivity only, due to their Fermi level pinning. For the fabrication of CMOS type devices, hence, it is required to realize both P and N type doping of the TMDs. Conventional Phosphorous doping has been tried on bulk MoS_2. (Nipane et al. 2016). Doping TMDs with chemical solution has also been tried (Yang et al. 2014b Bhattacharjee et al. 2015). But these techniques suffer from the degradation of doping concentration with time.

1.6.3 Electrical Contacts

Formation of completely ohmic contacts to TMD with very low contact resistance still pose a lot of challenges. There need to be a better understanding of the origin and nature of the contact resistance in the case of metal-TMD interface (Popov et al. 2012).

1.6.4 Choice of Substrates

Substrate plays an important role in the device performance. Similar to traditional polar substrates such as silicon oxide, 2D hexagonal boron nitride (hBN) supports phonon–polaritons, quasi particles that result from the coupling of photons and dipole-carrying optical

phonons. The layered nature of hBN makes it possible to tune the phonon–polariton resonance (Xia et al. 2014). Typically TMD materials are grown on oxide substrates. So if the devices are fabricated on hBN substrate, an extra step of transferring the TMD material from oxide to hBN substrate is needed. It is seen that substrate traps are highly active in the case of oxide substrate and these traps degrade the device performance. But with hBN, effect of traps is seen to be very less. But the device fabrication on hBN substrates is, at least now, limited to small number of devices due to device fabrication complexity.

1.6.5 Heterostructure TMD Materials

Fabrication of heterostructures for device applications is an important requirement. Techniques for growing two different TMD materials, vertically or laterally, using CVD is still in its infancy. Many groups are still resorting to the conventional exfoliation method. One material is exfoliated first. Then, with some mechanical set up, the next layer is aligned vertical to the first layer and exfoliated (Britnell et al. 2013). This is a time consuming process requiring great skill.

Degradation of exfoliated TMD flakes is another key point in device fabrication. Once the flakes are exfoliated for the required device application, they have to be kept in protected environments to prevent adsorption of any adsorbed molecules on the films. This will ensure good device performance(Kufer and Konstantatos 2015 Wang et al. 2015 Gao et al. 2016)

1.7 Scope and objectives of the thesis

1.7.1 Scope of the thesis

As seen from the previous sections, there are several missing links in the understanding of the physical properties of 2D materials and also in the techniques for device fabrication. To a certain extend this is to be expected since the field of 2D materials is still in its infancy. As far as the electrical contacts are concerned, much work is needed to create a barrier free electrode either with conventional methods of doping or with new techniques like edge contacts with Graphene(Das et al. 2013a, 2014 Dankert et al. 2014 Guo et al. 2014 Liu et al. 2015). There might need better characterization techniques unlike what is resorted in the case of Si as the interface in the case of 2D materials is very thin. Using conventional methods which are used to study the interface and charge transfer, it might not be very straightforward to study these materials. Also the concept of Schottky barrier itself might

be of different origin in this case as there is not much of volume of 2D material available for the band bending.

Light matter interaction and photodetection properties of these materials is another area where different schools of thought sustains. There are enough experimental evidence for photodetection with photovoltaic effect, photothermoelectric effect and hot electron transfer. We need to segregate the predominance of each of these properties. It might not be possible to come up with a universal theory for the optoelectronic activities of TMDs. but certainly typical case studies for each regime where each one of the above mentioned properties are active should be explained. (Buscema et al. 2013a Kang et al. 2014 Massicotte et al. 2015 Tielrooij et al. 2015 Zhang et al. 2015).

TMDs behave differently to different polarization of incident laser. This valley specific properties are existent at low temperatures. At room temperature, most of these effects disappear because of phonon scattering disturbs the valley conservation. This limits the use of Valleytronics for device applications. Room temperature valley properties will make a big leap in both photodetection and emission of light by TMDs. (Mak et al. 2012 Jo et al. 2014 Kim et al. 2014 Zhang et al. 2014 Lee et al. 2015 Shimazaki et al. 2015)

There are lot more issues to be solved field. It includes the reliable fabrication of p-n junctions in TMDs, large area high quality growth of TMDs, transfer of large area TMDs from one substrate to another, vertical and in-plane growth of TMDs to make heterostructures, superconductivity in TMDs and so on. But in this thesis much emphasize is given to few basic questions. Largely the interaction of TMDs with light and the dependence on the polarization of light is studied. Also there was an effort to understand the mechanism of charge transfer from metal to TMDs.

1.7.2 Objectives of the thesis

The main objectives of this thesis are mentioned below.

I. Investigation of the optical properties of TMDs thin films by means of Photoluminescence and Raman Spectroscopy employing linearly polarized light for excitation.
II. Study of the differences between normal photoluminescence and hot luminescence
III. Estimation of the charge carrier temperature and the lattice temperature using data from photoluminescence and Raman spectroscopy

IV. Investigation of the efficiency of photo-detection by measuring the photocurrent generation from a photodetector, made using MoS_2 film, by employing the Scanning Photocurrent measurement technique.

V. Investigation of photocurrent generation in photodetector having in-plane heterojunction and measure its rise time for light detection.

VI. Investigation of the charge transfer mechanism at the metal-TMD junction by employing different metals for electrical contact and, thereby, get an insight into contact resistance in such devices.

1.8 Organization of the thesis

The research work carried out is presented in this thesis in six chapters.

Chapter 1: This chapter highlights the motivation for the research carried out. It presents a brief overview of the physical properties of 2D materials and their relevance to device applications. It includes a review of recently published works in this area. Outstanding issues in understanding the behavior of 2D materials and the challenges in device fabrication, using such materials, is also discussed. Lastly, the scope and objective of research carried out is presented.

Chapter II: This chapter discusses the various experimental techniques and apparatus used for preparation of the MoS_2 samples and electrical and optical characterization. The techniques employed for fabricating devices for photodetector applications and electrical characterization are discussed. A brief description of the working principle of each of the equipment used for the characterization of TMD flakes and devices is also included.

Chapter III: This chapter presents an investigation of the role of linearly polarized light for excitation in the photoluminescence and Raman spectroscopy. Study of hot photoluminescence and normal photoluminescence is included in the chapter. The use of hot and normal photoluminescence in the temperature determination of the carriers is also described in this chapter. A more detailed picture of carrier excitation in TMDs with linearly polarized light and subsequent relaxation process is also included.

Chapter IV: This chapter discusses the role various photocurrent generation mechanisms in the TMD photodetectors. This chapter also describes the change in the photo detection behavior of TMDs photo detector with change in the number of layer of the TMDs. The role of in-plane heterostructure in the photocurrent generation pattern, is discussed in detail.

The changes in the photocurrent generation behavior in the case of in-plane heterostructure is explained by using the band off set arising at the heterojunction. The Characteristics of a high speed photo detector fabricated using an in-plane heterostructures are also presented.

Chapter V: This chapter discusses the issues related to the fabrication of good electrical contacts in devices using TMDs. The charge transfer mechanism from different metals to a TMD is studied in detail to understand the creation of potential barrier between the two. Results of the electrical measurements are presented to obtain a better understanding of the contact resistance arising in devices made using TMDs. From the various characterizations and electrical measurements, an alternate model to describe the barrier formation in metal-TMDs interface is put forward.

Chapter VI: This chapter presents the summary of the research work carried out along with important conclusions from the experiments. Scope for further research work in this field is also mentioned.

CHAPTER 2

Experimental methods

Overview:

Chapter 2 presents the methods used for the fabrication of TMDs based devices. Various nanofabrication processes are described in detail. A schematic of the process flow for the device fabrication is also presented. Lastly, various equipment's used for the characterization of these materials and devices are also introduced.

2. Experimental methods

2.1 Device fabrication

For the fabrication of various devices using TMDs, we have used standard nanofabrication techniques. The device fabrication was done entirely in clean room environment. Especially, the lithography processes were done in Class 100 clean room.

2.1.1 Selection of substrate

Thin layers of TMDs are quite transparent to visible light. A TMD monolayer transmits 90% of the incident light. We have generally use optical microscope for the identification of TMDs flakes in the process of device fabrication. The TMD flakes have a small contrast difference with the substrate on which they are placed. It has been shown that SiO_2 of thickness 90nm or 285nm on Si gives the maximum contrast for TMDs. Hence it is widely used as a substrate for device fabrication. The use of this substrate is doubly beneficial since, (i) It provides electrical isolation between different flakes on the same chip and, (ii) It serves as a global back gate dielectric for these devices.

For our experiments, we have used silicon wafer having 285nm SiO_2layer, which is thermally grown on Si substrate. A degenerately doped Si substrate was used so that it could be used as gate electrode, if required.

2.1.2 Micromechanical Exfoliation

Micromechanical exfoliation is also known as scotch tape method. It is a widely used method for the obtaining thin layers of 2D materials following the Nobel Prize winning work of Andre Geim and Novoselov. This method takes advantage of the weak interlayer coupling (Van der Waal's force) in 2D materials and, hence, the layers (including mono layers) can be easily peeled off mechanically. A commonly used scotch tape (or a similar tape such as PDMS tape) is first pasted on the TMD bulk crystal. When the tape is peeled

off it carries with it a few flakes of TMD films. Next this tape is pressed hard on to the Si substrate and then taken off. As a result a couple of TMD flakes from tape get transferred onto the substrate which may now be processed further. This process is termed micromechanical exfoliation.

This process is very simple, it yields high quality TMD films and can be implemented quickly. Nonetheless, this process does not yield identical flakes. The flakes deposited on the substrate may have different thickness and geometrical shape. Some of the flakes may be partly multi-layered. Further, the flakes cannot be placed at a pre-determined point on the substrate. Thus, this method is unsuitable for industrial application. The exfoliation with Scotch tape yields a large number of flakes on the substrate, whereas with PDMS assisted transfer, lesser number of flakes, but larger in size, are deposited. This may be advantageous in further processing to make devices in the laboratory.

2.1.3 Wafer cleaning

To make good quality devices we have to use clean substrates. The substrates are washed with RCA 1 and RCA 2 solutions before exfoliation to ensure that the substrates are free from traces of oil or dust. The roughness of the thermally grown oxide layer on the surface of the substrate is in the sub-nm regime. After the RCA cleaning, the substrate is heated at 150 degrees for 10 min on a hot plate to get rid of traces of moisture on the substrate surface. The substrate is now ready for the exfoliation step. The exfoliation may leave bits of residue from the scotch tape on the substrate. To remove these bits, the substrates are dipped in Acetone for 30 min and then rinsed with Isopropanol. Finally, they are dried and used for further processing.

2.1.4 Electron beam lithography

Electron beam lithography (EBL) is used widely for the patterning the TMD flakes into the required shape. EBL does not require use of any mask and involves the use of a fine beam of high electrons to directly write the patterns of any type on the TMD flake. This is routinely achieved using a computer controlled E-Beam equipment. Thus, EBL has become a versatile tool for fabrication of nano-scale devices.

The EBL system used for our work consists of a standard electron gun, which shoots a thin beam of electrons onto the anode having a fine pinhole. The beam passing through the pinhole then passes through a high voltage region wherein the electrons get accelerated to

very large kinetic energy in this drift region. The electron beam is collimated by magnetic lenses such that the beam radius is a few nanometers and the beam shape is cylindrical. We have used Raith E LiNE EBL equipment, operating at 20kV accelerating voltage, yielding an E-beam of spot size ~2nm for our experiments. Modern EBL systems works at very high patterning speeds. In Raith E LiNE, the pattern generator frequency is 10MHz.

The electron beam incident on the resist polymer causes the polymer chains to either break or get cross linked, depending on the nature of the resist. EBL resists are generally different from resists used in optical lithography. Poly Methyl Methacrylate (PMMA) is a widely used positive EBL resist. It is soluble in either Anizole or Chlorobenzene. Depending on the concentration of the solution and the spin coating speed, different thicknesses of resist coatings can be achieved. After the lithography, PMMA is developed in a solution of Methyl Iso Butyl Ketone (MIBK) diluted in Iso Propanol (IPA) in the ratio 1:3. Later, samples are washed in IPA and dried in Nitrogen.

Multi-layer lithography, generally called as overlay lithography, is needed for the device fabrication. This is done with the help of alignment marks. The sample stage is mounted on a high precision Translation Stage having a sub-nm positional accuracy. The alignment marks are realized using Gold metal lift off process in the first lithography carried out for device making.

Typically, the exposure is done by a vector scan of the e-beam on the wafer. The beam can be deflected in all directions, but as the beam deflection increases, the beam spot on the device surface becomes non-circular which is undesirable. This prevents us from doing the exposure solely by beam bending. Hence, modern EBL systems use a strategy of combining beam bending and translation of the device. Large area exposures are typically realized by this method without compromising the resolution, but care must be taken to minimize stitching error generated during the process of linear translation.

2.1.5 Reactive Ion etching

Etching is used for removal of materials from unwanted places. Etching is of two types, namely, Wet etching and Dry etching. Wet etching is done by dipping the sample in chemicals solution. Wet etching is very simple and inexpensive process, but suffers from issues like selectivity, undesirable lateral etch, etc. In dry etching (also called Reactive Ion Etch-

ing, RIE), plasma of select gases is generated in an evacuated chamber by electrical discharge. The chemical nature of the plasma results in removal of the film material on the substrate by chemical reaction. The etch rate can be varied by changing either the discharge voltage or the gas flow rate. If much denser plasma is needed one may employ inductively coupled RF discharge techniques for plasma generation.

MoS_2 film is etched using plasma of a mixture of BCl_3, Ar and O_2.gases. Flow rates for each of these gases are 15, 60 and 10 sccm, respectively. A 200nm thick PMMA film, patterned by EBL, is used as the etch mask. The etching process was done Etch time varies with number of layers of MoS_2 required to be etched. On an average, a relatively thick MoS_2flake (5-10nm) gets etched in about a minute. The whole process was done at very low RF and ICP(150 W) power so as to prevent the erosion of PMMA mask itself. Processing temperature was kept very low (-10^0C) to reduce the chance of PMMA getting cross-linked during etching.

2.1.6 Thin film coating

Physical Vapor Deposition (PVD) was employed for the deposition of thin films for metal contacts. For PVD, we have used DC sputtering and electron beam evaporation. For sputtering of metals, high energy argon plasma was created in the vacuum chamber. The plasma was directed towards the metal target using magnetic field. The metal atoms/ions get deposited on the substrate kept at a distance of 7.5cm from the target. Since sputtering is a plasma assisted deposition, there are chances of the thin monolayers of 2D materials also getting altered due to the exposure to the plasma. To avoid this degradation of the TMD film, electron beam evaporation is used for realizing metal contacts on TMDs. In electron beam evaporation, the source material, taken in a crucible (which is typically Tungsten or Graphite), gets heated to very high temperatures and gets vaporized. The metal vapors condense on the TMD film on the substrate forming the metal contact. The whole process takes place at very low pressure ($\approx 10^{-7}$ Torr). The substrate is provided with a planetary rotation in order to ensure uniform film deposition. Precaution is taken to increase the temperature of the source slowly so that there is a uniform melting of the evaporating material.

2.1.7 Wire bonding

Wire bonding plays an important role in the device fabrication. After the device fabrication, contacts pads are formed on the substrate and thin aluminum wires are bonded onto these

pads for linking the measurement instruments with the device. We have used wedge bonding in our experiments. The substrate is mounted on a PCB and the aluminum wire is lowered gently to make it touch the contact pad. This is now exposed to ultrasonic waves, from the bonding tool, which melts the aluminum wire and hence forms a very good electrical contact. The same procedure is employed at all points where wire contacts are required. As a precaution, we first connected the aluminum wires to the cable connecting to the instruments by soldering and then wire-bonded the aluminum wire to the contact pads. This prevented damage to the devices due to electrostatic discharge during the bonding process. Further, we used proper gloves while handling the wafer thereby increasing the yield of devices substantially.

2.2 Device fabrication process flow

Oxidizing the top layer of silicon wafer:

SIDE VIEW **TOP VIEW**

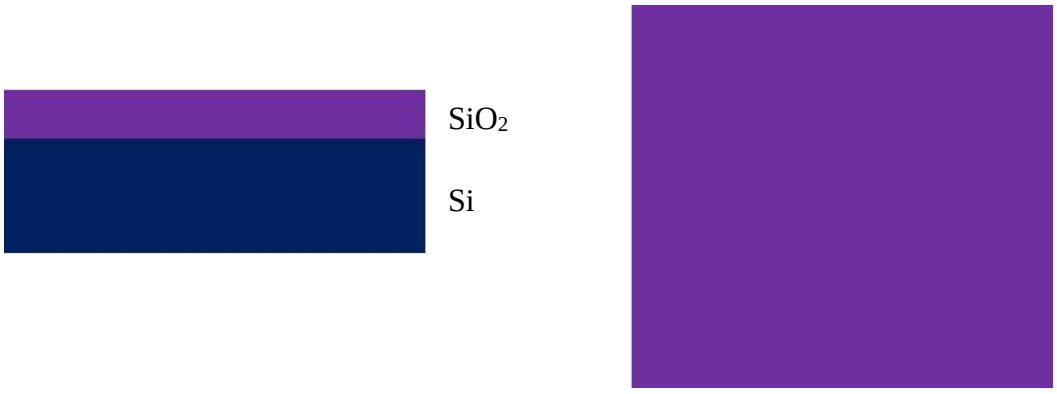

Depositing MoS_2 flake onto the substrate:

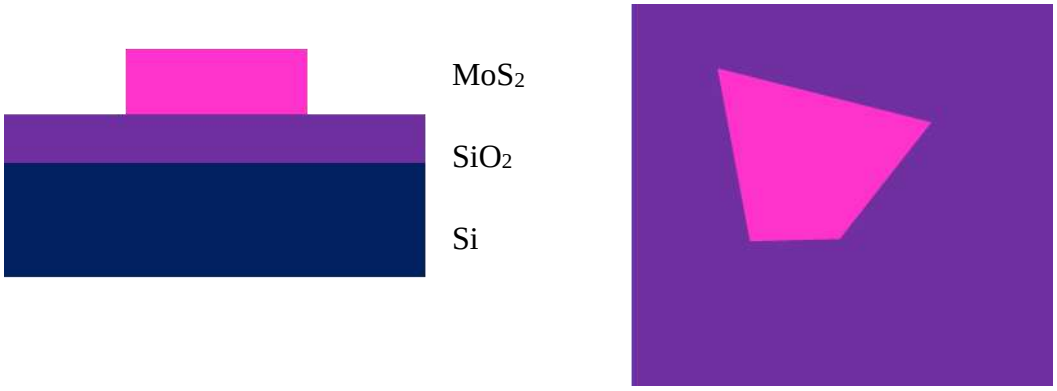

After PMMA resist coating (for EBL)

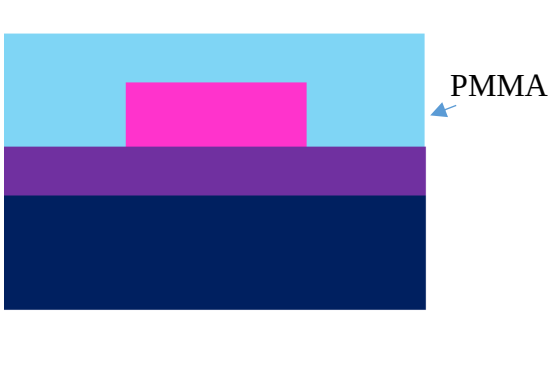

After EBL and development

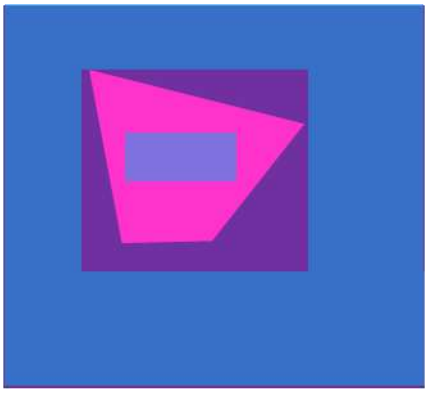

After RIE

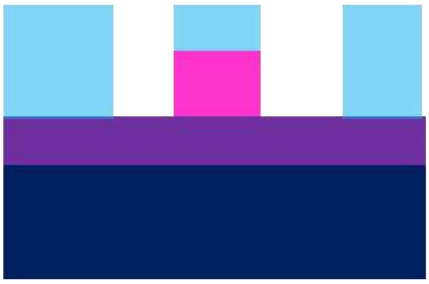

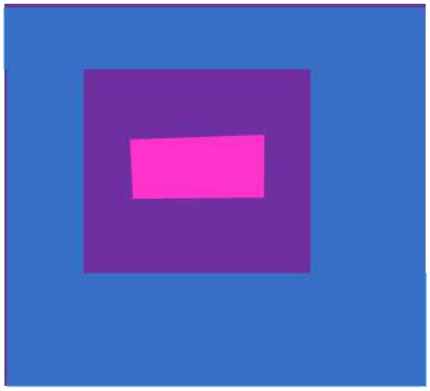

After resist removal in Acetone

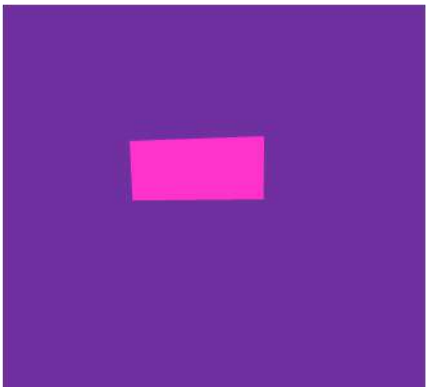

PMMA coating for EBL

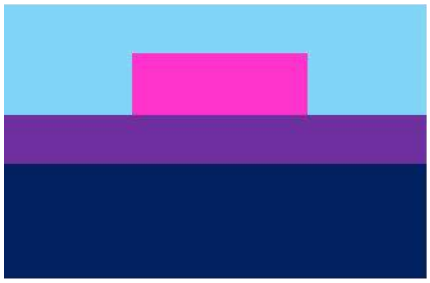

After EBL and PMMA development

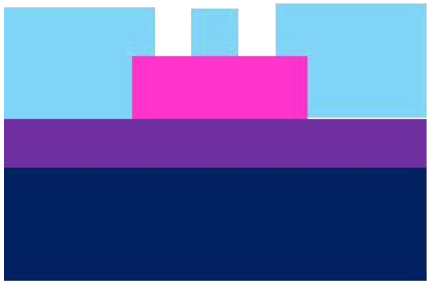

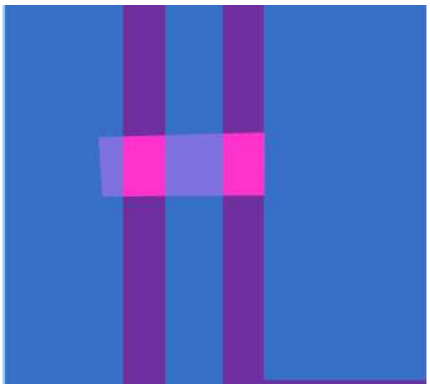

After metallization (ebeam evaporation)

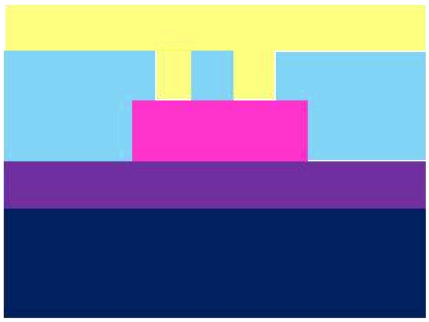

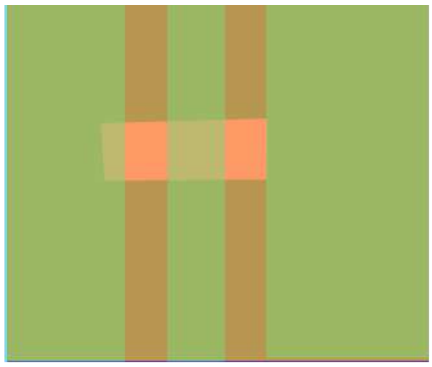

After metal lift off in Acetone

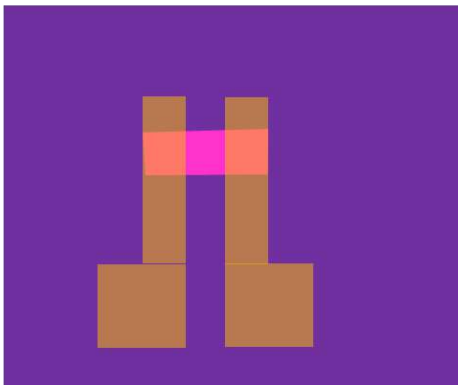

2.2.1 Images of the Device after fabrication

In Fig 2.1, typical devices fabricated by using above process flow is given. Note that the reactive ion etch step is introduced in between to shape the TMD flakes to the proper device dimensions required for the measurement. Also, this step excludes the complexity of the analysis of the device performance by lifting off the variations in the device properties with different number of layers. Many times, the thin layer are attached to multilayer flakes. So it is needed to isolate them from each other by using a plasma etch step.

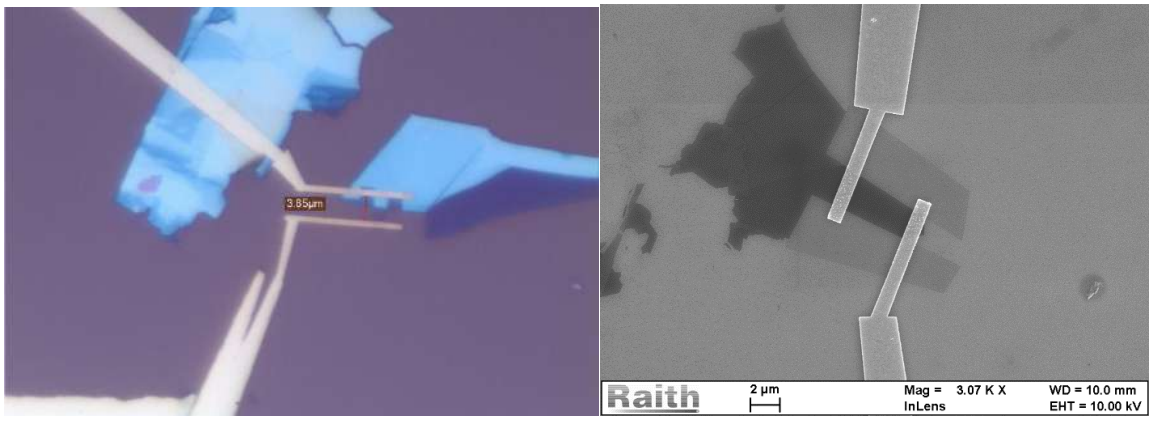

Fig 2.1 Typical devices fabricated using above procedure; (a) optical microscope images (b) Scanning electron microscope image

2.3 Material and electrical characterization

TMDs were characterized in terms of both optical as well as mechanical properties. Optical methods were used for spectroscopic analysis of the material and also for determining the number of layers in the sample. If exfoliated onto a proper substrate, the number of layers of the 2D materials can be easily identified using an optical microscope by noting the color of the flake. To confirm this, we generally use the following characterization methods.

2.3.1 Raman spectroscopy

Raman spectroscopy is a non-destructive optical characterization technique wherein the light scattered from a material sample has a small wavelength shift relative to that of the exciting light due to Raman Effect. The variation in the wavelength is the result of the inelastic scattering of the incident light from molecules that are vibrationally excited. Hence, the Raman shift yields information about the vibrational energy levels in the molecule. Besides the Raman scattered light, we also have the reflected light which comprises of three component, viz., one at the same wavelength as the excitation light (Rayleigh scattering), a weak component at a slightly longer wavelength (Stokes line) and another weak component at a slightly shorter wavelength (Anti-Stokes line). We used 532nm continuous laser beam excitation for the measurements. The laser beam is passed through a band pass filter and is made incident on the substrate using a mirror. A 100X objective is used to focus the laser onto the sample. Scattered light is passed through an edge filter and sensed by a CCD detector, having a resolution of 0.5 cm^{-1}. The entire system was kept on a vibration isolated table.

2.3.2 Atomic Force microscopy

An AFM uses a cantilever with sharp tip for scanning the surface of the sample. This tip undergoes deflection while moving on the surface of the sample, which is illuminated by a laser light. Reflected light from the cantilever is collected by a position sensitive photodetector. The differences between the signals from the different segments of photo-detector may be analyzed to evaluate the position on the sample were the measurement is being made. Thus the topography of the entire sample surface is obtained. By using a feedback loop to control the height of the tip above the surface—thus maintaining constant laser position—the AFM can generate an accurate topographic map of the surface features.

Thickness of the TMD films were measured by AFM (Bruker) under ambient conditions. TMD flakes were deposited on the substrate and kept on the sample stage. Samples were held at a fixed place by vacuum suction and good vibration isolation was ensured. A red laser beam was used to measure the deflection of the cantilever of AFM. Fig 2.2 shows typical AFM scan of the TMD flakes.

Fig 2.2 Typical AFM scan images of TMD flakes

2.3.3 Kelvin Probe Force Microscopy

Kelvin probe force microscopy (KPFM), also known as surface potential microscopy, is a noncontact microscopic technique similar to atomic force microscopy (AFM). Using KPFM, the work function of surfaces and contact potential difference (CPD) between two surfaces in contact can be measured. Typically, different materials have different Fermi levels. So when the AFM tip is brought close to the surface, it experiences an electric force due to the difference in Fermi levels. Equilibrium requires Fermi levels of two surfaces to be aligned at steady state, if the AFM tip and the sample surface are close enough for electrons to tunnel through. Because of the relative re-alignment of the Fermi levels, a contact

potential difference V_{CPD} gets generated. An electrical force acts on the contact area, due to the V_{CPD}. This electric force can be nullified by applying an external bias in the opposite polarity. The applied external bias voltage that nullifies the electrical force due to the V_{CPD} is then equal to the work function difference between the AFM probe tip and sample. Thus, the work function of the sample material can be calculated knowing that of the AFM probe tip (Melitz et al. 2011).

In the AFM used by us the tip was made of Platinum/ Iridium which has a work function of 5.3eV. TMD flakes were deposited on metal stripes by mechanical exfoliation. TMD flakes were located using optical microscope. Further, these metal stripes were grounded prior to the KPFM measurements.

2.3.4 Photo Luminescence

Photoluminescence (PL) is light emission from any form of matter when it is irradiated by light. It is one of many forms of luminescence and is initiated by the excitation using light beams. In a typical PL experiment, a semiconductor is excited with a light-source of energy more than the band gap of the semiconductor. Once the photons are absorbed by the semiconductor, electron-hole pairs are formed with finite momenta in the conduction and valence bands, respectively. These electrons and holes then undergo energy and momentum relaxation from the higher energy states towards the lower energy levels. Once the electrons and holes reach the band edges they can re-combine to generate photons of energy equal to the band gap of the semiconductor. The emitted light has a wavelength longer than that of the light used for excitation. PL has become a widely used technique for the measurement of the optical band gap of semiconductors.

In this work, PL measurements were done using both 532 and 785nm continuous laser light sources. The laser beam was focused on the sample using a 100X microscope objective. The light emitted by the sample was detected using a liquid Nitrogen cooled CCD detector, capable of measuring the energy of the emitted photons from 1.25eV and above. All the measurements are done at ambient conditions.

2.3.5. Electrical characterization

Electrical measurements were done by using Lake Shore low temperature probe station, which is capable of varying the temperature from 5K to 400K. During measurement, the system was pumped down to 2e-6mBar. Agilent B1500 was used as the source meter for

applying electrical bias. For the bottom gated field effect transistor characterization, source and drain electrodes are probed with micromanipulator probes. Chuck was biased for the application of gate, which is a global gate. In this aspect, the bottom side of the substrate was coated with Aluminium so as to make sure the proper bottom contact with the chuck of the probe station. Electrical measurements were done with and without annealing of these devices. Vacuum annealing was done for the devices at 400K for 1Hr, while the chamber was pumped down to 2e-6mBar.

Contact resistance and Schottky barrier height measurements were done by using Transfer Length Measurements (TLM) technique. For this, set of back gated devices were fabricated by using above mentioned process. Monolayer TMD flakes were selected for the device fabrication. On the same monolayer TMD flake itself, set of electrodes were realized with varying distances between them. Effectively, this will act as bottom gated FET devices with varying channel length.

From the electrical measurements, total resistance of each of the above FET devices was obtained. This total resistance includes both contact resistance and the channel resistance. The variation in the total resistance with respect to the channel length (distance between the electrodes) was plotted. By extrapolating this curve to it Y-intercept, the contribution of the channel resistance to the total resistance was eliminated (as Y-intercept has zero channel length). The total resistance at zero channel length corresponds to twice the contact resistance (from source and drain metal electrodes) and hence contact resistance of the electrode will be half of that. For Schottky barrier height measurements, I_d-V_g measurements were done for the above devices at varying temperature. We have changed the temperature from 215K to 290K in steps of 15K. By fitting these current values in the Richardson equation, we could measure the effective Schottky barrier height as a function of Drain and Gate bias at each temperatures.

2.4 Conclusions

In summary, this chapter includes the methods used for the fabrication of TMDs based devices. Various nanofabrication processes are described in detail. A schematic of the process flow for the device fabrication is also presented. Lastly, various equipment's used for the characterization of these materials and devices are also introduced.

.

CHAPTER 3

Valley-Coherent Hot Carriers and Thermal Relaxation in Monolayer Transition Metal Dichalcogenides

Overview:-

In this chapter, we discuss the polarization resolved Raman and photoluminescence. The photoluminescence near the excitation wavelength is studied with varying incoming polarization of laser. The different schemes in which the excited electrons transfer its energy to lattice is also discussed. From photoluminescence spectra and line width broadening in Raman spectroscopy, the temperatures of charge carriers and lattice are calculated. Difference in the photoluminescence spectra with resonant and off-resonant conditions of excitation is also studied.

3. Valley-Coherent Hot Carriers and Thermal Relaxation in Monolayer Transition Metal Dichalcogenides

The electronic and optical properties of these materials have been subject of interest for many researchers (Lee, et al. 2014). In the case of MoS_2 and few other TMDC, the band gap becomes indirect to direct when we move from bulk to a single layer (Splendiani, et al. 2010). This is accompanied by a corresponding increase in the band gap also. Hence, the luminescence decreases as the number of layers is increased. For MoS_2, bulk layer is an indirect band gap of 1.3eV but single layer is direct band gap of 1.9eV. There is a huge increase in the photoluminescence (PL) intensity for single layer when compared to bulk. The PL intensity has been shown to depend on other variables also. e.g., Single layers sitting on Boron Nitride shows better PL than SiO_2 and suspended single layers show even better PL intensity (an increased quantum yield. TMDC are shown to have high photoresponsivity also. It has been shown to have photoresponsivity of 880A/W under laser excitation which is almost 5 orders of magnitude higher than that of Graphene (Lopez-Sanchez, Lembke, et al. 2013).

The direct band gap transition in monolayer TMDs happens at the K (K') points in the Brillouin Zone (BZ). Each BZ is thus having a set of 3 K-points and 3 K'-points. These are called valleys in the BZ. The origin of PL spectra in TMDs is from these K (K') points. When we look at the PL spectra of TMDs, we can get a lot of information about the band structure of these materials and the kind of electronic transitions happening in these materials. For monolayer MoS_2, the main exciton peak (A peak) happens around 1.9eV and the B peak at 2.05eV. The valance band of monolayer MoS_2 is split because of spin orbit coupling and conduction band is doubly degenerate as seen in the previous chapters. The valance band is now split as "spin up" or "spin down" state in the top position. In K valley,

"spin up" state is at the valance band maximum and in K' valley, "spin down" state is at the valance band maximum. This is the reason for the creation of two different photoluminescence peaks of 0.15eV difference in energy. These are called A and B peaks respectively.(Xiao et al. 2012) This PL peaks in fact correspond to the optical band gap of the system. Which in turn, is the exciton ground state in these materials. The small dielectric constant and strong out of plane confinement makes the exciton to stay longer in these materials. In other words, the binding energy of exciton is very high in these materials (Aivazian, et al. 2015). These valleys are shown to have selective excitation under photons of particular polarity (Baugher, et al. 2014). e.g., Right circularly polarized (RCP) laser excites K valley and Left circularly polarized (LCP) light excites K' Valleys. Conduction band minimum does not have any spin split of this kind. So in effect, by controlling the chirality of the laser, we can have a selective excitation of particular type of electrons in this material. This valley specific optical excitation opens up wide variety of possibilities in TMDC (Mak, et al. 2014) (Mak, et al. 2010).

Raman spectroscopy has been used as a very useful tool in the area of 2D materials. It can even be used to determine the number of layers in the film (Chakraborty, et al. 2013) (Corro, et al. 2014). For monolayer TMDs, there are two main vibrational modes. They are called A_{1g} and E^1_{2g} peaks. A_{1g} peak arises from the out of plane vibrations and E^1_{2g} peak arises from the in-plane vibrations. For bulk MoS_2, E^1_{2g} and A_{1g} peaks are at 382 and 406cm^{-1} respectively. As the number of layers reduce, the difference between these peaks also reduces. For single layer, the difference is close to 19cm^{-1} (Molina-Sanchez 2011). If the flake is a bilayer, this difference is between 20-21cm^{-1}. Similarly it keeps increasing as the number of layers increase. Number of layers up to 5-6 can be detected by using Raman spectroscopy.

Fig 3.1 (a-b) explains this situation in much detail. Fig 3.1 (a) describes the various vibrational modes available for the metal and chalcogen atom in the TMD monolayer. Out of various modes, E^1_{2g} (in-plane vibration) and A_{1g} (out of plane vibration) are considered to be more active in these materials. Also, as seen earlier, they are used in the layer number determination in these materials. Fig 3.1(b) shows how the difference between these two peaks vary with the increase in the number of layers in the TMDs.

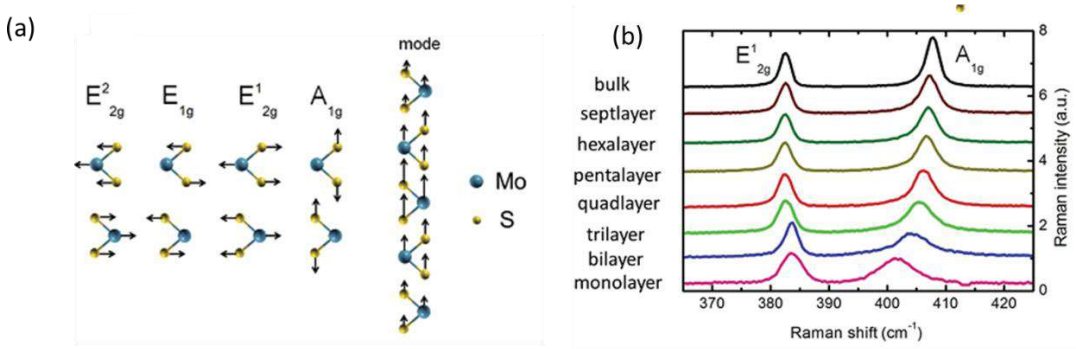

Figure 3.1: Raman spectra of MoS2 with varying layer thickness (a) main modes of vibration in monolayer TMDs (b) changes in the Raman spectrum with change in the number of layers

Here we studied the room temperature valley coherence of 532nm linearly polarized light on MoS_2, $MoSe_2$, WS_2 and WSe_2. The polarization of the incident light was changed using half wave plate. The PL spectra was taken for a larger range, starting right from the excitation wavelength. PL shows a coherence in the emission which can be explained by the valley coherence. This is expected only near the excitation wavelength. Far away from the excitation, this valley coherence is disappeared due to the scattering in the system (Kozawa, et al. 2014).

3.1 Experimental set up

We have studied the photoluminescence spectra of 4 different types of TMDC with two different excitation conditions. They are MoS_2, $MoSe_2$, WS_2 and WSe_2. Monolayers are separated from the crystal using micro-mechanical exfoliation. Silicon substrate with 285nm SiO2 on it is used as the substrate for exfoliation. All the measurements are taken at room temperature. We have selected two laser wavelengths for the photoluminescence measurements; 532nm and 785nm. This is selected so that one is a resonant excitation and other one is non-resonant for the various TMDs monolayer we have studied.

In Fig 3.1 and 3.2, characterization of monolayer flakes of various TMDs with Raman spectroscopy and Atomic Force Microscopy are shown.

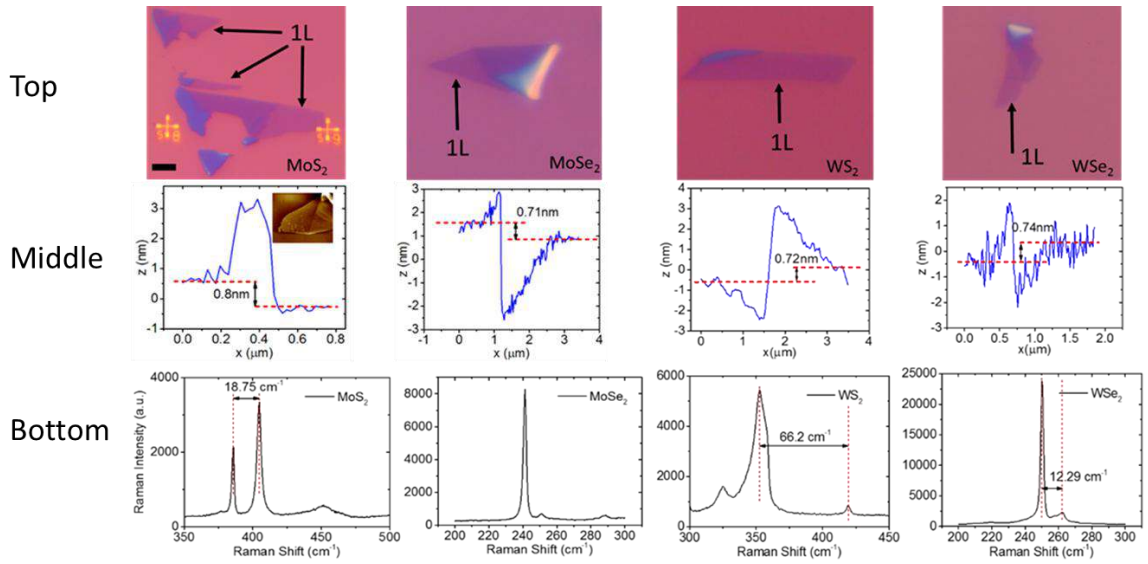

Fig 3.1 Material characterization of monolayer TMDs. Results of MoS_2, $MoSe_2$, WS_2, WSe_2 are shown from left to right; (top) Optical microscope images of the TMD flakes on 285nm SiO_2 substrate. Out of many thickness layers available after exfoliation, monolayer are exclusively marked. ; (middle) AFM scan images of the monolayer of each material (bottom) Raman spectrum of monolayer of each material

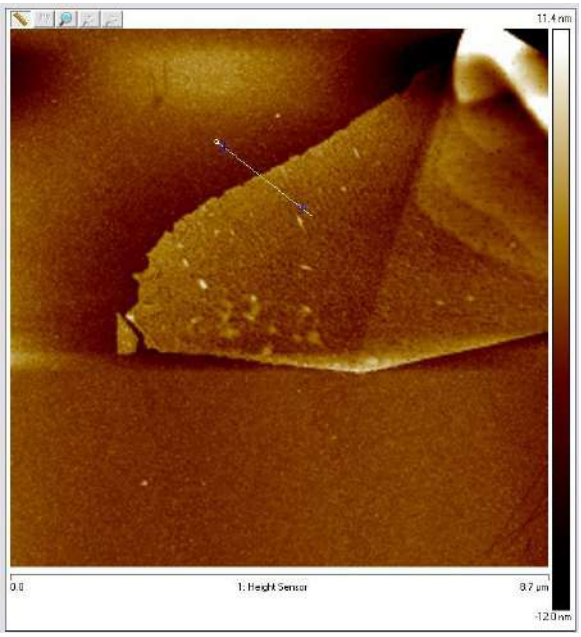

Fig 3.2 Typical AFM scan image of a monolayer MoS_2 layer.

Initially, we have checked the Raman scattering of MoS_2 flakes using a 532nm laser source. Energy of the laser is 2.6μW. Schematic diagram of the experimental set up is shown in Fig 3.3(a). Laser is originally linear polarized in vertical direction. To change the linear polarization of the laser, we used a half wave plate in the optical path, before the laser falls on the substrate. The half wave plate has the provision to change its angle of polarization. If the half wave plate is rotated through an angle "θ", the polarization of the laser beam

changes by "2θ". We have changed the angle of the half wave plate from 0 to 45 in certain steps so that we get a polarization change of vertical polarization to horizontal polarization.

We have kept another analyzer at the detector side, which allows only the vertical component of the reflected light. When the incoming polarization after the half wave plate is vertical, such a configuration we call as "VV" (or co-polarization). In the other case, if the half wave plate sends a horizontally polarized light, such an arrangement is called "HV" (or cross-polarization).

3.2 Results and discussion

3.2.1 Hot and normal Photoluminescence

Initially, we have checked the dependence of Raman spectrum on the polarization angle of laser beam. When we change from VV to HV configuration in steps, we see that the A_{1g} has a change in the Raman intensity. E^2_{1g} does not have any change in the intensity as shown in Fig 3.3 (c). The strong polarization dependence of A_{1g} peak can be seen as a result of symmetry considerations of the corresponding vibrations. From the Raman tensors, intensity of A_{1g} is proportional to $\cos^2\theta$ where θ is the angle of polarization where as that of E^2_{1g} is a constant. From the physical point of view, E^2_{1g} is happening because of the vibrations in the lattice which are in plane. So this vibrations will not really see the change in polarization of the incoming light. But the A_{1g} peak is from the vibrations which are out of plane from the lattice. So when the angle of polarization of the incident light changes, it can strongly change the manner in which it reacts with these out of plane vibrations and hence the intensity changes.

Fig. 3.3 (b) shows the linear polarization resolved photoluminescence intensity from monolayer MoS_2 sample with vertically polarized excitation. The A peak at ~1.85 eV and B peak at ~2.0 eV do not show any polarization resolved characteristics. As this peaks are far away from the excitation wavelength, there could be multiple scattering events which lift the coherence. It includes intrinsic decoherence of trions, and intra- and inter-valley scattering induced decoherence of excitons. Since the excitation wavelength is much more than the optical band gap, it is expected that the electrons will jump to an energy level which is very high in the conduction band. As this state is highly unstable because of its high energy, these electrons will come down to the conduction band minimum by losing its energy in series of collisions (and similarly holes in the valance band also will go up by the same

process). It is very natural to expect that these electrons and holes, which makes the excitons and trions (and the reason for A and B peaks in the PL) does not preserve any polarization history.

On the other hand, when we check the PL spectra close to the excitation energy, we see that there is a strong dependence of PL on the polarization of exciting laser. Although this is region has very sharp and intense Raman peaks along with the PL(which is typically a broad peak), we can make out the polarization dependence of PL by drawing the base line envelope of the PL spectra. Few Raman peaks also show polarization dependent behavior as described earlier. Polarization is changed in the similar way we did for Raman studies. At the detector side, we keep an analyzer which will allow only vertically polarized light.

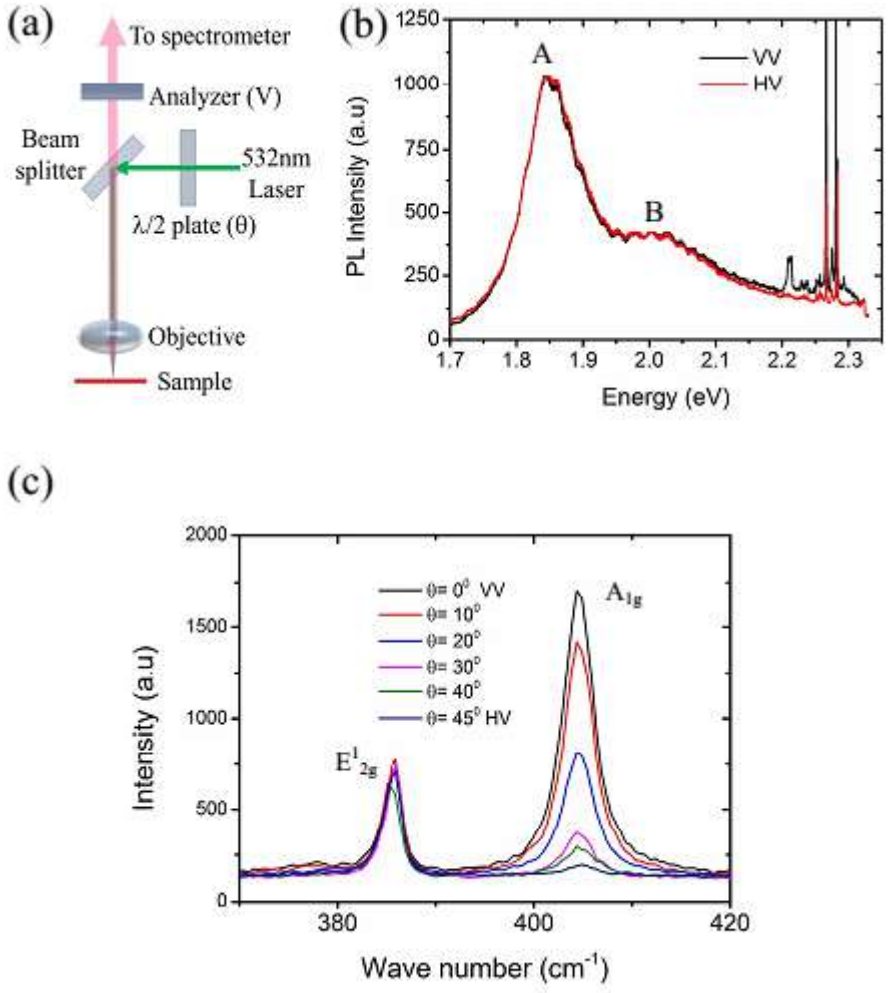

Fig 3.3 polarization dependent Raman and PL studies on monolayer TMDs (a) Schematic of the experimental set up used (b) Linear Polarization resolved PL spectra (c) Polarization dependent Raman spectra

Fig. 3.4 (a), shows a magnified plot of the MoS_2 polarization resolved PL signal which is taken close to the excitation wavelength (2.33eV). Since this area is also having set of Raman peaks, a PL envelope is also drawn by dashed lines as guide to eyes. It is found that the co-polarized (VV) PL envelop and also the corresponding degree of polarization in this configuration is found to have a peak value around ~2.29 eV. The incident vertically polarized photon is a coherent superposition of left (LCP) and right (RCP) circularly polarized light. So when a linearly polarized light falls on TMDs, due to the reasons which we have seen earlier, there will be a creation of electron-hole (e-h) pairs in the K and K′ valleys. These e-h pairs can recombine either before or after exciton formation. (Koch, et al. 2006). This will generate LCP and RCP luminescence at the respective valleys. If these LCP and RCP are emitted coherently, it can create linearly polarized light. The observation of strong linear polarization resolved characteristics imply excellent coherence between the K and K′ hot luminescence (Mak, et al. 2010) (Perea-López, et al. 2013) (Zhang, et al. 2010). This coherence can be happening near the excitation energy because there is a less chance for the scattering to happen at this point. The carriers are excited to an energy level much above the optical band gap and some of them are recombined right at that high energy. The degree of linear polarization drops significantly below 2.2eV, which is ~130meV (more than twice the optical phonon energy) below the excitation. Interestingly, such polarization resolved hot luminescence was observed in III-V semiconductors as well (Zemskii, B and D 1976), although it should be noted that the requirement of valley coherence is absent in III-V semiconductor since we have only one (Gamma) active valley. (Furchi, et al. 2014) (Jones, et al. 2014). The behavior of hot PL of monolayers of WS_2 and WSe_2 also has the same nature. But there are some minor differences in the shape of the blue envelope. This is arising from the fact that each TMD is having different band gap and the shape of the hot PL envelope depends on the band gap of the material. In all the experiments till now, laser excitation used was fixed at 2.33eV.

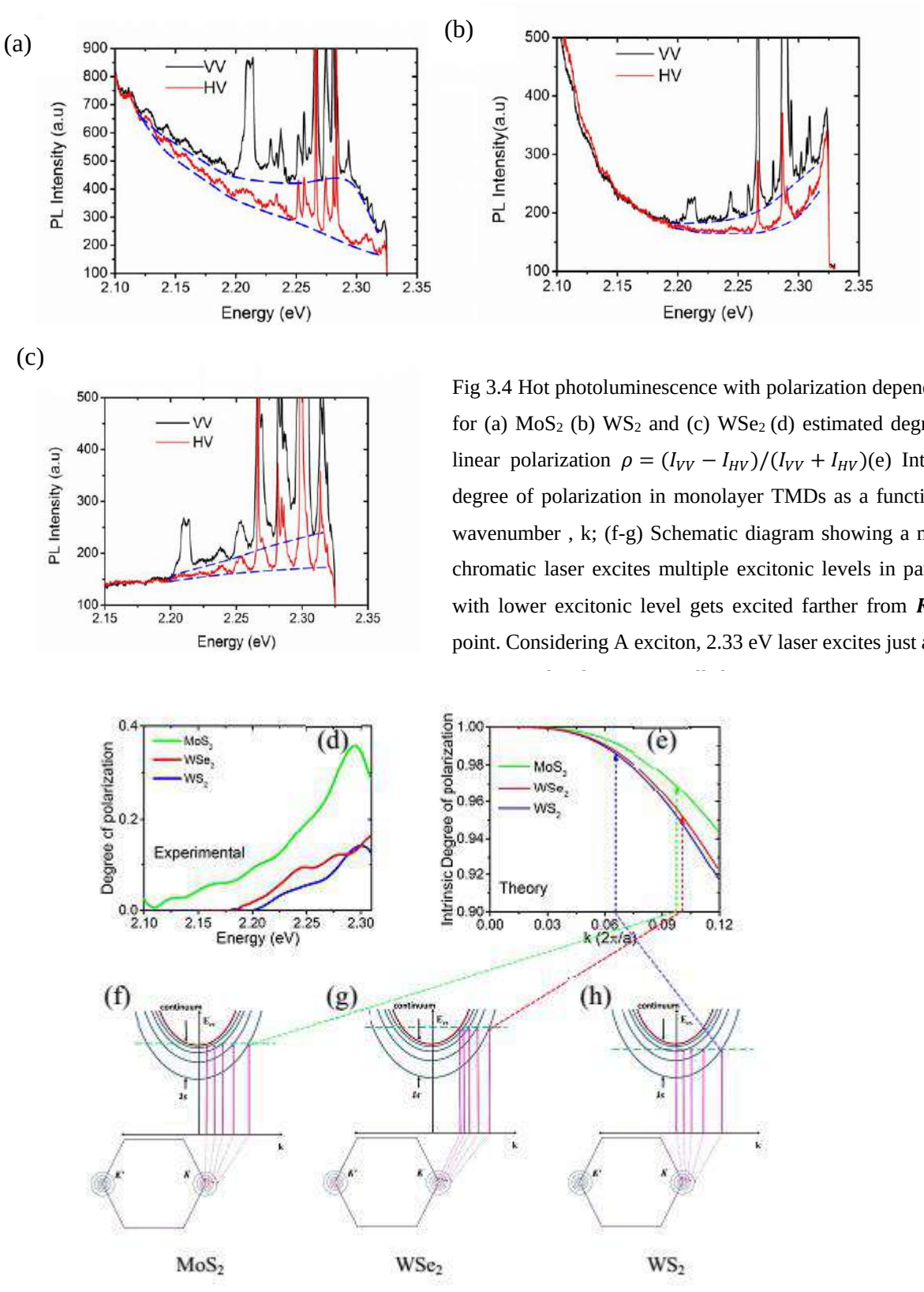

Fig 3.4 Hot photoluminescence with polarization dependence for (a) MoS_2 (b) WS_2 and (c) WSe_2 (d) estimated degree of linear polarization $\rho = (I_{VV} - I_{HV})/(I_{VV} + I_{HV})$(e) Intrinsic degree of polarization in monolayer TMDs as a function of wavenumber , k; (f-g) Schematic diagram showing a mono-chromatic laser excites multiple excitonic levels in parallel, with lower excitonic level gets excited farther from $\boldsymbol{K}(\boldsymbol{K}')$ point. Considering A exciton, 2.33 eV laser excites just above

In Fig. 3.4(f), we schematically show schematically the difference in the excitations for three different materials with the same wavelength (and changing band gap). For parabolic bands, the exciton energy as a function of $\boldsymbol{k} = \boldsymbol{k_e} = -\boldsymbol{k_h}$ can be expressed as

$$E_{ex}(\boldsymbol{k}) = E_g(\boldsymbol{k}) - R_y^* \frac{1}{\left(n_B - \frac{1}{2}\right)^2}$$

with $E_g(\boldsymbol{k}) = E_{g0} + \frac{\hbar^2 \boldsymbol{k}^2}{2m_e^*} + \frac{\hbar^2 \boldsymbol{k}^2}{2m_h^*}$. This is the quasiparticle bandgap at a given k without considering any excitonic effect. Moreover, k is measured from the K (K') points. $E_{g0} = E_g(0)$ is the direct quasiparticle bandgap at the K (K') point. Here we have assumed a Wannier exciton. The calculated Bohr radius of this exciton (~8Å) is larger than the unit cell dimension (~3.193Å) of the crystal. Each excitonic level n_B can have a hot luminescence associated with a corresponding peak, when the excited electrons and holes of same k recombine back radiatively. We should note here that the lower the excitonic level, farther is the excitation point k_{n_B} from the K (K') point, as $k_{n_B} = \frac{1}{\hbar}\sqrt{2m^*(E_L - E_{g0} + \frac{R_y^*}{(n_B - \frac{1}{2})^2})}$ where $m^* = \frac{m_e^* m_h^*}{m_e^* + m_h^*}$ and is the reduced mass of the exciton. For MoS_2, the calculated distance between the A excitation point for 532nm excitation and the K point is ~10% of the size of the Brillouin zone [Fig. 3.4 (e)-(f)]. The corresponding intrinsic depolarization associated with the excitation point being away from K (K') point is calculated to be only 3%. Thus it seems more likely that the hot luminescence associated with each of the exciton branch is linearly polarized and contribute to the signal in Fig. 3.4 (a). However, the observation of the strong peak around 2.29 eV followed by a decay is a signature of strong contribution from band extremum at K (K'). This is because the hot luminescence and its degree of polarization at k≠0 points should exhibit monotonically decaying characteristics from the excitation energy. The B exciton 2s and 3s levels have been reported to be around 2.24 and 2.34 eV (Hill, et al. 2015), hence unlikely to contribute to the peak at 2.29 eV. Based on this, the 2.29 eV peak likely arises due to the A exciton higher energy level. It will lead to an estimated lower bound of the A exciton binding energy to be 0.42 (±0.02) eV.

Similar polarization resolved hot luminescence PL is done for monolayers of WSe_2, WS_2 and $MoSe_2$. The polarization resolved hot luminescence characteristics for monolayer WSe_2 and WS_2 are summarized in Fig. 3.4 (b)-(e) and Fig. 3.4 (g)-(h). All these materials

show the polarization dependence of the hot PL. nonetheless, the nature of hot PL vary from each other depending on the optical band gap of respective materials. For WSe_2, the degree of polarization decreases monotonically from the excitation wavelength. This is probably because there is no band extremum near the excitation. This is in agreement with A exciton band gap of 1.65 eV and binding energy being ~0.3-0.4eV (He, et al. 2014), as schematically shown in Fig. 3(g). By the time we get the exciton 1S peak in PL, carrier undergo series of scattering (in the downward journey in the energy scale because of the high energy excitation) and hence there is a fairly good chance that the polarization is not maintained in the output. We need to remember that our experimental set up has a vertically polarized analyzer at the output side and that the reason why we get the vertical polarization intensity (VV) much more than the horizontal polarization intensity (HV). With lot of scattering, thus, the polarization is lost in the emission, which is clear from Fig 3.4 (a-c), as VV and HV meet each other. On the other hand, in the case of WS_2, with A exciton band gap around 2.05 eV and binding energy of 0.32 eV(Chernikov et al. 2014 Hill et al. 2015). Hence the excitation is below the continuum level [Fig. 3.4(h)], and above the optical band gap. Hence the hot PL still show a polarization dependence but not with any particular peak. The hot PL intensity increases with energy. This hot PL increase is probably going upwards as further more in energy, it is hitting the continuum level. But as the excitation energy is slightly below that continuum level, we are probably missing the show.

So far we have seen various situations where there is an excitation close to continuum level, excitation much above continuum level and an excitation which is between optical band gap and continuum level. Now we turn our attention to a different situation where we excite a material very close to its optical band gap. The PL is expected to be much higher intensity in the case of resonant excitation (like this) as the quantum yield will be very high in this case. We use monolayer $MoSe_2$ (Optical band gap is 1.57eV) in this case. We have used two different laser energies for excitation, i.e., 532nm and 785nm. We have shown the difference between resonant and off-resonant excitation in $MoSe_2$ monolayer. When a 532 nm excitation is used [Fig. 3.5 (a)-(c)], the situation is similar to WSe_2 case. The 1s peak at ~1.57 eV remains unpolarized due to sufficient relaxation through scattering. Also, like other 2D materials, the observed photoluminescence is found to be linearly polarized close to the excitation energy. On the other hand, when the excitation wavelength is changed to 785 nm [Fig. 3.5 (d)-(e)], we resonantly excite the $MoSe_2$ 1s exciton level, which in turn

exhibits very strong (>40%) linear polarization in the photoluminescence. This high polarization dependency indicates that there is a strong valley coherent emission from each K and K' valleys at room temperature. This observation also goes in line with the explanation given in the case of other TMDs. Since resonant PL is happening in this case, carriers undergo very less scattering as there is not much of energy level to release energy to reach the bottom of the conduction band. So radiative recombination with the emission happens much better. Hence it produces high polarization resolved PL. we could observe only the half portion of the 1s peak is observed in Fig. 3.5(e). This is due to the edge filter associated with the system. This filter cuts off the higher energy portion of the PL spectrum

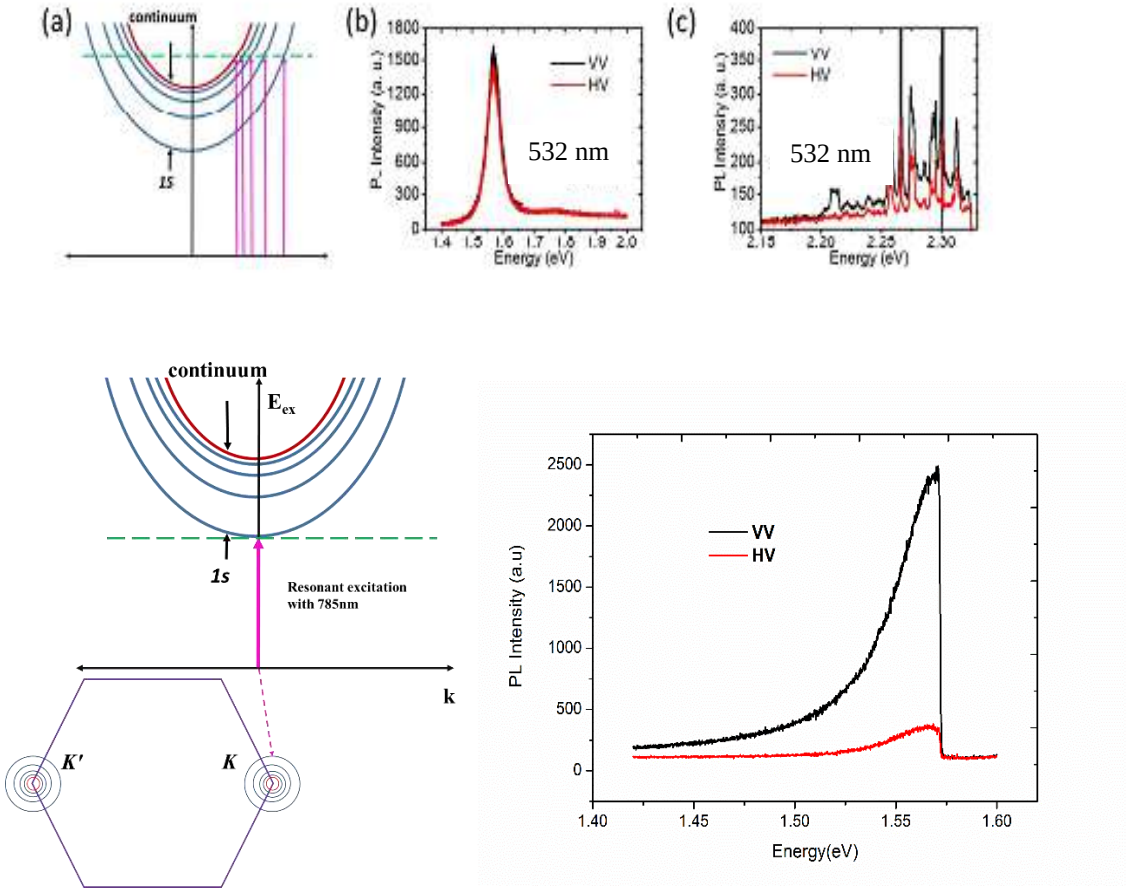

Figure 3.5 Resonant and non-resonant excitation in $MoSe_2$; (a) Schematic of the off-resonant excitation in $MoSe_2$(b) Non resonant PL in monolayer $MoSe_2$ (c)Linearly polarized PL near excitation (d) Schematic of resonant excitation in monolayer $MoSe_2$ (e)Linear polarization resolved PL in monolayer $MoSe_2$

Table 3.1 Comparison of Binding energies of various TMDs monolayers

Sl. No.	Material	A or B exciton	Binding energy (eV)	Method	Ref.
1	MoS_2	B	0.44	PL	Hill et al, (2015)
2	MoS_2	A	0.3	STM	Chiu et al, (2015)
3	MoS_2	A	0.57	Photocurrent	Klots et al, (2015)
4	WS_2	A	0.32	Reflectance	Chernikov et al, (2015)
5	WS_2	A	0.32	PL	Ye et al, (2014)
6	WS_2	A	0.7	Two photon excitation	Hanbicki et al, arXiv:1412.2156
7	WS_2	A	0.79	Reflectance/absorption	Hanbicki et al, arXiv:1412.2156
8	WSe_2	A	0.37	Linear absorption and two photon	He et al, (2014)
9	WSe_2	A	0.4	STM	Chiu et al, (2015)
10	WSe_2	A	0.47	SHG	Wang et al, (2015)
11	$MoSe_2$	A	0.55	STM	Moody et al, (2015)

We can consider the excitation of carriers in TMDC in different steps. (i) Excitation energy less than the optical band gap: In this situation, carriers cannot be excited. (ii) Excitation energy greater than Optical band gap and less than continuum limit: In this situation, carriers are excited. These excited carriers tend to form excitons. The binding energy of excitons are relatively high in these materials because of the very low dielectric constant (which makes Coulombic attraction in exciton much stronger). Hence, upon light irradiation, we

can expect high density of excitons. The optical band gap which we can measure using PL and other techniques like UV spectroscopy, is in fact the 1S level of these excitons. Of course there are many other levels like 2S, 2P etc. for these excitons. But 1S level has the maximum probability of radiative emission. All the higher levels are stacked on top of the 1S level (in energy scale). These energy levels become closer to each other as they go up in energy. Finally, when it goes beyond the binding energy of the exciton, exciton becomes electron and hole plasma. This maximum energy level at which an exciton breaks is the continuum limit. (iii)Excitation energy is above the continuum limit: In this situation, carriers are excited to electron and hole plasma directly. From there it can come down to make excitons as the loose energy because of multiple scatterings (amongst each other and with the lattice).

3.2.2 Carrier temperature estimation from Photoluminescence

Now let's examine the nature of scattering happening for these carriers using hot PL as a tool. We know that above the continuum limit band edge, the PL intensity corresponds to electron and hole plasma. Hence, the corresponding PL intensity $I_P \propto f_e(E_e) f_h(E_h)$where f_e and f_h are the electron and hole distribution functions obeying Fermi-Dirac statistics (with respective quasi-Fermi levels), and the corresponding electron (E_e) and hole (E_h) energies are measured from the conduction and valence band edges, respectively. As energy of the photo-excited carriers are much higher in this regime than the respective quasi-Fermi levels, we obtain (Lyon 1986)

$$I_P \propto e^{[-(E-E_{g0})/K_B T]}$$

Hence,

$$\log(I_P) = \text{constant} - \frac{E - E_{g0}}{K_B T}$$

In the other case, if the excitons in the TMDs are contributing to the hot photoluminescence, the intensity (I_P) of the emission is proportional to the number (n) of excitons which are having that energy. Since number of excitons follows Bose-Einstein distribution for energies $E \gg K_B T$, we can see that:

$$\log(I_P) = \text{constant} - \frac{E}{K_B T}$$

From the above equations, it reveals that without depending on the origin of the luminescence, whether it is originated from e-h plasma or excitons, the hot photoluminescence, especially the tail of the hot photoluminescence, associated with the PL peaks are expected to decay exponentially with energy. Also, by from the plot between log (I_P) and E, the carrier temperature can be calculated.

In Fig. 3.6, the carrier temperature is extracted from the tail of 2.29 eV peak. It is coming to 510 (±10) K for an incident laser power of 0.26 mW. This peak is due to the hot PL and this corresponds to the carrier temperature before relaxation through optical phonons. The possible methods of relaxations at this point are through carrier-carrier and carrier-acoustic phonon scattering. So by the time carriers reach up to A peak of the PL, it would have lost substantial amount of energy and hence the calculated temperature at this position will be less than the previous value. Substantiating this, the temperature extracted from the tail of the A peak by this method (at 1.87 eV) is 363K±3K. When we had reduced the power of the incident laser to 0.026mW, we saw that there is a reduction in the extracted temperature of the A exciton and now it is around 290K (inset of Fig. 3.6). This temperature is the laboratory ambient temperature. We have observed that the TMDs get heated up and often times burns upon 0.26mW laser irradiation. But at low power, we don't observe any burning of this kind. Our measurements shows that there is no substantial heating happening at this instant. Though this reduction in temperature is with power is very intuitive, our method of extraction of temperature for corresponding power from the slope of hot photoluminescence is very unique. This can be used as a probe to measure the temperature at various instances where normal temperature measurements are not possible.

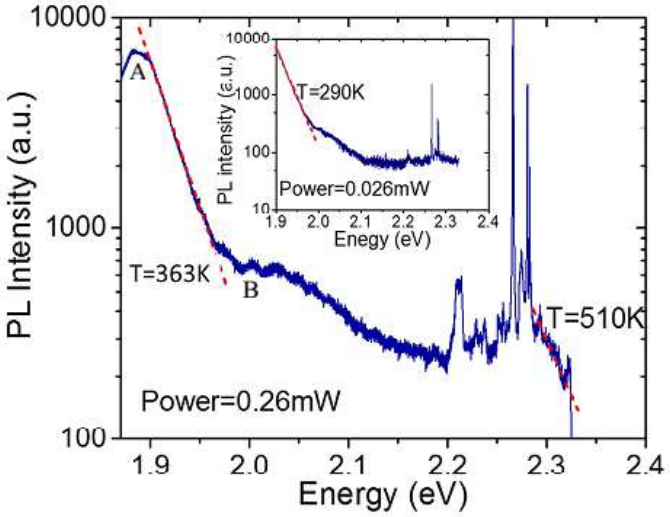

Figure 3.6 Carrier temperature extraction from hot luminescence tail of MoS2 (inset) Extracted carrier temperature for 0.026mW laser power

There are two reasons because of that the above method of extraction of carrier temperature in this method can be ambiguous. First, if there is a proximity of any other peaks near the main peak, it may flatten the hot luminescence tail. Now the extracted carrier temperature will be overestimated. Hot luminescence peaks should be properly deconvoluted in this case before extracting the carrier temperature. Second, in this calculation, we assume that the broadening of the photoluminescence peak results in the Boltzmann-type tail only. But actually case is that there are other inhomogeneous contributions to this tail from excitation-induced and phonon-induced PL broadening (Mouri, et al. 2014). Nonetheless, near to the room temperature, we see that the hot luminescence is still the main mechanism which causes the broadening of the hot luminescence. This also makes sure that the carrier temperature extraction by this method is fairly accurate. However, for better temperature extraction at low temperatures, one should subtract appropriate correction factors arising from other broadening mechanisms.

To prove the above point where one should be careful in applying the technique of temperature extraction from the luminescence tail, when multiple peaks are in close proximity, we have fabricated a MoS_2 device with FET architecture as show in Fig 3.7. This type of a situation occurs when the MoS_2 sample is doped which results in a trion peak and an exciton peak with a separation of ~30 meV. We fabricated a FET with MoS_2 channel. Substrate Oxide was used as the dielectric for applying gate field. Two electrodes with Chromium/ Gold (Cr/Au) with thickness of 5 and 50nm respectively was realized using a combination

of electron beam lithography and metal lift off. Metal deposition was done by electron beam evaporation. Bottom of the substrate is coated with Aluminium. We applied an external bias of 1V across the top metal electrodes, which will function as source and drain. Constant gate voltage is applied at the bottom. Depending on the polarity of the gate bias, it changes the charge concentration in the channel. If we apply a positive bias at the gate, it will make the channel n-type by creating a sheet of electrons in the channel to counter this positive field. Similarly, p-type doping will ideally occur if we apply a negative bias at the bottom (though p-type doping of MoS_2 is not very effective by gate). In Fig. 3.7 shows such an example where the sample was initially n-type doped. The PL peak around 1.845 eV has a primary contribution from the trion peak, with a small contribution from the exciton, which flattens the slope significantly. When we apply a negative bias from the back gate, the effective doping in the sample is reduced, and we are able to suppress the trion peak, blue shifting the PL peak by around 30 meV, and now the slope has primary contribution from the exciton – hence the extracted temperature will be more accurate.

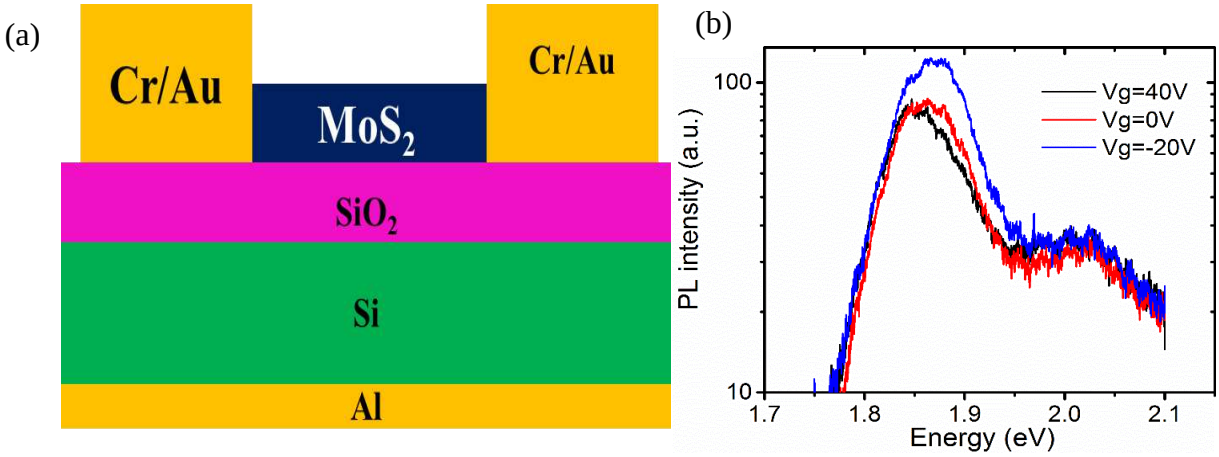

Fig 3.7 effect of doping of the channel in the temperature estimation (a) Schematics of the FET device fabricated with MoS_2 as channel and bottom gate architecture (b) normal PL spectra taken at various gate voltages

3.2.3 Lattice temperature estimation from Raman scattering

The photo-carriers relax from the excited coherent state to the incoherent 1s state through emission of optical phonons. It is know that the optical phonons cannot transport the heat which it has acquired from the carriers very efficiently because of its poor group velocity (from the energy dispersion relation for optical phonons, which is a flat line parallel to the energy axis). Generally, these optical phonons decay through the acoustic phonons. This

will give rise to anharmonic effects in the measurements. This anharmonic effects are mainly shows as a broadening (Γ) and a red shift (ρ) of the Raman peak:

$$I_R \propto \frac{\Gamma(T)}{[\omega_0 + \rho(T) - \omega]^2 + \Gamma^2(T)} \times [n(\omega, T) + 1]$$

where ω_0 is the peak without any anharmonic effect and n(ω,T) is the Bose-Einstein occupation number. In Fig. 3.8(a), we have plotted the Raman intensities taken at different incident laser powers. This measurement shows a red shift and broadening of both A_{1g} and E^1_{2g} peaks. We see in [Fig. 3.8(b)-(c)] that the broadening and red shift associated with A_{1g} peak is more when compared with that of E^1_{2g} peak. This observation goes in line with the fact that the out of plane A_{1g} phonon is the primary contributor to electron-phonon scattering (Kaasbjerg, Thygesen and Jacobsen 2012), particularly at lower laser powers. However, at higher incident power, we see that the E^1_{2g} phonon branch also start as another channel for energy relaxation in the lattice.

As long as the energy and momentum of the electrons are conserved, there are many different choices of phonon combinations through which an optical phonon can decay. We choose only those phonon combinations which possess relatively large density of states (Sanchez and Wirtz 2011), and use a modified Klemens model (Klemens 1966) for modeling the peak broadening. Full Width Half Maximum (FWHM) of the A_{1g} peak is obtained as:

$$\Gamma(T) = \Gamma_0 + 2\alpha n^{LA(M)}(244, \sigma_1 T) + 2\alpha n^{TA(M)}(160, \sigma_2 T) + 2\beta n^{LA}(202, \sigma_3 T) + 2\gamma n^{E'}(384, \sigma_4 T) + 2\gamma n^{LA,TA}(20, \sigma_5 T)$$

where Γ_0 is the broadening due to background, and the superscripts in n indicate the respective phonon branches. σ_i T (with $\sigma_i<1$) is the temperature of the i^{th} phonon branch where the energy is transferred to. The red shift of the Raman peak follows a linear relationship with a change in the temperature: ρ (T) =ξΔT. Taking the peak position at a laser power of 0.026 mW to correspond to 290 K and using the value of ξ (=-1.30e^{-2}cm^{-1}K^{-1}) for the A_{1g} peak from recent literature (Yang, et al. 2014), we first estimate the temperature of the A1g phonon branch. Next, with the estimated temperature, we find that we can self-consistently fit the FWHM data at the corresponding laser powers [Fig. 3.8(d)]. The best fit is obtained with Γ (0) =0.96, α=0.94, β=0.04, γ=0.02. This shows that the primary relaxation path are the phonon branches at the M point. Also, we obtained σ (1) =σ (2) =1 implying that the

temperature of the A1g phonon is almost equal to the decaying acoustic branches, which is in agreement with the fact that these acoustic branches at the M point are almost flat possessing very small group velocity (Molina-Sánchez and Wirtz 2011)and thus cannot carry away the heat efficiently, rather in turn transfer the heat to other acoustic branches. The extracted A_{1g} and E^1_{2g} temperatures at different laser powers are plotted in Fig. 3.8(e).

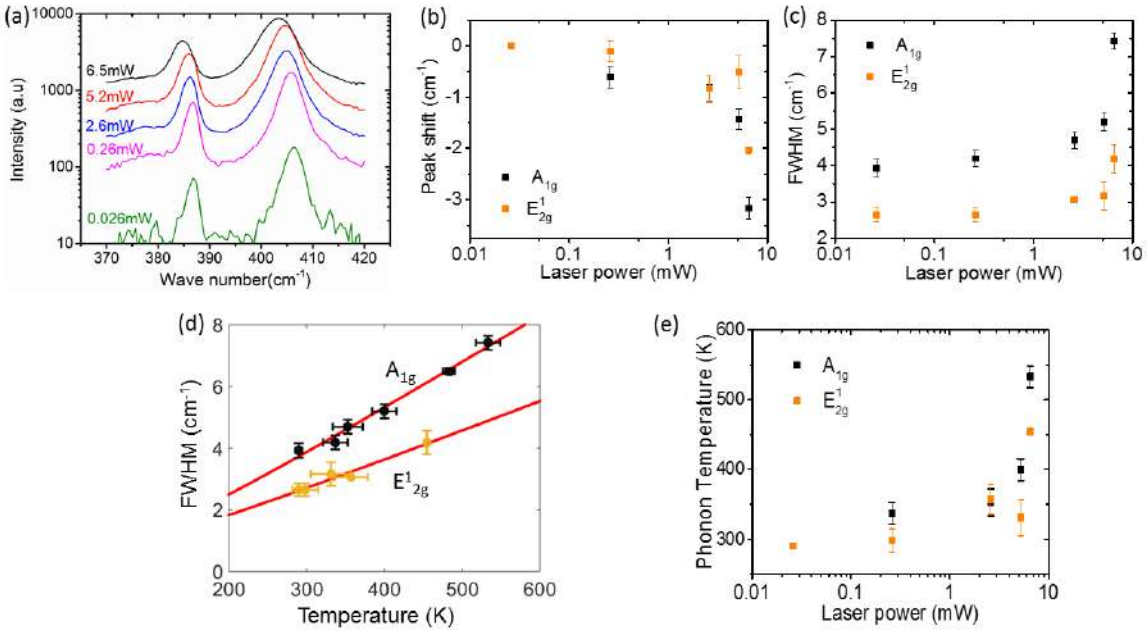

Figure 3.8 (a) Raman spectra at different incident powers (b)-(c) Peak red shift and change in FWHM with different powers(d) Fitting of the phonon temperature and FWHM (e) Calculated phonon temperature with varying laser powers

The complete process of exciting TMDs with linearly polarized light can be thus describes as follows. The linearly polarized light is a linear combination of LCP and RCP. This gives rise to the excitation from both K and K' valleys of the Brillouin Zone. The electrons take this energy and goes to a higher energy level in the conduction band. This high energy acquired by these electrons will increase the carrier temperature in the system. We have calculated this temperature as 510K for an excitation laser power of 0.26mW. There is a hot photoluminescence from this high energy level and we have seen that this is a polarized light emission. The K and K' points emit RCP and LCP which combine together to produce a linearly polarized light at the output. The heat energy of carriers is relaxed by giving the excess energy to the lattice in the form of acoustic phonons. These changes can be seen from the Raman line width broadening. We extract the lattice temperature from the Raman line width broadening and it is close to 337K for an excitation laser power of 0.26mW. The

1S level of the exciton is a good meta-stable state for most of the electrons. So after all the above relaxation, they will settle at this point. From here, it will undergo electron-hole recombination by radiative transition. As it is very evident, the emission in this case will be un-polarized light.

To check the consistency of temperature measurement by measuring the tail of PL spectrum, we have repeated the same experiment with reduced laser power. When the laser power was reduced to 0.026mW, the temperature of the carrier from the normal PL spectra was estimated to be 290K, which is the laboratory temperature in our experiments. Hence, such a low power excitation does not heat the TMD material during measurements. This observation is also in accordance with the common observation of burning of TMD monolayers while irradiating with laser light for long. Even in our experiments also, we have seen that TMD monolayers are burnt after a while, if laser light of power 0.26mW or more is applied for long. But nothing of this kind has been observed for PL measurements with very low power.

Schematic of the above description in shown in the figure below.

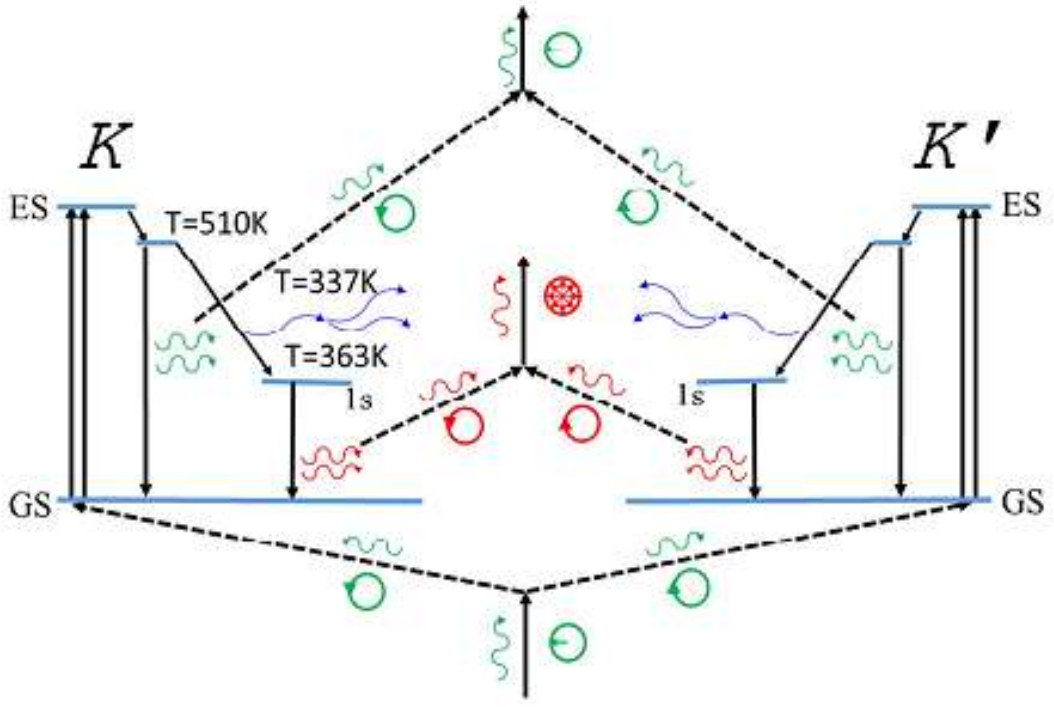

Fig 3.9 Schematic of the excitation of carriers in monolayer TMDs and subsequent relaxation

3.3 Conclusions

In conclusion, using off-resonant excitation, we demonstrated linear polarization resolved hot photoluminescence at room temperature in monolayer MoS_2, $MoSe_2$, WSe_2 and WS_2 reflecting valley coherence close to excitation energy due to lack of sufficient optical phonon scattering. We have also shown strong room temperature valley coherence in monolayer MoSe2 by resonantly exciting the 1s peak at energies close to excitation. Generation of valley coherence is important from the point of view of Valleytronics, where manipulation of valley degree of freedom by external stimulation is required. Hence demonstration of such coherence at room temperature, on one hand, is technologically important due to increased hopes for room temperature Valleytronics, and on the other hand, makes laboratory experiments more flexible in terms of laser wavelength and sample temperature requirements. We also found the lower bound of the A exciton binding energy in monolayer MoS_2 has been extracted to be ~0.42 (±0.02) eV. Using a combination of hot luminescence tail and anharmonic effects in Raman peaks, the extracted steady state temperature of the carriers before optical phonon relaxation, after relaxation to 1s level and that of the emitted A1g optical phonons are 510 (±10) K, 363 (±3) K, and 337 (±15) K respectively, for an incident laser power of 0.26 mW on monolayer MoS_2. Such in-situ and non-destructive extraction of temperature of the carriers as well as the different phonon branches is important as it is generally non-trivial to directly find out the temperature of the electron (or hole) and phonon systems separately in the semiconductor under non-equilibrium. The technique can also be easily extended to other systems as well, for example in devices under high electric bias.

Chapter 4

Photoresponse of atomically thin MoS_2 layers and their planar hetero-junctions

Overview:

Chapter 4 analyses the various factors which affect the performance of TMD based photodetectors. This is realized by fabricating photodetectors with MoS_2. The different processes behind the photocurrent generation in MoS_2 based photodetectors with uniform channel thickness is studied. The influence of in-plane heterojunction in the photocurrent generation is also studied. Further, a fast photoresponse of the photodetectors with heterojunction made of MoS_2 is demonstrated.

4. Photoresponse of atomically thin MoS_2 layers and their planar heterojunctions

Two dimensional transition metal Dichalcogenides(TMDs) have emerged as highly promising next generation materials for future optoelectronic application (Choi et al. 2012 Eda and Maier 2013 Lopez-Sanchez et al. 2013 Roy et al. 2013b Yu et al. 2013 Baugher et al. 2014a Koppens et al. 2014 Pospischil et al. 2014 Pradhan et al. 2015 Rathi et al. 2015). MoS_2 is one of one of the leading candidates in this class of materials and has attracted a lot of attention from many researchers. bulk MoS_2 is an indirect bandgap material with a bandgap of ~1.3 eV and its monolayer MoS_2 exhibits a direct optical(excitonic) bandgap of ~1.9 eV, which is measured from the photoluminescence measurements and first principles calculations (Splendiani et al. 2010 Ramasubramaniam 2012). The direct bandgap in monolayer MoS_2, along with its excellent light absorption(10% in monolayer), makes it interesting for light detection applications (Lee et al. 2012 Yin et al. 2012 Lopez-Sanchez et al. 2013 Zhang et al. 2013 Koppens et al. 2014 Kufer and Konstantatos 2015). However, monolayer MoS_2 exhibits extremely large exciton binding energy(Hill et al. 2015). Hence the photogenerated electrons and holes will still be in the bound state. This would make the photovoltaic properties (which is one of the main properties used for light detection) of MoS_2, very week. MoS_2 devices characterized with scanning photocurrent microscopy(SPM) have revealed that there is a strong photoresponse at the metal-MoS_2 junction, which is due to photothermoelectric effect (Buscema et al. 2013b). In the case of multilayer MoS_2 photoresponse, different mechanisms, including photoelectric effect, photothermoelectric effect, and hot electron injection have been suggested (Wu et al. 2013 Furchi et al. 2014 Wi et al. 2014 Hong et al. 2015). Moreover, TMDs based metal/semiconductor/metal (MSM) photodetectors which are fabricated on oxide very exhibit slow transient response (recovery in few seconds or even in minutes). This limits the practical application of such devices in fast photo-detection applications. Hence, an understanding of the fundamental

mechanisms which are responsible for such slow response, and a design procedure to obtain TMDs based high speed photodetector will be very useful.

Apart from these planar metal-semiconductor-metal (MSM)photodetectors, different vertical heterojunction devices have also been studied (Britnell et al. 2013 Hong et al. 2014 Lee et al. 2014 Lopez-Sanchez et al. 2014). similar studies in planar heterojunction devices is lacking in the literature and have recently started to attract attention (Howell et al. 2015 Tosun et al. 2015). Changing number of layers along the channel of TMDs results in an abrupt heterojunction due to thickness dependent electronic properties of MoS_2. In this work, we exploit this fact to fabricate planar monolayer/bilayer heterojunction and monolayer/few-layer/multi-layer double heterojunction MoS_2 devices. We have used monolayer and bilayer devices as references devices. We systematically study their photoresponse and transient response using scanning laser excitation to elucidate the fundamental mechanisms involved. We show that the in-plane heterojunction photodetectors can be appropriately designed to obtain fast photo-detection by reducing hole trapping which happens near the source junction in SiO_2.

4.1 Device fabrication and experimental set up

Thin MoS_2 layers are exfoliated on a cleaned Si wafer on which 285 nm thick SiO_2 layer is grown. The thickness of the MoS_2 flake is determined by optical microscope (as this substrate gives better contrast). Thickness of the layers is cross checked also by measuring the separation between the A_{1g} and the E^1_{2g} Raman peaks. Raman, Photoluminescence and AFM characterization of the samples are provided in Fig 2.1. The MoS_2 layer are then patterned by electron beam lithography followed by etching for 20 s in BCl_3 (15 sccm) and Ar (60 sccm), with an RF power of 100W and chamber pressure of 4.5 mTorr. This step is done to make the flake in the shape of a rectangular strip so that there is no shape dependent characteristics (like current crowding) in the photocurrent measurements. In the next step lithography, contact pads are defined, followed by 5 nm/45 nm thick Cr/Au deposition using electron beam evaporation which is followed by metal liftoff in Acetone. No post metallization annealing was performed in these devices. The wafer is then bonded to a PCB using an Aluminium wire with the help of wire bonder. Photocurrent measurements were performed at room temperature. A 532 nm (2.33 eV) green laser was passed through a 100X objective and the sample stage was moved so as to scan the diffraction limited laser spot

from the source to the drain. The source is always kept grounded, and the drain is biased using a source meter (Keithley 2450).

4.2 Material characterizations

MoS_2 flakes are having high optical contrast on 285nm SiO_2 substrate. So these flakes can be easily identified with an optical microscope. Apart from this, MoS2 has peculiar Raman peaks whose positions change with the layer number. Number of layers of these flakes can be determined by corresponding Raman spectra. If the difference between two peaks in the Raman spectra is $19cm^{-1}$, it corresponds to a single layer flake. This difference increases as the number of layers increases.

Photoluminescence (PL) is also used to characterize these flakes. As the monolayer MoS_2 flakes are direct band gap in nature, it shows very high PL intensity around 1.85eV, which is the monolayer band gap. As the number of layers increases, it becomes an indirect band gap material and hence the PL intensity reduces. Also, we should note that the PL peak position red shifts as the number of layers increases. This is due to the change in the band gap with change in the number of layers of TMDs, as discussed in the previous sections.

Further, Atomic Force Microscopy (AFM) is used to measure the layer thickness. A clear step is visible at the interface between (i) single layer to SiO_2 (ii) single layer and bilayer and (iii) single layer-few layer-multi layer flakes. The thickness of a monolayer is coming around 0.8nm from these measurements.

Fig 4.1 shows Raman spectroscopy, Photoluminescence and AFM of MoS_2 flakes. Fig 4.1 (c) shows the variation in the PL intensity with the change in the number of layer in the case of 1L/2L layer junction. Fig 4.1 (e) shows the variation in the PL intensity with the change in the number of layer in the case of 1L/few layer/Multi-layer junction. Fig 4.1 (d) and 4.1 (e) are the thickness measurement of heterojunctions using AFM.

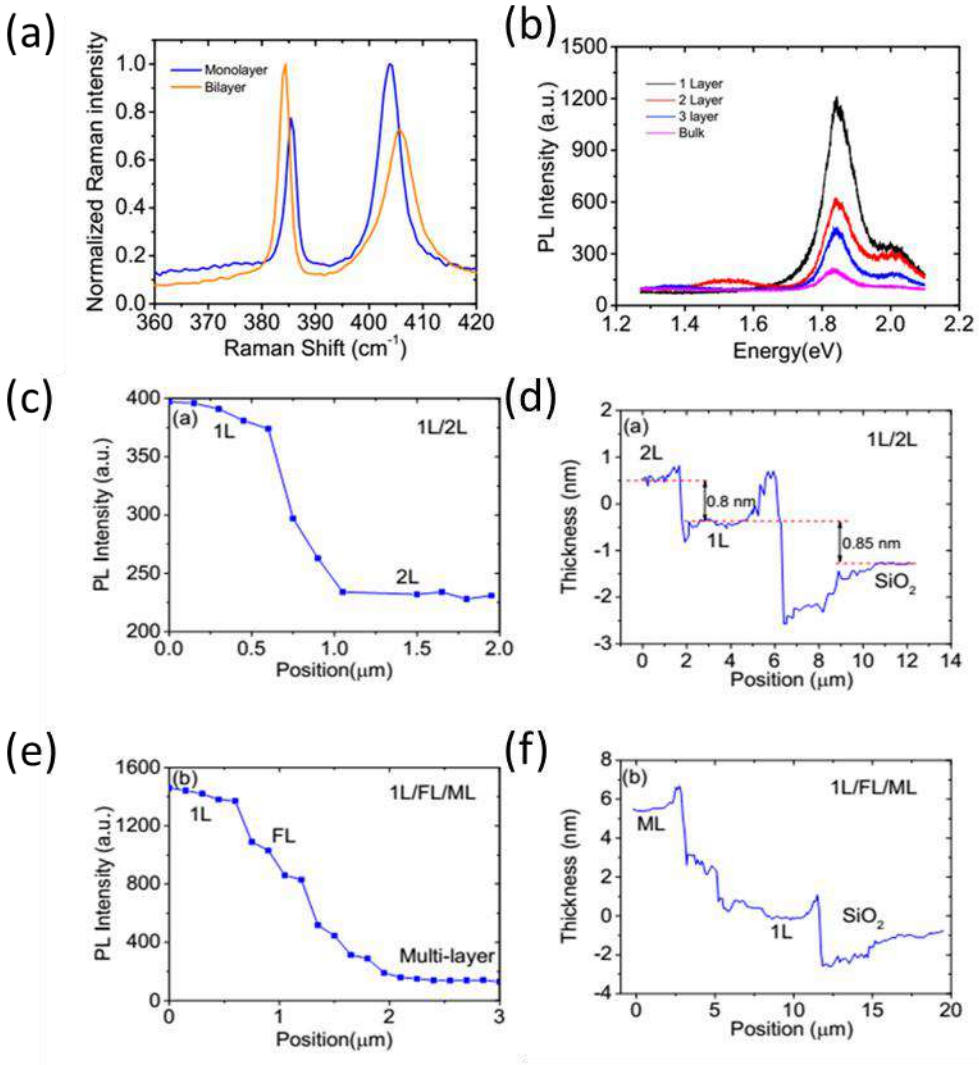

Fig 4.1 material characterization of MoS_2 (a) Raman spectra of the different layer (b) PL spectra of different layers (c) PL intensity map of the 1L/2L junction (d) AFM image of 1L/2L junction (e)) PL intensity map of the 1L/Few layer/Multi-layer junction (f) AFM image of the 1L/Few layer/Multi-layer junction

4.3 Results and discussions

4.3.1 Photoresponse of uniform channel - monolayer (1L) and bilayer (2L): Role of hot photo-electron injection

Fig 4.2 (a) shows the schematic of the experimental set up used for the photocurrent measurements. A laser spot from is 100X objective is used for all the photocurrent measurements. The two terminal device as shown in the Fig 4.2 (a) is biased using an external source meter and corresponding current is measured. The position of the laser illumination on the device was changed by moving the stage. In out experimental set up, the stage on which devices are kept was able to move in steps of 100nm. Photocurrent mapping with

laser illumination at various positions of the device could give insights to the underlying mechanism of photocurrent generations. Fig. 4.2(b)-(c) spatially resolved photocurrent characteristics for a monolayer MoS_2 device at different drain voltages (V_{ds}). There are different mechanisms by which the photoresponse can happen. It mainly includes Photoelectric effect, Photo-thermoelectric effect and metal induced hot electron injection. Here these three photocurrents are denoted by $I^E_{e,h}$, $I^S_{e,h}$ and $I^P_{e,h}$ respectively. We have used scanning photocurrent measurement is used to measure the relative contribution of each of these currents. The subscripts (e, h) correspond to electron and hole currents.

when the laser is focused at the middle of the channel, photocurrent is found to be small. Photo-thermoelectric effect will be negligible at the center of the channel because it needs different materials (change in the Seebeck coefficients). At the center of the channel, hence, the photocurrent is dominated by photoelectric effect. The observation of small photocurrent at the center of the channel indicates that intrinsic photoelectric effect in monolayer MoS_2 is very weak. It is seen that because of the strong out-of-plane confinement, small dielectric constant and large carrier effective mass in monolayer MoS_2 results in extremely high exciton binding energy (~0.4 eV) (Hill et al. 2015). This is shown in Fig. 4.2(d)-(e)].

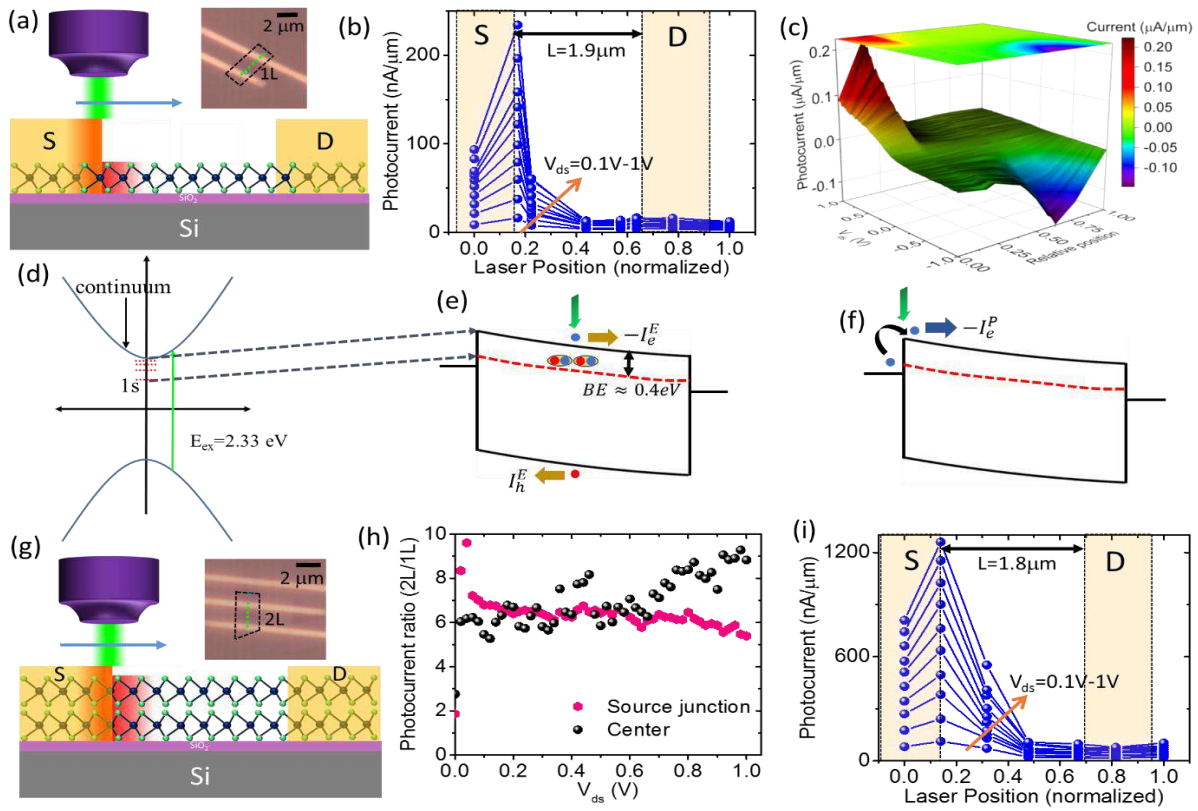

Figure 4.2 Photoresponsivity of MoS_2. (a) Schematic of the scanning photocurrent measurement setup with monolayer MoS_2 device, with L = 1.9 μm and W = 2 μm. The laser power used is 2.6 μW. Inset: Optical microscope image of the device. (b) Photocurrent measured as the laser spot is scanned from the grounded source (S) to the drain (D). Each line corresponds to a different V_{ds}, varying from 0.1 V to 1 V, in steps of 0.1 V. (c) 3D plot of the photocurrent as a function of V_{ds} and the normalized laser position in the device. The color plot projection is shown at the top. (d) Schematic diagram of parabolic band structure of MoS_2 with different excitonic states. 2.33 eV excitation creates hot electron-hole pairs which are ~ 0.215 eV higher than the A_{1s} state. (e)-(f) Band diagram of monolayer MoS_2 at positive V_{ds}, with laser beam (green arrow) focused at the (e) center of the channel, and (f) at the source junction. The solid lines indicate band extrema with no excitonic effect (continuum, representing electrical band gap), while the red dashed lines indicate lowest excitonic state (A_{1s}), with a binding energy BE ~ 0.4 eV. The dark golden arrows indicate direction of carrier flow of due to external bias induced drift-diffusion. The blue arrow indicates electron flow due to hot electron injection from metal. (g) Schematics diagram of uniform bilayer device with L = 1.8 μm and W = 1.9 μm. The laser power used is 2.6 μW. Inset: Optical microscope image of the device. (h) Photocurrent ratio between bilayer and monolayer devices, with the laser spot at the source junction and at the center. (i) Photocurrent measured as the laser spot is scanned from the grounded source (S) to the drain (D). Each line corresponds to a different V_{ds}, varying from 0.1 V to 1 V, in steps of 0.1 V.

So large electric field is needed to separate the photo-generated electrons and holes efficiently. MoS_2 layers are contacted by metals at both sides. This metal electrodes will try to bend the bands in MoS_2. But band bending of this kind will not be efficient in this case because (i) MoS2 layer is very thin and (ii) Doping concentration of MoS_2 is less. So the presence of metal electrode will result in quasi linear (or linear) band profile in MoS_2 as suggested by Poisson's equation. This results in a quasi-linear band profile as shown in in 4.2(e)-(f). The lowest energy excitonic level (A_{1s}) is shown by the red dashed line. The resulting electric field due to band bending is two orders of magnitude lower than the field required to break the exciton.it needs ~5 MV/cm, assuming a Bohr radius of ~8Å . This results in a relatively weak photoelectric effect, in spite of excellent light absorption properties.

Now the photocurrent is measured when the laser falls at the source metal-Mos_2 junction. Photocurrent increases sharply when the laser is focused at the point between the edge of the metal electrode and the MoS_2. Based on the above discussion of quasi-linear band profile, the electric field close to the metal junction cannot be dramatically different from the center of the channel. Hence the contribution from photoelectric effect to the total current also will not be dramatically high. Hence, such photocurrent enhancement at the source

junction cannot be explained by the photoelectric effect. On the other hand, strong photo-thermoelectric effect has been observed at metal-MoS_2 junction (Buscema et al. 2013b) as monolayer MoS_2 exhibits a larger Seebeck coefficient ($|S_{1L}| \sim 10^3 - 10^5 \mu$V/K depending on gate voltage) than that of the metal. However, in our devices, we observe strong external bias dependence of the photocurrent at the source junction. Since the thermoelectric effect should be independent of external bias, it is difficult to explain the enhancement in the photocurrent purely from photothermoelectric effect, particularly at large V_{ds}.

Hot electron injection from the metal electrode is the other effect which can play a role. The strong photocurrent at the metal junction can be explained by hot photo-electron injection from the metal to the channel region. When the laser shines at the source junction, the electrons from the metal tend to diffuse into the channel because of the bias. However, this requires the electrons to overcome the Schottky barrier between metal and the channel at the source junction, as explained in Fig. 4.2(f). The origin of the Schottky barrier at the source junction can be explained as follows: photons create excitons in the channel and these excitons cannot be driven electrically as they are neutral particles. So, in order to have conduction electrons, it is necessary for the electrons from the metal to jump from metal Fermi level to the states in the MoS_2 channel that are close to or above the continuum level of the exciton as shown in Fig. 2(d). This corresponds to a barrier height in excess of a few $K_B T$. It is very difficult for the electrons which are already in quasi-equilibrium with the laser heated metal lattice, can overcome this potential barrier. On the other hand, with the absorption of 2.33 eV photons of the green laser, hot photoelectrons can be generated in the metal-MoS_2 junction, which can efficiently cross over the potential barrier into the channel(Hong et al. 2015). Once an electron has sufficient energy to cross this barrier, it can be driven by the external bias. This results in bias dependent large photoresponse. On the other hand, a reverse electric field diminishes the photocurrent substantially because at this time, the laser spot is at the drain junction.

The scanning photocurrent results from a bilayer device are summarized in Fig. 4.2(g)-(i). Fig. 4. 2 (h) shows that depending on the position of the laser spot and bias condition, the bilayer device exhibits 5- to 10-fold improvement in photocurrent compared with the monolayer device. When the laser spot is falling at the center, the enhancement in the photocurrent can be attributed to: (i) increased light-matter interaction length in bilayer because of the extra thickness coming from the bilayer (ii) enhanced photoelectric effect, owing to

reduced excitonic binding energy (Cheiwchanchamnangij and Lambrecht 2012 Komsa and Krasheninnikov 2012); and (iii) reduced series resistance in bilayer owing to improved mobility and contact resistance of metal bilayer junctions (Yang et al. 2014b).

So, when the laser spot is falling at the source metal edge, the photocurrent is the strongest, as shown in Fig. 4.2(i). We note from Fig. 4.2(h) that at this laser position, the photocurrent is 5- to 7-fold higher than that of the monolayer device. The peak photoresponsivity of this device corresponds to 921 mA/W at V_{ds} = 1 V and 2.6 μW incident power. Such an enhancement of the photocurrent in bilayer device over monolayer supports the explanation of metal hot photo-electron injection as the mechanism of photocurrent generation. This is due to the fact that bilayer MoS_2 does not exhibit dramatically different Seebeck coefficient than that of monolayer (Wickramaratne et al. 2014 Hippalgaonkar et al. 2015 Yoshida et al. 2016), and hence we do not expect much larger thermoelectric effect than the monolayer case. On the other hand, bilayer MoS_2 offers more efficient in hot carrier injection into the channel, due to two reasons: (i) bilayer offers reduced Schottky barrier height for the photo-induced hot electrons from metal to channel, resulting from its relatively weaker exciton binding energy and (ii) the electronic coupling between the metal and the bilayer is better than the monolayer case. The better electronic coupling is the result of the delocalization of the spatial distribution of the electron wave function at the conduction band minimum. the band minimum point moves away from the K or K' point in monolayer to inside of the Brillouin zone in bilayer or multi-layer (Splendiani et al. 2010).

4.3.2 Photoresponse of monolayer/bilayer (1L/2L) heterojunction

Next, consider the photoresponse of a 1L/2L single heterojunction device photoresponse. The SEM micrograph of a typical heterojunction is shown in Fig. 4.3(a), indicating sharp junction between monolayer and bilayer. In Fig. 4.3(b), is plot which shows the spatial distribution of the separation between the A_{1g} and E^1_{2g} Raman peaks, which is commonly used to distinguish monolayer and bilayer MoS_2 (Lee et al. 2010). Further characterization of monolayer/bilayer heterojunction is performed using photoluminescence and atomic force microscopy (AFM) (see Fig 4.1). The scanning photocurrent response of such a heterojunction device [schematically shown in Fig. 4.4(a)], is plotted in Fig. 4.4(b)-(c). Due to strong out of plane quantum confinement of carriers in these ultra-thin two dimensional films, the bandgap changes appreciably with thickness of the layer, as explained earlier. For example, the excitonic gap of 1.9 eV in monolayer changes to 1.6 eV in bilayer. Also,

this is coupled with the fact that monolayer has stronger exciton binding energy than bi-layer, which again results in an even larger electrical bandgap difference(as optical band gap is less than the electrical band gap by an amount which is equal to excitonic band gap).

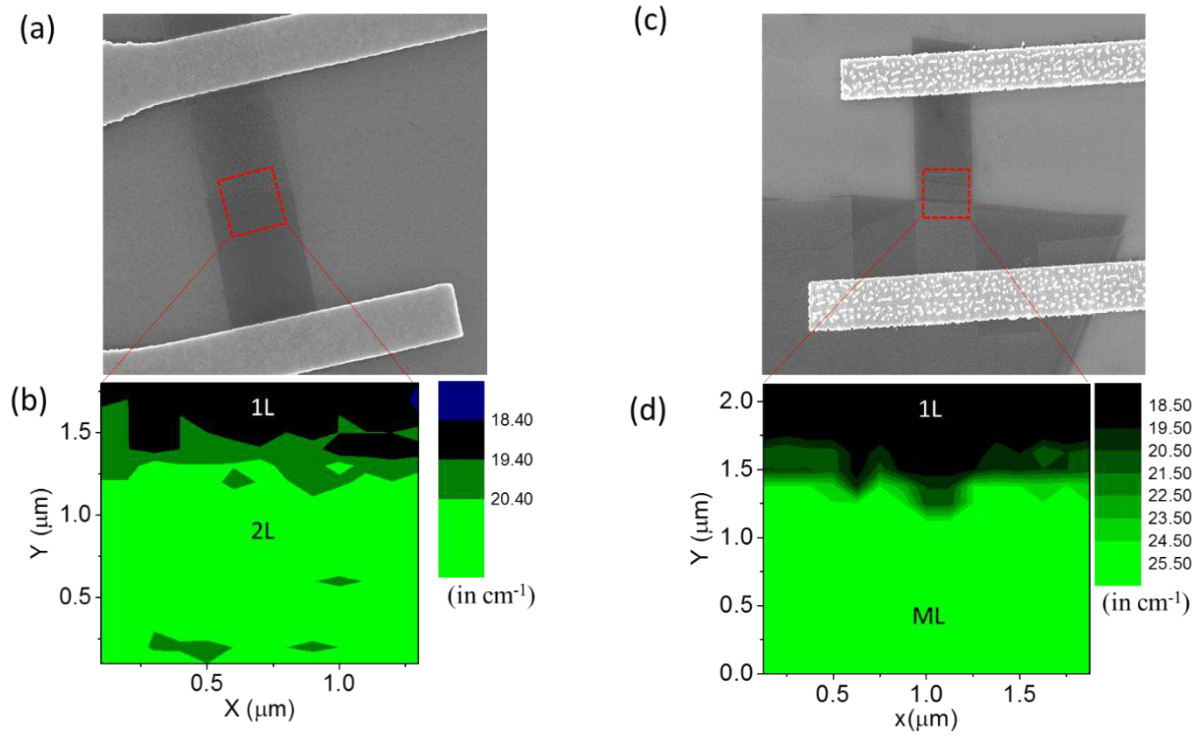

Fig 4.3 Characterization of MoS_2 heterojunctions. (a) SEM micrograph of a monolayer/bilayer heterojunction device. (b) Raman spectroscopic mapping in the highlighted region, where the spatial distribution of the difference between A_{1g} and E^1_{2g} peak positions are plotted, which indicate the monolayer and bilayer portions of the flake. (c) SEM micrograph of a monolayer/few-layer/multi-layer MoS_2 double heterojunction device. (d) Raman spectroscopic mapping of the device in (c) characterizing the number of layers along channel length.

A change in number of layers along the channel, thus, modulates the bandgap. Typically, the vertical heterostructures made out of different TMDs show Type-II band alignment. But in-plane monolayer/multi-layer junction has been shown to exhibit Type-I band alignment (Tosun et al. 2015), with the band offset being very small for conduction band and large for valence band. To explain the observed photocurrent characteristics, we solve Poisson equation for the heterostructure device, and the obtained the band diagrams are shown in Fig. 4.4(d)-(f). The energy scale in the band diagrams is kept in arbitrary unit since the different band-offsets and electrical band gaps are not precisely known.

For the case$V_{ds} > 0$, the peak photocurrent is observed when the laser falls right at the 1L/2L junction. This shows the significant role of the heterojunction. To understand this in much detail, the different components of the total photocurrent are shown in Fig. 4.3(d). The built-in potential step at the heterojunction helps to spatially separate the photo-excited hot electrons and holes. This is done by inhibiting exciton formation in the monolayer. The electron current (I_e) and hole current (I_h) thus created are asymmetric due to different built-in potentials in the conduction and the valence bands (Type-I arrangement). The total current in the channel is thus given by $I = I_e + I_h = (I_e^E + I_e^S) + (I_h^E + I_h^S)$.

At very small V_{ds}, the thermoelectric current can significantly contribute to the total current, which is the result of the laser induced high temperature at the heterojunction. This forces the electrons and holes to diffuse away from the junction. For the electrons, the conduction band built-in barrier offset is very small and hence, any net thermoelectric electron current can arise only from the small difference in Seebeck coefficient between the monolayer and the bilayer MoS_2 (Wickramaratne et al. 2014 Hippalgaonkar et al. 2015 Yoshida et al. 2016). This would result in negligible I_e^S in all the bias configurations. However, the built-in potential step is large for the holes. Because of this, the holes are blocked to move to the monolayer side of the junction. This forced asymmetric flow of the holes would result in an appreciableI_h^S, which is stronger than I_e^S, and controls the photocurrent profile to a certain extent. We should note the difference between the above mentioned effect and conventional photothermoelectric effect observed that in barrier free junctions like Graphene heterojunction. In the case of Graphene, the built-in potential barrier is negligible. So the thermoelectric current results only from the difference in Seebeck coefficients for a monolayer and a bilayer Graphene. It is worth noting that in this configuration, the direction of I_h^S is same as that with the photoelectric effect induced current.

At higher positive V_{ds}, on the other hand, there is a strong bias dependence of the photocurrent at the 1L/2L junction. This indicates that the photoelectric current ($I_e^E + I_h^E$) dominates over the thermoelectric component. due to improved mobility in bilayer (Yang et al. 2014b) than monolayer, and improved coupling with contact, it is likely that I_h^E will be stronger than I_e^E as the holes are moving through the bilayer portion (less resistance for the hole movement).

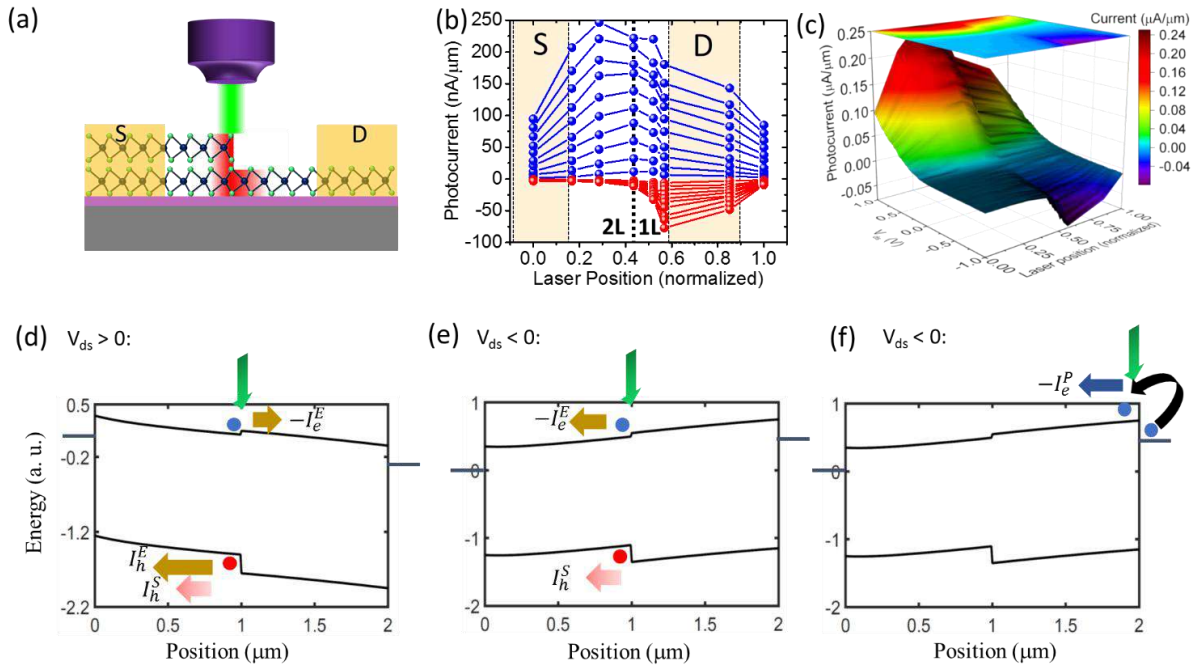

Fig 4.4 Photoresponse of monolayer/bilayer heterojunction MoS2 device MoS_2 device. (a) Schematic diagram of the device, with L = 2.0 μm and W = 1.9 μm. The laser power used is 2.6 μW. (b) spatially resolved photocurrent with positive (blue) and negative (red) V_{ds}. V_{ds} values are -1.0 V to 1.0 V in steps of 0.1 V. The dotted vertical line represents the monolayer/bilayer heterojunction. (c) 3D plot of photocurrent as a function of laser position and V_{ds}. The color plot projection is shown at the top. (d)-(e) Band diagram at (d) positive and (e) negative V_{ds}, with the laser spot at the heterojunction. The different components of the electron and hole currents (see text) are shown by arrows. (f) Band diagram at negative V_{ds} when the laser is at the drain end.

The magnitude of I_e^E can be estimated from the photocurrent values for $V_{ds} < 0$. It is easy to see [Fig. 4.4(e)] that the holes are blocked by the 1L/2L valance band offset, resulting in $I_h^E \approx 0$. Note that, in this situation, direction of I_h^S is opposite to that of I_e^E. This nullifies the net current partially, particularly at small negative V_{ds}. If we neglect contribution of any thermoelectric current at large negative V_{ds}, the total photocurrent measured in this situation can be approximately attributed to I_e^E. Note that, for $V_{ds} < 0$, the electrons flow through the bilayer portion and hence $I_e^E(V_{ds} < 0)$ is the upper limit of $I_e^E(V_{ds} > 0)$ and, from Fig. 4.4(e), is an order of magnitude lower than $(I_e^E + I_h^E)|_{V_{ds}>0}$. This shows that in the case of large positive V_{ds}, more than 90% of the photocurrent is contributed byI_h^E. In summary, for large positive (negative)V_{ds}, the primary factor of photocurrent are $I_h^E(I_e^E)$, with$|I_h^E(V_{ds} > 0)| \gg |I_e^E(V_{ds} < 0)|$. We attribute this to better separation of holes from the monolayer owing to larger valence band offset at the 1L/2L heterojunction.

For$V_{ds} < 0$, the peak photocurrent is observed when the laser is at the drain junction [red curves in Fig. 4.4(d)], where I_e^P dominates. This observation is in agreement with the Type-I band alignment of the heterojunction. Such a band alignment does not block the photo-electrons generated at the drain side from moving to the source contact, as explained in Fig. 4.4(f).

4.3.3 Photoresponse of monolayer/few-layer/multi-layer double heterojunction device (1L/FL/ML)

With the observation of photocurrent distribution in monolayer/bilayer device, we modified the design of the heterojunction to a more complex level. To increase the effect of the heterojunction, we next consider a 1L/FL/ML MoS_2 double heterojunction device. The SEM of such a double heterojunction device is shown in Fig. 4.3(c). We note the changes in the number of layers as characterized by the separation of A_{1g} and E^1_{2g} Raman peaks shown in Fig. 4.3(d). Such a double heterojunction device, as schematically shown in Fig. 4.5(a), has two advantages. First, it efficiently creates electron-hole pairs at the 1L/FL junction when excited by a laser. This is because the few layer structures are, in general, optically more active than thick multi-layer MoS_2. Second, the multi-layer portion provides efficient coupling with the contact metal (hence better contact resistance), as well as helps to reduce trapping effect, as discussed later. Compared with 1L/2L junction, the 1L/FL junction provides improved spatial separation of electrons and holes due to (i) even stronger built-in barrier offset than the previous case of monolayer/bilayer (few layer has a bandgap of ~1.3 eV), and (ii) even weaker excitonic binding energy (nearly an order of magnitude smaller than monolayer) in the few layer portion. There is a different mechanism by which such a 1L/FL junction can provide additional conduction carriers. When the laser is at the 1L/FL junction, an exciton in the monolayer can thermally diffuse into the few-layer portion. As the exciton binding energy in the few-layer MoS_2 is small, there is a high chance that the diffused exciton will break as it enters the few layer portion. This gives rise to excess carriers for conduction. Fig. 4.5(b) shows spatially resolved scanning photocurrent with a strong and sharp peak at the 1L/FL heterojunction. Interestingly, the peak occurs at negative V_{ds} condition, unlike the 1L/2L junction, where the peak occurs in the positive bias.

To understand further the peak current happening at opposite polarity compared with the 1L/2L case, we plot the band diagrams in Fig. 4.5(c)-(d). The MoS_2 layers in our devices are slightly n-type doped, even without any gating (the energy band diagram shows that the

Fermi level of MoS_2 is much closer to the conduction band). The diffusion length (L_h^D) of holes in MoS_2 is expected to be ~0.5 μm (Wang et al. 2012b). This is much smaller than the combined length (~1.8 μm) of the few-layer and multi-layer portion of the present device [Fig. 4.5(c)]. Hence, the photo-generated holes at the 1L/FL junction, when trying to reach the source contact under positive V_{ds}, undergo strong recombination in the channel. This causes in significant reduction in the total hole current ($I_h^E + I_h^S$) at $V_{ds} > 0$. We should note that due to much shorter device length, such recombination does not significantly suppress the hole current in the 1L/2L heterojunction device discussed earlier. The hole current being very small, the total current in the 1L/FL/ML device is thus governed by the electron current flow for positive V_{ds}. Now, for the case $V_{ds} > 0$, the electrons encounter a small uphill barrier due to built-in potential in the 1L/FL/ML device. Those electrons which are overcoming this barrier, will have to travel through the monolayer portion (which is having low mobility) of the device, to reach the drain contact. This results in reduced electron current. On the other hand, when $V_{ds} < 0$, the electron current again dominates the total current due to suppression of the hole current resulting from larger valence band barrier at the 1L/FL junction. Nonetheless, the electron current is strong in this case, since the photo-generated electrons at the 1L/FL junction do not face any barrier. These electrons are transported through the multi-layer portion (with relatively higher mobility). In the case when the laser is at the 1L/FL junction, we observe stronger net photocurrent when $V_{ds} < 0$, compared with $V_{ds} > 0$.

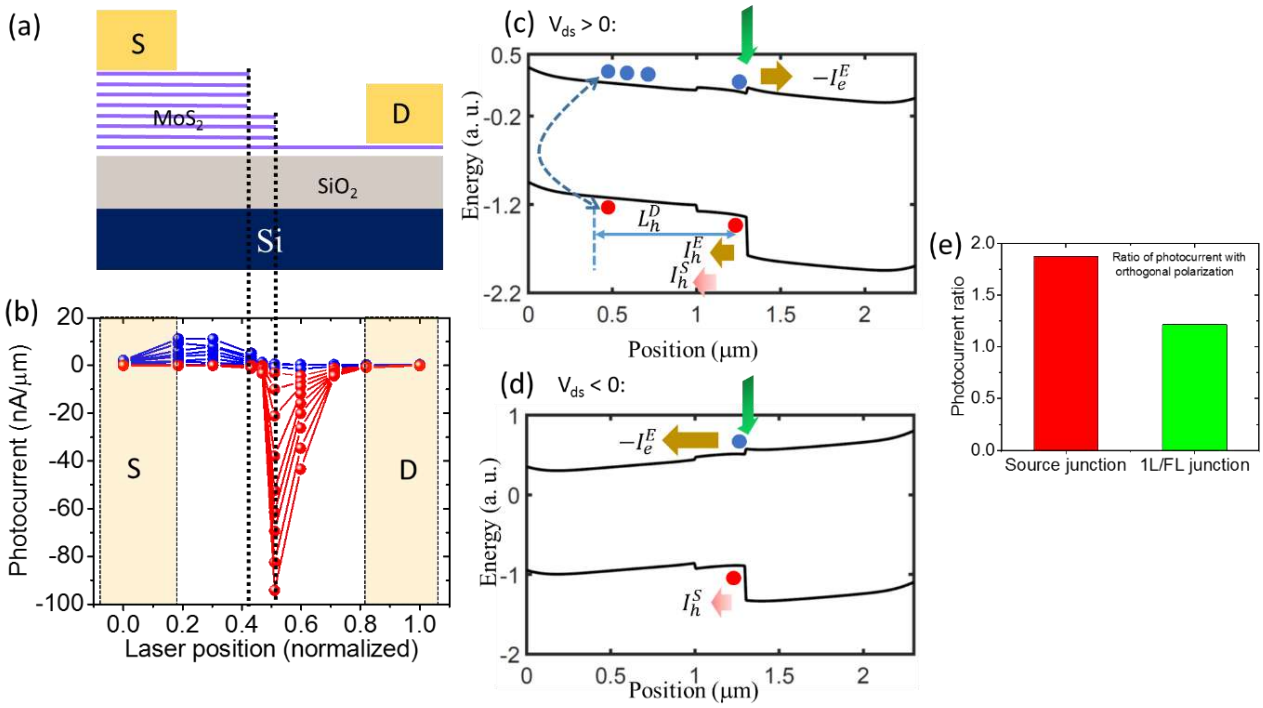

Figure 4.5 Photoresponse of monolayer/few-layer/multi-layer MoS2 double heterojunction device (a) Schematic diagram of the device, with L = 3.7 μm and W = 1.57 μm. The laser power used is 2.6 μW. (b) Spatially resolved photocurrent with positive (blue) and negative (red) V_{ds}. V_{ds} values are -2.0 V to 1.8 V in steps of 0.2 V. (c)-(d) Band diagram at (c) positive and (d) negative V_{ds}, with the laser spot at the monolayer/few-layer junction. The different components of the electron and hole currents (see text) are shown by arrows. (e) Ratio of photocurrent when the excitation laser is polarized perpendicular and parallel to the channel length, with the position of the laser spot being at the source edge (red bar) and at the monolayer/few-layer junction (green bar).

For $V_{ds} > 0$, and when the laser spot is close to the source metal-MoS_2 junction, we observe a strong photocurrent, as in earlier devices. This reinforces the fact that hot photoelectrons can be efficiently injected from the source metal, resulting in strong I_e^P and this turned out to be the primary mechanism for large photoresponse at metal/MoS_2 junction in these devices. To see the effect of plasmonics effects in this context (which is another phenomena which generates photocurrent), photocurrent measurements are done with the change in the polarization of the incident linear polarized light. Interestingly, we have observed that at this position of the laser, the photocurrent is strongly dependent on the orientation of the linear polarized excitation, as shown in Fig. 4.5(e). The peak is observed when the polarization is parallel to the source metal edge, i.e. perpendicular to the channel direction. However, there was no such strong polarization dependence of the photocurrent observed when the laser spot is at the 1L/FL junction. Such polarization dependence indicates possible

energy transfer to electrons in the metal through plasmons is also happening. Similar polarization dependence at metal/multi-layer junction has been observed recently in Hong et al. as well (Hong et al. 2015).

4.3.4 Fast transient response in heterojunction photodetector

Monolayer MoS_2 photodetectors are generally exhibiting slow transient response, varying from few seconds to minutes, in the case of planar devices(The transient characteristics of a typical monolayer MoS_2 photodetector are studied in response to the excitation laser being turned on and off either manually or by using a chopper). This is a practical limitation of these photodetectors for high speed applications. The origin of the observed long rise and fall times of these devices has been attributed to the proximity of the traps in the SiO_2 layer underneath monolayer MoS_2 (Roy et al. 2013b). Consequently, increasing the number of layers helps to improve the transient response due to screening of the traps by the low lying layers.

Long persistent photocurrent is generally observed in these 2D photodetectors, even after the laser is switched off. The role of the traps in SiO_2 in these can be understood as follows. These traps (produced by light or by photocurrent) try to reduce the metal-MoS_2 barrier, by acting as indirect gating towards the source barrier. Hence the source barrier reduces. As a result, there will be a more efficient carrier injection from the metal to the semiconductor (MoS_2). These trap dynamics, in this way, keep changing the barrier height. Since the traps decay slowly, this will reflect in the rise and fall time of these planar devices. It can be clearly understood from this dynamics, that why the speed of the devices are not compromised in vertical devices. Thus any active trap underneath the source junction is likely to impact the speed of the device more severely. In Fig. 6(a), we show the forward and reverse sweep of I-V characteristics with a slow scan in a typical heterojunction MoS_2 device, in presence of laser excitation. The photocurrent is found to enhance in the reverse sweep. All our measured heterojunction devices exhibit similar characteristics.

Such an enhancement in the current during the reverse sweep indicates hole trapping in the oxide near the source junction – forcing the effective barrier height reduction for electrons at the source junction. This mechanism is schematically drawn in the inset of Fig. 4.6(a), along with the resulting band diagram. While calculating the band diagram, we assumed uniform trapped hole density of 10^{17} cm^{-3} up to a distance of 50 nm from the source junction.

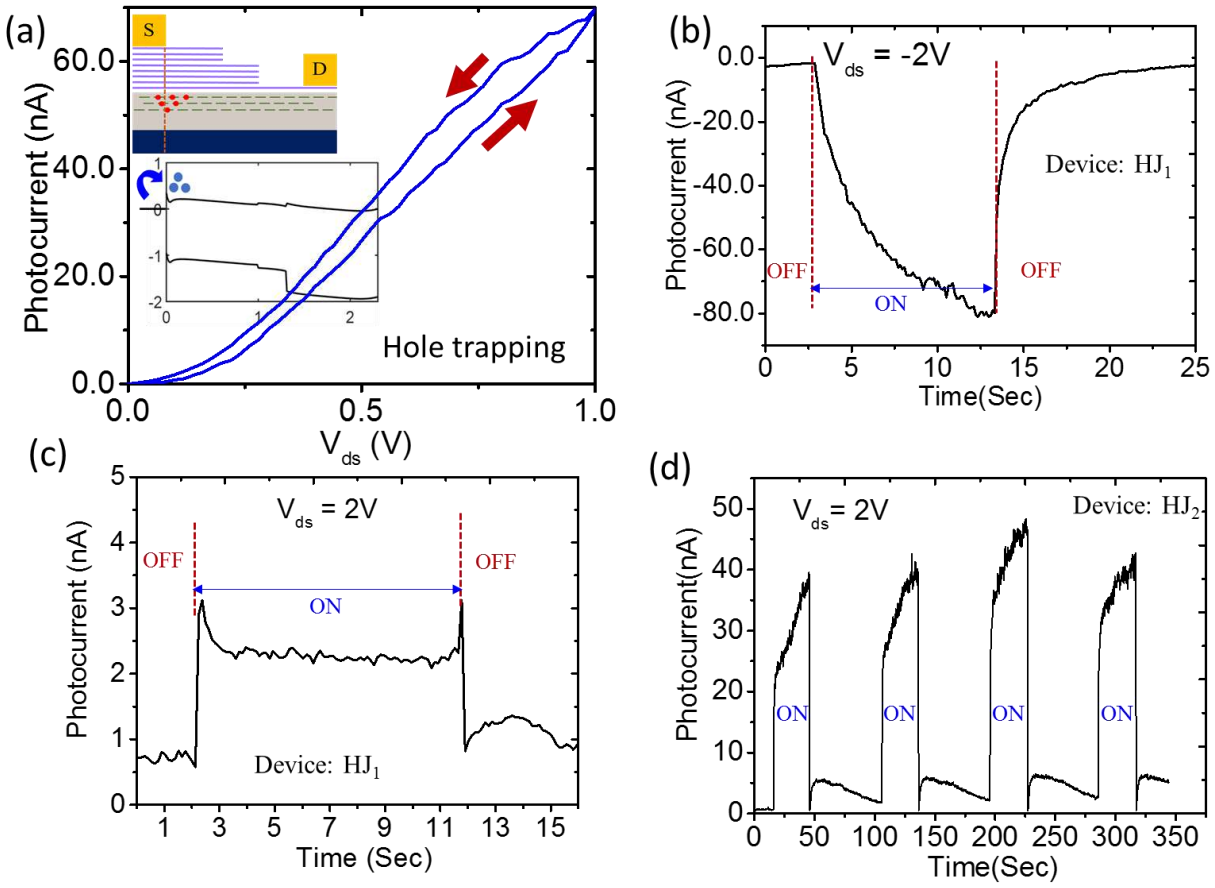

Figure 4. 6 Transient response of monolayer/few-layer/multi-layer device photocurrent with the laser illumination at the 1L/FL junction. (a) Forward and reverse I_{ds}-V_{ds} sweeps indicate a larger current in reverse sweep direction, indicating hole trapping. Inset, schematic representation of hole trapping in the oxide underneath the source junction, and the calculated band diagram showing source barrier height reduction for efficient electron injection. (b)-(c) Transient response of photocurrent of the device in Fig. 4, when the laser at the 1L/FL junction is turned on, and turned off, with (b) negative and (c) positive V_{ds}. Positive V_{ds} case exhibits excellent photoresponse times. (d) Transient response of another device (HJ_2) with a sequence of laser on and off at the 1L/FL junction, with positive V_{ds}.

From the above discussion, we expect that a thicker layer towards the source junction would be more effective to reduce the trap induced source barrier height reduction effects as thicker layers will be more shielded from the substrate traps. We can see that the double heterojunction device serves this purpose efficiently, and is found to exhibit excellent transient response when the laser spot is at the 1L/FL junction. Fig. 4.6 (b) and (c) display the transient response of the device resulting from laser being turned on and off, at V_{ds} = -2 V,

and V_{ds} =2 V, respectively. The results from another double heterojunction device with V_{ds} = 2 V are shown in Fig. 4.6(d).

In Fig. 4.7(a), the laser position dependent fall time of the photocurrent is plotted. It shows an exponential increase of fall time as the laser spot is moved towards the source junction. Here we define the fall time as the time required for the photocurrent to reduce from 90% to 10% of its steady state value. In particular, the measured fall time is ~26 ms when the laser is at the 1L/FL junction. The possible mechanisms are explained schematically in Fig. 4.7(b)-(c). The layers are extrinsically n-doped as we have discussed earlier. When the laser spot is at the 1L/FL junction, the diffusion length (L_h^D) of the photo-generated holes is much smaller than the separation (L) between the 1L/FL junction and the source metal junction.

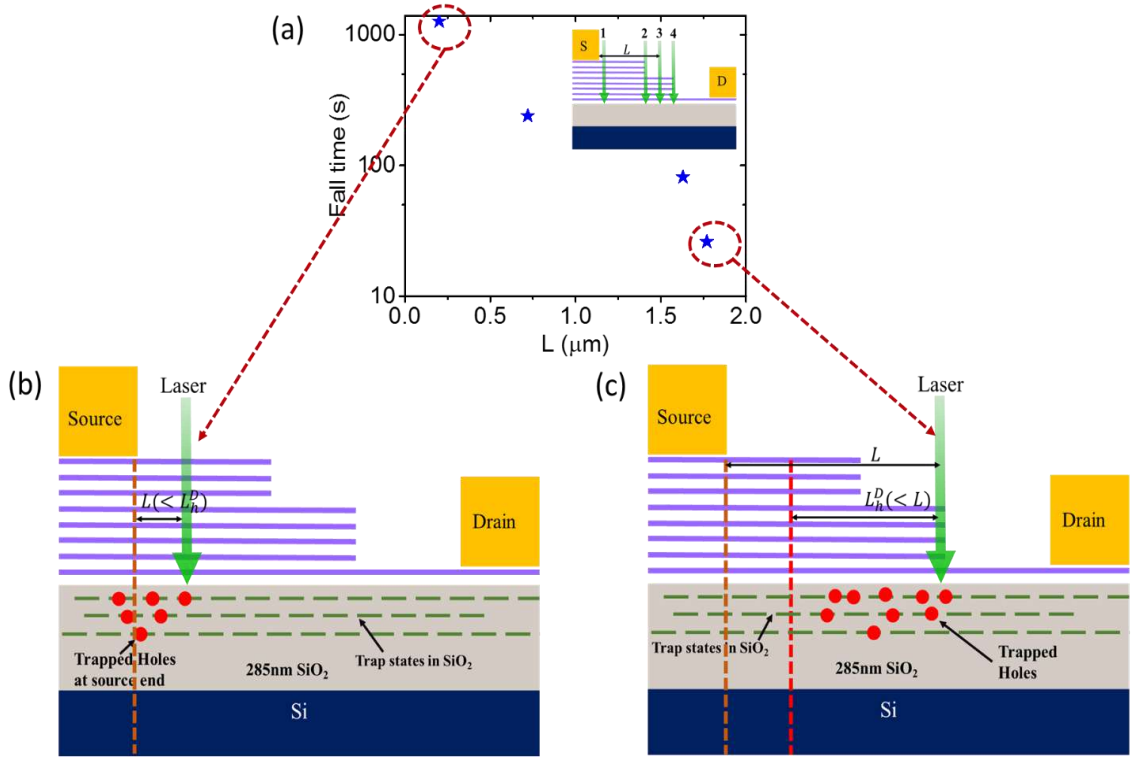

Figure 4.7 Mechanism of fast transient response in MoS_2 heterojunction photodetector. (a) Fall time (defined as the time required for the photocurrent to reduce from 90% to 10% of its steady state value) after the laser is turned off, plotted as a function of the laser spot distance from the source junction. V_{ds} has been kept at 2.0 V. Inset, the laser excitation positions are shown schematically. (b) Schematic representation of the trapping scenario, when the separation (L) between the laser spot and the source junction is less than the hole diffusion length. Holes are trapped at the source junction, resulting in source barrier reduction for electrons, and hence long persistent photocurrent (larger fall time). (c) Schematic representation of the scenario when L is larger

than hole diffusion length, in which case, reduced number of holes are trapped at the source junction, improving fall time.

Hence, the holes tend to recombine with the electrons before they reach the source junction. This suppresses the probability of hole trapping at the source junction. This will give rise to fast photo-response of these device. However, when the laser spot is moved closer to the source metal, a larger fraction of the photo-generated holes is able to reach the source junction as it does not get enough time to recombine with electrons. This, in turn, enhances the likelihood of hole trapping underneath the source junction, and thus, degrading the device photo-response.

4.4 Conclusions

In conclusion, we have investigated the electrical response to scanning photo-excitation in monolayer, bilayer, monolayer/bilayer, and monolayer/few-layer/multi-layer MoS_2 devices to understand the fundamental mechanisms of photocurrent generation in these devices. In uniform monolayer and bilayer devices hot electron injection from metal results in a strong photoresponse with the laser spot on the source junction. Photoelectric effect in these devices is found to be small in these materials due to its strong exciton binding energy. This is clear from the observation of very low photocurrent when the laser falls at the center of the channel (and in this situation, photoelectric effect is supposed to be maximum). In the case of heterostructure devices, strong photoresponse is observed when the laser is focused right at the heterojunction. This is due to the spatial separation of the photo-generated electrons and holes as a result of potential barrier induced asymmetric driving of charge carriers. The double heterojunction devices are found to provide much better photoresponse by avoiding hole trapping at the source junction when the laser spot separation from the source is longer than the hole diffusion length. Though MoS_2 used for the device fabrication in all these experiments, the observations are expected to be valid for other TMDs also. The insights obtained will be useful in designing fast optoelectronic devices based on two dimensional transition metal Dichalcogenides.

Chapter 5

Nature of carrier injection from Metal –TMDs interface

Overview:-

This chapter discusses the mechanisms of charge transfer from metal to TMDs. Conventional picture of band bending is re-visited in the context of very thin films of semiconductor. The charge transfer between the metal and semiconductor is analyzed using Raman spectroscopy, KPFM and XPS. The Schottky barrier height is measured using TLM measurements with both Au and Ni contacts. From these experiments, the contact resistance of these devices is calculated. These studies are extrapolated to calculate the limit of the contact resistance in such a system.

5. Nature of carrier injection from Metal –TMDs interface

Monolayer and few-layers of TMD materials have been shown to be very promising for light generation(Mak et al. 2010 Wang et al. 2012a Baugher et al. 2014b Pospischil et al. 2014)and detection (Lopez-Sanchez et al. 2013 Yu et al. 2013) applications as seen in the previous sections. On the other hand, the ability to suppress surface roughness scattering at sub-nm thickness, coupled with appreciable bandgap, makes them promising candidates for making logic transistors smaller than 10 nm(Majumdar et al. 2014). However, the performance of most of these electronic and optoelectronic devices are poor due to relatively large parasitic contact resistance(Léonard and Talin 2011 Radisavljevic et al. 2011 Allain et al. 2015 Xu et al. 2016). On the contrary, for photo detection applications, metal/TMDs interface plays active role in enhancing photoresponse(Buscema et al. 2013a Kallatt et al. 2016). Thus, it is important to understand the physics of the interface between metal and the TMDs in these devices. Despite its importance, studies to understand the origin of intrinsic mechanisms that control the characteristics of such interface have been very limited. Generally, the metal-TMDs interface has been analyzed in a manner similar to metal-bulk semiconductor junction and, hence, the understanding is rather poor.

Investigations on Schottky barrier height and the contact resistance of metal/TMD interface have been reported in the past (Chen et al. 2013 Das et al. 2013b Fang et al. 2013 Dankert et al. 2014 Leong et al. 2014 English et al. 2016).However, the findings of these works differ considerably from each other, particularly for the case of monolayer TMD – metal interface. In this chapter, we present detailed experimental measurements and parameter estimation to reveal the underlying mechanisms that control the Schottky Barrier formation

and the resulting contact resistance of metal-TMD interface. On the basis of material characterization, we proposed a new two-barrier carrier injection model. These barriers control the charge transfer between contact metal and 2D material just underneath the metal. The magnitude of the effective potential barrier and contact resistance was obtained by using a novel TLM based estimation methodology. For the estimation of effective barrier height, the Richardson equation was appropriately modified incorporating suggestions from the existing literature. In this any ambiguity resulting from temperature variation of channel resistance of the TMD was eliminated. Finally, the Landauer limit of the contact resistance achievable in such structures is derived analytically and compared with the experimental results. All the experiments were carried out on devices using either Au or Ni for metal contact on monolayer MoS_2films. The conclusions are general enough and are applicable to devices made using any 2D semiconductor material.

5.1 Tunneling versus thermionic emission

It is well known that TMDs have naturally passivated surface. This property of 2D materials enables its integration with any substrate quite easy since one need not bother about lattice matching. However, when it comes to making electrical contacts on TMD films, passivated surface poses some problems. It is natural to treat metal-TMD contact similar to metal-bulk semiconductor junction, wherein the band bending model is adopted. In metal-TMD contact the potential barrier formation is more complex due to the fact that the volume of the semiconductor available is insufficient for causing band bending. Such contacts have been treated in literature in terms of conventional band bending scheme together with a certain amount of Fermi level pinning and tunneling induced field emission as shown in Fig 5.1. We need to consider the presence of a thin air gap (t_{air}) between metal and the TMD layer which is naturally passivated. However, this reduces the tunneling probability for carriers. As shown in Fig5.2, the tunneling probability of lower energy electrons in the metal side of the interface are even lower. This is because of the large tunneling distance seen by these electrons to reach the TMD channel for further transport. Although at higher energy levels, tunneling distance reduces as shown in Fig 5.2,but the number of hot electrons is much less. If we consider *d* as the vertical air gap between metal edge and a point in 2D film and *t (E)* as the distance of the conduction band edge at energy *E* from the metal edge, we can quickly estimate the distance ($t_{air}(E)$) through which an electron should tunnel through, in order to reach a particular point in 2D material as $t_{air}(E)=(d^2+t^2(E))^{1/2} \approx t(E)$ for $t(E)>>d$.

The depletion width will be very large for these monolayers. This will be suppressing the field emission. So the electrons are forced to move directly downward, followed by a horizontal transport, as against the direct tunneling to the channel.

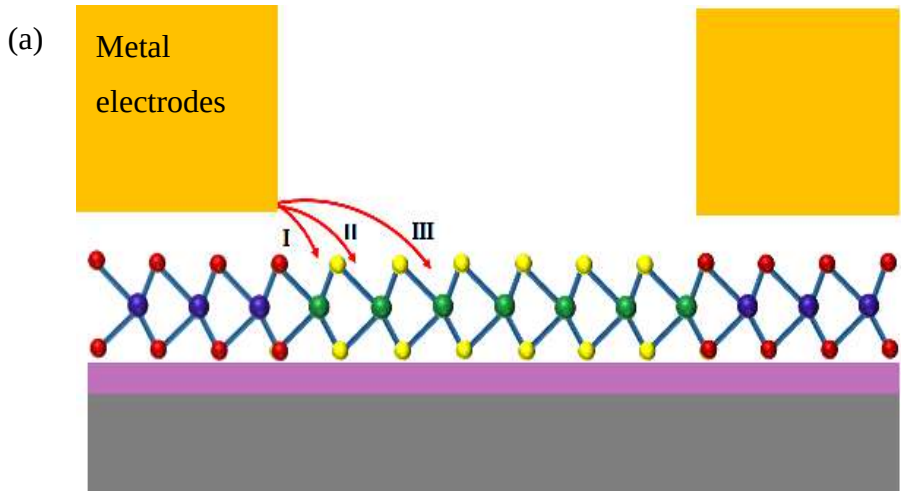

Fig 5.1 Schematic diagram showing possible carrier injection processes from metal to monolayer MoS_2.

In Fig 5.2, the tunneling process of the electrons from metal side to TMD channel is schematically shown. A thin air gap produces a potential barrier between metal-TMD interfaces. The electrons have to tunnel through this potential barrier first and then through the band bending. The length of the blue arrow in Fig 5.2 is proportional to the probability of tunneling of electrons from metal to TMD.

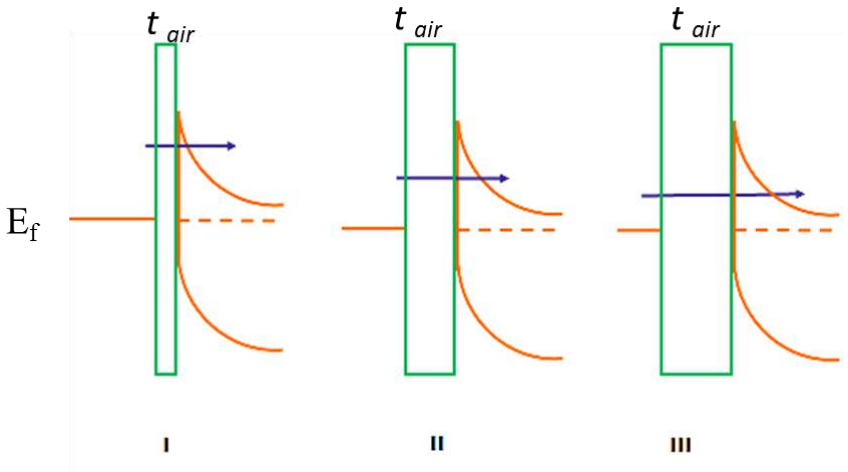

Fig 5.2 Conventional picture of band bending in a metal – semiconductor junction. Three different situations are shown to explain how the probability of electron tunneling changes with varying thickness of air gap $t_{air.}$ Length of the blue arrow in all the images is proportional to the probability of tunnelling of electron from metal to semiconductor side through the air gap. (I-III) Three different thickness of the air barrier for tunnelling.

5.2 Charge transfer between metal and MoS_2

At the metal-TMD contact transfer of charge carriers from metal to TMD is facilitated by the alignment of the Fermi levels of both materials. The contact potential barrier determines the amount of charge flow across the barrier. In order to get a clear picture, we fabricated two different devices, one with Au as the metal electrode and the other with Ni, deposited on monolayer MoS_2, to study the efficiency of charge transfer. It has been shown that in monolayer MoS_2 ,electrons occupying conduction band minimum are contributed by Molybdenum atoms (Splendiani et al. 2010). In order to get better contact resistance, hence, it is mandatory to have a sufficient electronic overlap between contact metal orbitals and that of Molybdenum. Nickel has a better affinity to make bonds with Sulphur. So when MoS_2 is in contact with Nickel, the partially filled 3*d* orbitals of Nickel will be more delocalized than that of Gold, which has a completely filled 5d-orbitals.

5.2.1 Characterization of MoS_2 monolayer on metal

To investigate the charge transfer from metal to MoS_2, we employed Photoluminescence spectroscopy, Raman spectroscopy, X-ray Photoemission Spectroscopy (XPS) and Kelvin Probe Force Microscopy (KPFM).

For these characterizations, we deposited parallel lines of Nickel on a SiO_2/Si substrate and similarly with gold on a separate substrate. Lines of metals on the substrate enable us to estimate the thickness of MoS_2 by the optical contrast measurement of the same on the extended portion of the oxide substrate.MoS_2 monolayers are exfoliated on top of these metal lines.

Raman shift of the A_{1g} peak for MoS_2 deposited on metal shows a larger broadening compared to that deposited on SiO_2. The E^1_{2g} peak did not show any such substrate dependence. This situation is depicted in Fig 5.3 (a-b). Such a broadening can be attributed to anharmonicity due to laser induced heating and doping(Chakraborty et al. 2012). However, larger broadening for monolayer samples on metals, as against SiO_2 substrate, cannot be attributed to heating of the metal itself since the heat energy spreads over the entire metal film resulting in a lower temperature rise. This suggests that the additional broadening occurs due to metal induced doping effect. Also, the photoluminescence intensity of A exciton peak is found to be dramatically suppressed for monolayer TMDs on metals as shown in Fig 5.3 (c). This suggests that there is a substantial amount of charge transfer between metal and MoS_2.

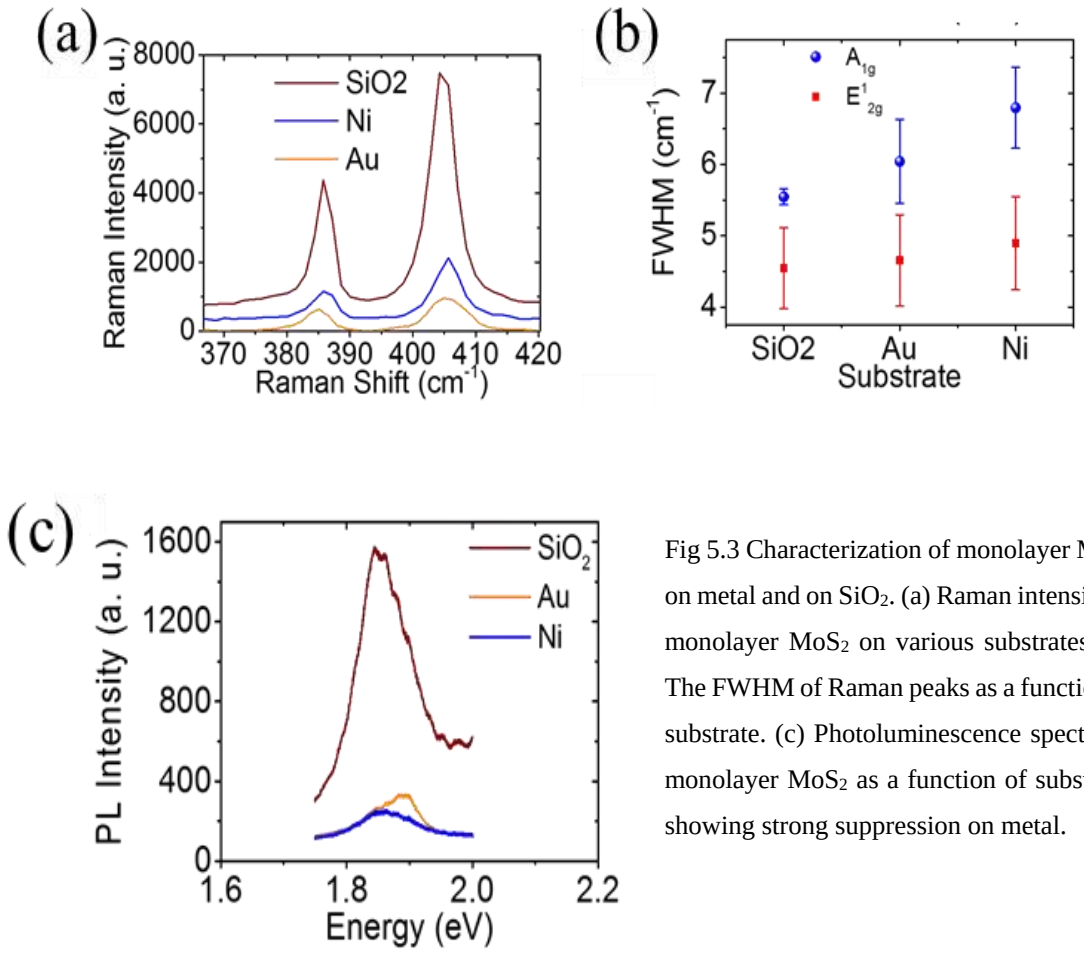

Fig 5.3 Characterization of monolayer MoS_2 on metal and on SiO_2. (a) Raman intensity of monolayer MoS_2 on various substrates. (b) The FWHM of Raman peaks as a function of substrate. (c) Photoluminescence spectra of monolayer MoS_2 as a function of substrate, showing strong suppression on metal.

On the basis of the above observations, we propose a new model to explain origin of the potential barrier between metal-TMD interfaces. The air gap between the metal surface and the TMD layer corresponds to a potential barrier Φ_V in the vertical direction from the metal to TMD. This barrier is modeled as the vertical diode D_V .The metal film transfers large quantity of electrons to the part of the TMD film just below the metal thereby heavily doping this part of the TMD channel. The electrons also experience a series resistance R_D while travelling through this region. A second potential barrier Φ_H is created between doped part of TMD and the part beyond the edge of the metal electrode, which remains practically undoped. This region is modeled as horizontal diode D_H. The electrons experience further resistance R_{CH} as they travel along the channel towards the second electrode. Fig.5.5 shows a schematic of the circuit model developed for our device. The charge carriers see the diodes D_V and D_H and the resistances R_D and R_{CH} as they flow from the source electrode to the drain electrode. The combination and predominance of all these circuit elementswould dictate the charge transport through the device.

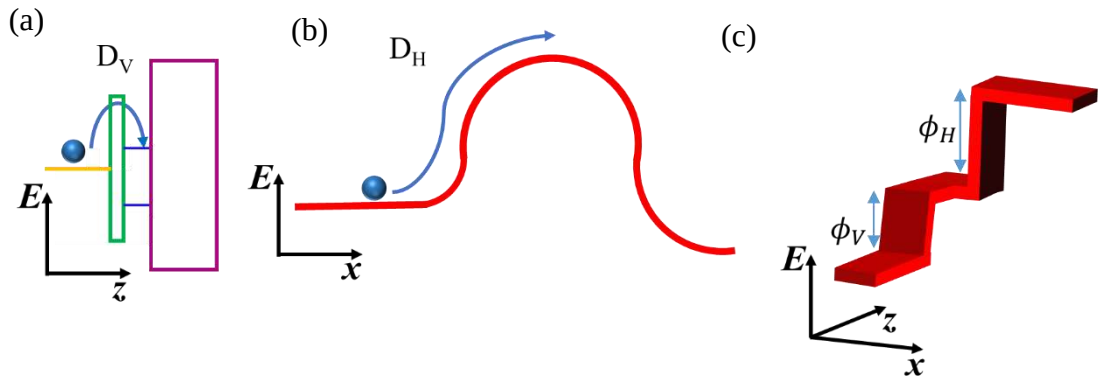

Fig 5.4 (a) the origin of the vertical diode D_V (with barrierϕ_V) between the metal and the monolayer underneath the contact, through a tunneling air gap; (b) Two possible origins of potential barrier ϕ_H in horizontal diode D_H at contact edge. Left: doping difference induced built-in barrier (weak interaction with contact). Right: Fermi level pinning induced Schottky barrier (strong interaction with contact); (c) A schematic diagram of the two barriers (ϕ_V and ϕ_H) encountered by the electron injected from the metal at the source end.

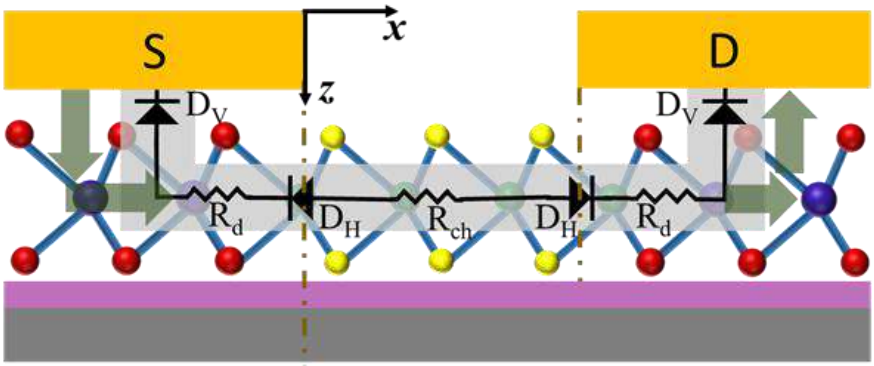

Fig 5.5 Schematic diagram of a series model of back to back diodes and resistor in a back gated device.

For further characterization, MoS_2 was exfoliated on Au and Ni coated substrates. In contrast to Raman spectroscopy and KPFM, the XPS characterization of MoS_2 monolayer on metal was not accurate as XPS beam width was much larger than the monolayer flake size. The data obtained from XPS is a mix from layers of different thickness. Fig 5.6 is the XPS data which shows that there is a blue shift of peaks of MoS_2on Au and Ni film, compared to MoS_2onSiO_2. Such a blue shift indicates that the Fermi level is relatively shifted upward, closer to the conduction band. Hence, it implies that the TMD samples on metals are doped more n-type compared with samples on SiO_2.

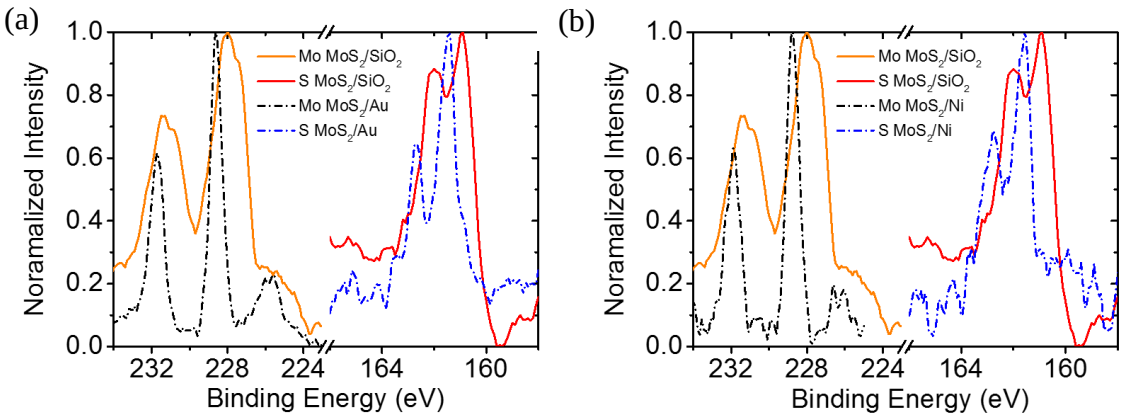

Fig 5.6 comparison of XPS spectrum of MoS_2layers between (a) Gold and $SiO_2$and (b) Nickel and SiO_2substrates.

Kelvin Probe Force Microscopy (KPFM) is used to understand the role of the potential barriers. The devices used for KPFM measurements are shown in Fig 5.7. All the metal lines are grounded for the measurement. KPFM data corresponds to the contact potential difference (CPD) between the probe tip and the sample. Thus, the Contact Potential Difference, ΔW is given by,

$$\Delta W = W_{tip} - W_{sample}.$$

For the Pt-Ir tip which we used for our KPFM measurements, W_{tip}= 5.3eV. Using the scan line 1(green line) in Fig 5.7, we first observe that W_{tip}-$W_{Au} \approx 0$, which implies that W_{Au}= 5.3eV. We also see that W_{Au}- $W_{Au/MoS2}$ = 0.12eV. From this, we can infer that $W_{Au/MoS2}$ = 5.18eV. Using scan line 2 (red line) in Fig 5.7, we obtain $W_{MoS2/SiO2}$ - $W_{Au/MoS2}$ = 0.13eV, which directly implies that the barrier height between the two regions (Φ_H) is 0.13 eV. For the Ni electrode, we obtained W_{Ni}= 5.06eV and $W_{Ni/MoS2}$ = 5.18eV and Φ_H = 20meV. Hence, we can see that the electron transfer in MoS_2 devices with Ni electrodes is higher than in devices with Gold electrode. Clearly charge transfer from metal electrode to TMD film in contact with it is not entirely dependent on the magnitude of the work function of the metal; both Nickel and Gold have large work functions. The potential barrier formation depends significantly on the electronic structure of metal too.

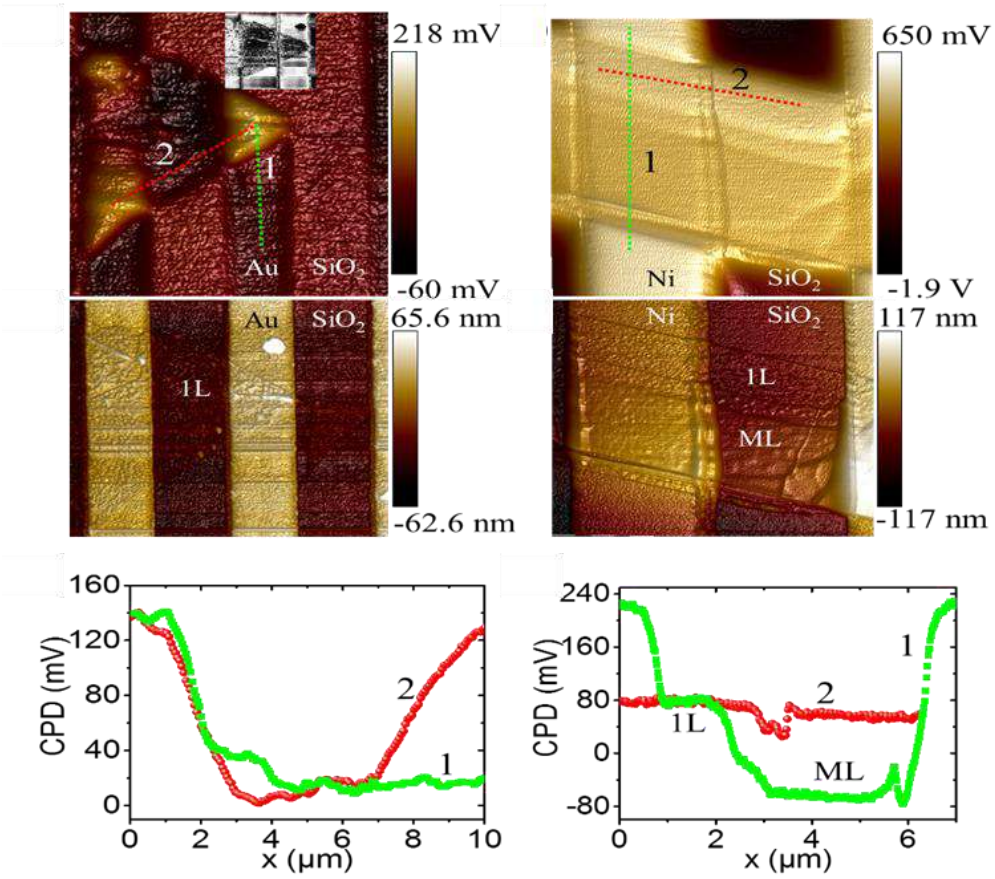

Fig 5.7 Characterization of monolayer MoS_2 by KPFM (d) CPD image of monolayer MoS_2 on Au and SiO_2 lines showing strong work function differences. Inset. A 2D AFM image of the flake. (e) Corresponding AFM image of Au lines and triangular monolayer flake. (f) Values of CPD along scan line 1 (MoS_2/Au - Au) and scan line 2 (MoS_2/Au – MoS_2/SiO_2 – MoS_2/Au). (g) CPD image of monolayer/multi-layer MoS_2 on Ni and SiO_2 lines. (h) Corresponding AFM image of Ni lines and MoS_2 flake. (i) Values of CPD along scan line 1 (Ni – 1L MoS_2/Ni – ML MoS_2/Ni – Ni) and scan line 2 (1L MoS_2/Ni – 1L MoS_2/SiO_2).

5.3 Richardson equation for barrier height measurement

In order to theoretically analyze the charge injection mechanism in our TMD devices the Richardson equation needs to be modified (Tersoff and Hamann 1983). For this purpose the MoS_2 portion underneath the metal electrode is treated as a doped ultra-thin semiconductor layer. A thin air gap is assumed to separate the metal and MoS_2 layers. As mentioned earlier the electrode-TMD junction is modeled as a series combination of diode D_V, consisting of two planes of charges separated by the air gap and D_H , a two-dimensional diode in the plane of the monolayer. Due to the difference in dimensionality, D_V and D_H obey different types of Richardson equation. Following the approach of Tersoff *et. Al.*(Tersoff and Hamann 1983), Richardson equation for the vertical diode D_V may be written as

$$J_v = A'_V e^{-2k_0 d} T^{\alpha_V} e^{-q\phi_V/k_B T} = A^*_V T^{\alpha_V} e^{-q\phi_V/k_B T}$$

with $\alpha_V = 1$ and $\phi_V = \phi_{V0} - \beta V_g - \gamma V_{ds}$. ϕ_{V0} is the barrier height without any bias, β, γ are screening dependent factors. Adopting the formalism developed by Anwar *et al*(Anwar et al. 1999), we obtain the two-dimensional form of Richardson equation for diode D_H :

$$J_H = A_H^* T^{\alpha_H} e^{-q\phi_H/k_B T}$$

with $\alpha_H = 1.5$. It must be noted that both α_V and α_H differ from conventional values of $\alpha = 2$ for three-dimensional diodes (Sze et al. 1971).

The origin of current crowding effect and resistance R_d in our devices may be understood as follows: the continuity equation for electric current requires that the loss due to the vertical current must be compensated by reduction in the horizontal current. Thus, at the ith node, we obtain the voltage $V(x)$ from the continuity equation

$$\sigma\left[\frac{V_{i-1}-V_i}{\Delta x} - \frac{V_i - V_{i+1}}{\Delta x}\right] = J_v(\mathrm{x})\Delta x$$

where σ is the in-plane conductivity of the 2D material below the metal electrode. The more precise equation is

$$\frac{d^2V(x)}{dx^2} = \frac{\zeta}{\sigma} e^{qV(x)/k_B T}$$

with $\zeta = A_V^* T^{\alpha_V} e^{-q(\phi_{V0}-\beta V_g)/k_B T}$. The solution for this equation is expressed as

$$V(x) = -\frac{2}{\beta}\ln\left[cos\left\{\frac{\beta}{2}(D_0 + \lambda x)\right\}\right]$$

where $\beta = \frac{q}{k_B T}$, $\lambda = \left(\frac{2\zeta}{\beta\sigma}\right)^{1/2}$, and $D_0 = -\frac{2}{\beta} tan^{-1}\left(\sqrt{e^{\beta V_0} - 1}\right)$.

Thus the injected electrons experience an effective barrier due to cascading effect of D_V, R_d and D_H, following an effective Richardson equation:

$$J = A_{eff}^* T^{\alpha_{eff}} e^{-q\phi_{B,eff}/k_B T}$$

where the effective barrier height $\phi_{B,eff} \leq \phi_V + \phi_H$. The equality holds only when either of ϕ_V and ϕ_H is negligible (that is, zero reflection from one of the diodes) and the transport underneath the metal is near ballistic. Also, since ϕ_V and ϕ_H vary with biasing conditions, α_{eff} varies in the range $1 \leq \alpha_{eff} \leq 1.5$ (Chen et al. 2013)

5.4 Estimation of effective barrier height

In earlier works, both $\alpha_{eff} = 2$ (Dankert et al. 2014 English et al. 2016) and $\alpha_{eff} = 1.5$ (Chen et al. 2013)have been used for barrier height calculation. Apart from the choice of α_{eff}, the Schotttky Barrier Height also depends on the fact that the channel resistance varies with temperature owing to strong dependence of carrier mobility on temperature in ultra-thin layers (Jariwala et al. 2013). Hence Richardson equation does not completely describe the temperature dependence of the current density. Thus the theoretical estimate of the barrier height is usually an under-estimate.

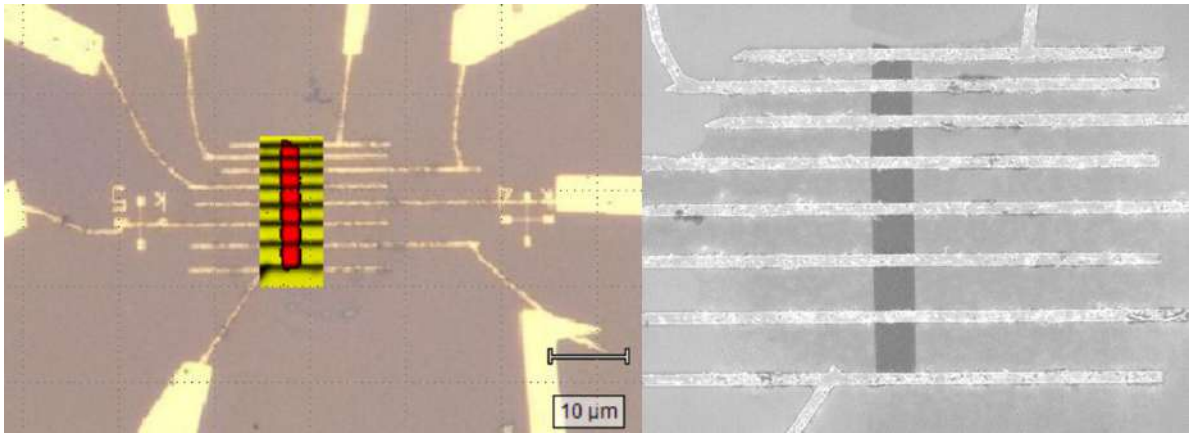

Fig 5.8 TLM devices with MoS_2 monolayers (a) Optical image and the corresponding Raman mapping of a typical TLM device. In the Raman map, red patch corresponds to the monolayer MoS_2, and the yellow signal is from Si; (b) An SEM image of the device. Black strip is the monolayer $MoS_2$and the white lines are the metal contacts of the TLM device. Width of the metal electrode is 500nm. Width of the monolayer MoS_2 strip is 1.5µm. Length of the channel portion between the electrodes were varying from 300nm to 2µm.

To nullify the temperature dependent channel resistance effect, we fabricate a set of back gated devices with varying channel length and use the Transfer Length Method (TLM) as shown in Fig 5.8. SEM micrograph along with Raman mapping of the TLM device fabricated for our measurements are shown in Fig 5.8. The I_{ds}-V_g characteristics of a typical device with Au and Ni contacts are shown in Fig 5.9(a), at different temperatures ranging from 215 K to 290 K. All devices having nickel electrodes exhibit lower threshold voltage compared to devices having gold electrodes. This suggests Fermi level pinning close to the conduction band edge at the contact MoS_2/channel MoS_2 junction. Fig 5.9(b) shows the variation of I_{ds} with V_{ds} and the graph is seen to be almost free from hysteresis. I_{ds} of 52 µA/µm was obtained in a MoS_2 device, with Au electrode, having 300nm channel length at V_g = 80 V and V_{ds} = 2 V.

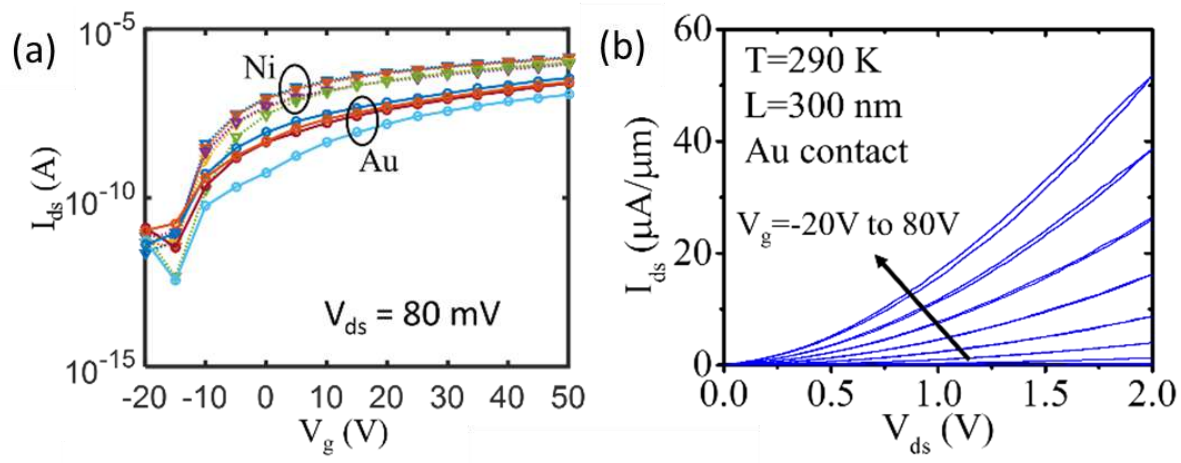

Fig 5.9 electrical characterization of the TLM device (a) I_{ds}-V_g plot of Au and Ni contacted device, at multiple temperatures. Ni devices show lower V_t; (b) Forward and reverse I_{ds}-V_{ds} sweep of a 300 nm channel length back gated monolayer transistor, showing 52 μA/μm drive current at V_{ds} = 2V and V_{ds}=80 V.

Fig 5.10 (a) shows the method of extraction of the contact resistance. The total resistance R_T of our device is the combination of R_{CT}, the electrode-TMD contact resistance, and R_{SH}, the sheet resistance of the TMD channel, is given by

$$R_T W = R_{sh} L + R_{cT} W$$

where L is the length of the TMD between electrodes W is its width. Fig. 5.10 (a) shows that the variation of R_T with L is linear. The intercept of the graph on the vertical axis yields the total contact resistance for both the source and the drain contacts. A more accurate value of the contact resistance at the source terminal R_{CS} is estimated from the equation:

$$R_{cS}(V_g, V_{ds}) = R_{cT}(V_g, V_{ds}) - 0.5 \times R_{cT}(V_{g,max}, V_{ds,max}).$$

Where *Rcs* is the source side contact resistance. Fig.5.10 (b) shows variation of current density *J* with temperature T. The plot of $\ln(I_c T^{-\alpha_{eff}})$ with $\frac{q}{k_B T}$, for $\alpha_{eff} = 1$, is a straight line which enables us to unambiguously determine $\phi_{B,eff}$, the Schottky barrier height. The calculated $\phi_{B,eff}$ values for the device with gold electrodes is plotted as a function of V_g and V_{ds} in Fig. 5.11(a) and (c). Similar data for the device with nickel electrode is plotted in Fig5.11 (b) and (d). The nickel electrode devices were always showing very low contact resistance. This is also in accordance with KPFM data where nickel showed a better charge transfer with MoS_2. At higher bias conditions, both gold and nickel showed very low barrier.

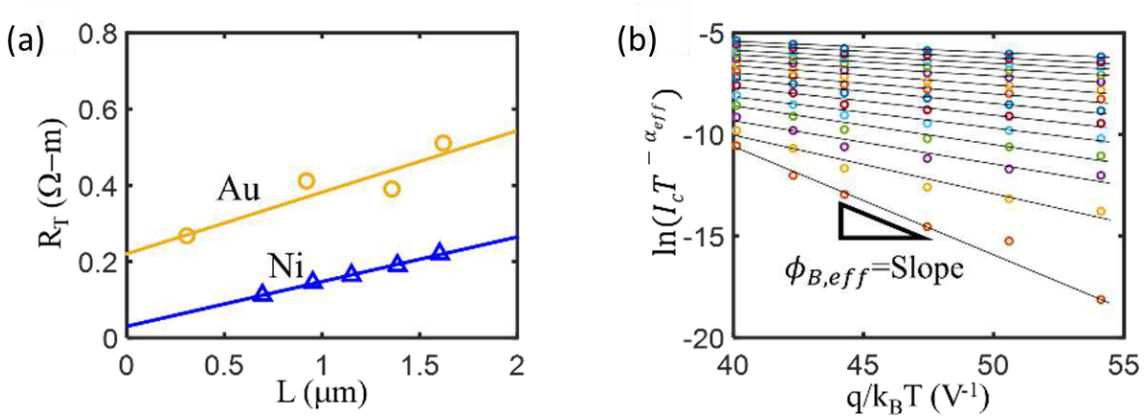

Fig 5.10 (a) A typical TLM fit for Au and Ni devices with intercept corresponding to R_{cT} (b) $I_c = V_{ds}/R_{cS}$ is used in a Richardson plot at different biasing conditions. The slopes of the linear fits correspond to the effective barrier height.

The extraction is performed with $\alpha_{eff} = 1.5$ showing a difference of ~10 meV. The Nickel electrode contacted devices [Figure 5.11 (c) and (d)] consistently show lower $\phi_{B,eff}$ compared with Au, in agreement with KPFM and XPS analysis.

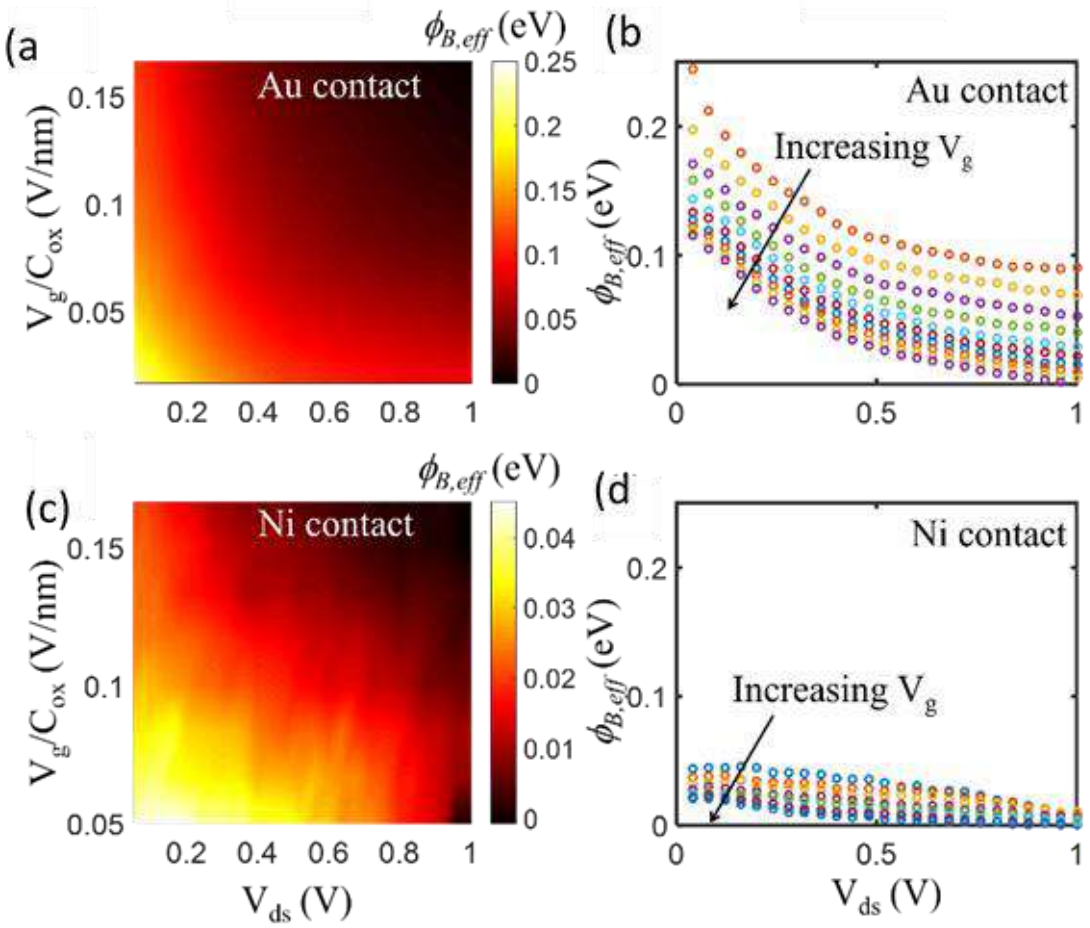

Fig 5.11 Variation of effective barrier height with bias (a) The effective barrier height for Au-MoS_2 contact, as extracted from TLM, is plotted as a function of V_{ds} and gate electric field. (b) Horizontal slices of Figure (f) at different gate electric field. (c)-(d) The effective barrier height for Ni-MoS_2 contact.

To get insights into the V_g dependence of $\phi_{B,eff}$, we solve 1-D coupled Poisson-Schrodinger (CPS) equations along the vertical direction of the device, both at the channel region and at the contact region. From the simulated potential, the barrier height is extracted in Fig 5.12(a), which will be valid for small V_{ds} due to 1D nature of the equations. Using only channel doping as a fitting parameter, we were able to obtain good agreement between the simulation (red lines) and the TLM extracted SBH including the 'knee point.' The deviation of $\phi_{B,eff}(V_g)$ from linearity in the vicinity of the knee point arises due to gate field screening at high voltage. Using estimated values of ϕ_H from KPFM and assuming$\phi_{B,eff} \approx \phi_V + \phi_H$, the individual components ϕ_V and ϕ_H are extracted at V_g=0. Further, using $\phi_V(V_g = 0)$, we calculate the doping of the monolayer MoS_2 film underneath the contact, and using the same, the ϕ_V at non-zero V_g is also simulated (blue lines). At larger gate field, ϕ_H almost collapses, and ϕ_V dominates the total barrier. With an increase

in V_{ds}, ϕ_V also is suppressed, and the device enters into *"zero thermal barrier"* regime of operation [bottom right corner of Figure 5.11(b) and (d)], where only d and R_d control the contact resistance.

Thus, for devices with Gold and Nickel electrodes, the potential barrier is nearly zero at very high bias. It is worth noting that the barrier in the case of devices with Nickel electrode is very low even at low bias voltages. Hence, this device produces "zero barrier" at much lesser gate and drain bias voltages. According to the model which we have proposed at the beginning, the disappearance of the potential barrier under high bias voltages can be explained as follows: the horizontal barrier between undoped and doped portions of MoS_2gets modified as the bias increases. Especially at high gate field, the TMD channel gets heavily doped all over the film. In this situation, the potential hill Φ_H, vanishes. Also, the high gate field dopes the area under the metal electrode to even higher levels. This modifies the series resistance of the TMD film. The series resistance R_d also gets reduced by this gate induced doping of the entire channel. Since both parameters, which determine the barrier height between metal and TMD, disappear, the barrier reduces to almost zero. Still, the contact resistance is limited by the air gap controlled vertical diode D_v. This can be reduced by the application of an appropriate metal electrode which can reduce the thin air gap between metal and TMD by effectively delocalizing its valance electrons.

5.5 Contact resistance limit

In Figure 5.12(b), R_{cT} is plotted as a function of the 2D sheet carrier density (n_s) for the devices with Au and Ni as electrode, at different temperatures. Carrier density n_s is obtained as

$$n_s = C_{ox}(V_g - V_t)/q.$$

At T=290 K, gate field = 0.167 V/nm and V_{ds} = 1 V, the contact resistance ($R_c = R_{cT}/2$) for monolayer MoS_2 device with Nickel electrode was found to be 14 kΩ-μm and that of MoS_2 device with Nickel electrode was found to be 23 kΩ-μm. Contact resistance of Nickel electrode contacted decide was reduced to 9 kΩ-μm after a vacuum anneal at 127℃ for one hour. In the case of devices with gold electrode, annealing did not produce any such improvement.

To see how these values compare with the fundamental limit of contact resistance achievable, we used the Landauer approach to calculate the conductance in a monolayer MoS_2 device with metal contact using the following equation

$$G = \left(\frac{2q^2}{h}\right) g_v M \mathrm{T}_{eff},$$

where h is Plank's constant, g_v is valley degeneracy (= 2 for monolayer MoS_2), M is number of current carrying modes per valley. $\mathrm{T}_{eff}$is the effective transmission probability through the three cascaded processes described earlier and is given by $\mathrm{T}_{eff} = \frac{1}{\frac{1}{T_V}+\frac{1}{T_d}+\frac{1}{T_H}-2}$. For maximum transmission limit, $T_{eff,max} = e^{-2k_0 d}$ is obtained at the zero thermal barrier and ballistic limit, by noting that $T_{V,max} = e^{-2k_0 d}$ (tunneling through zero thermal barrier air gap in D_V), $T_{d,max} = 1$ (ballistic limit of MoS_2 underneath metal), and $T_{H,max} = 1$ (zero thermal barrier in D_H). At low temperature limit, only electrons at Fermi level take part in conduction, and hence $k_0 = \frac{(2m^*\varphi_{avg})^{1/2}}{\hbar}$. Here we assumed$\varphi_{avg} = 0.5(W_m + \chi_{MoS_2})$. The number of modes of a two-dimensional conducting channel is given (Datta 2005)

$$M = Int\left[\sqrt{\frac{2m^* W^2 \Delta E}{\pi^2 \hbar^2}}\right] \approx W\sqrt{\frac{2n_s}{g_v \pi}}$$

where n_s is given by $n_s = g_v \frac{m^*}{\pi\hbar^2}\Delta E$ ignoring Fermi-Dirac broadening. Here $Int[.]$ is the maximum integer function. Hence,

$$R_{c,min}W = \frac{W}{G_{max}} = \left(\frac{h}{2q^2}\right) e^{2k_0 d}\sqrt{\frac{\pi}{2g_v n_s}}.$$

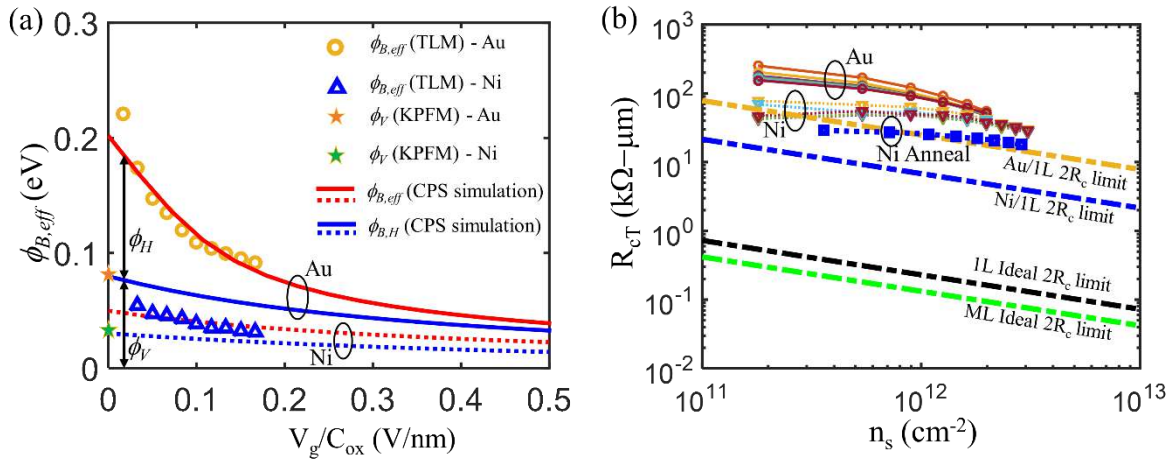

Fig 5.12 Experimental validation of thermionic model and the limits of contact resistance of MoS_2 devices; (a) Comparison of coupled Poisson-Schrodinger (CPS) solution predicted $\phi_{B,eff}$ (shown in red solid line for Au and red broken lines for Ni) and the corresponding TLM extracted value (golden circle for Au and blue triangle for Ni), at small V_{ds} using channel doping (6.3×10^9 cm^{-2} for Au and 2.24×10^{12} cm^{-2} for Ni) as fitting parameter. The star symbols indicate ϕ_V at V_g = 0, which is obtained by subtracting the KPFM extracted ϕ_H from Simulated$\phi_{B,eff}$. The blue lines (solid for Au and broken for Ni) correspond to $\phi_V$at non-zero V_g, and are obtained by fitting a doping concentration (7.0×10^{11} cm^{-2} for Au and 4.76×10^{12} cm^{-2} for Ni) underneath the contact corresponding to the star. (b) The extracted total contact resistance R_{cT} for Au and Ni at different temperatures (215 K to 290 K) are shown as a function of the 2D sheet carrier density. Annealed Ni contact is also shown at 290 K. The corresponding lower limits achievable for Au ($d = 3$Å, $W_m =$ 5.3 eV), Ni ($d = 2.2$Å, $W_m = 5.06$ eV), and an ideal contact ($d = 0$) are shown for comparison. For monolayer (1L) and multi-layer (ML), $g_v = 2$ and $g_v = 6$ are used, respectively.

In Figure 5.12 (b), the $2R_{c,min}W$ limits are plotted for Au and Ni electrode contacted devices and also for an ideal contact where $d = 0$ is assumed (no air gap). Also, the barrier height measured from KPFM measurements is also used. For comparison, ideal multi-layer limit is also shown using $g_v = 6$. The obtained limits clearly allow provision for further technological improvement. We note that, at smaller V_g, the extracted R_c decreases with an increase in temperature, due to enhanced thermionic emission efficiency. However, the trend diminishes and eventually reverses at higher bias, where the thermionic emission efficiency does not change appreciably due to negligible barrier. However, carrier scattering under the metal contact increases with an increase in temperature, in turn increasing contact resistance.

5.6 Conclusions

In conclusion, using a combination of theoretical and experimental techniques, we investigated the nature of current injection at the junction between a monolayer MoS_2 and the contacting metal (Au and Ni). We have shown that the charge transfer between contact metal and MoS_2 underneath plays a key role in such a contact, where the carrier from source is injected via two cascaded thermal barriers. The corresponding Richardson equation of such a Schottky diode requires appropriate modification in the power of T. At large gate and drain bias, both Au and Ni contacted devices offer zero effective thermal barrier contact, where the contact resistance is limited by the tunneling air gap and the conductivity of the monolayer underneath the contact. At this zero barrier condition, the fundamental lower limits of contact resistance are obtained theoretically using Landauer approach. The insights obtained will be useful in designing well-behaved contacts for high performance two-dimensional electronic and optoelectronic devices.

Chapter 6

Summary and conclusions

Overview:

Chapter 6 outlines the summary of the work presented in the thesis along with important conclusions drawn from the study. Scope for further research has also been outlined.

6. Summary and conclusions

6.1 Summary

Various optoelectronic properties of Transition Metal Dichalcogenides (TMDs), such as MoS_2, WS_2, WSe_2 and $MoSe_2$, were studied in this work. PL spectra of these materials were investigated in detail using linearly polarized laser for excitation. The PL spectra were recorded over energies ranging from the excitonic band gap to the excitation energy using both horizontal and vertical linear polarization states of the laser light. It was observed that polarization of the incident light influences the PL spectra near the excitation energy. On the contrary, PL spectra at energies close to the exciton band gap does not show any polarization resolved characteristics. The PL experiment is repeated for non-resonant and resonant excitation conditions. In the case of resonant excitation, degree of polarization up to 40% was observed for $MoSe_2$. Generation of valley coherence is important from the point of view of valleytronics, where manipulation of the valley degree of freedom by external stimulation is exploited. Hence, demonstration of such coherence at room temperature, on one hand, is technologically important due to increased hopes for room-temperature valleytronics and, on the other hand, provides greater flexibility in the choice of laser wavelength and sample temperature. From the analysis of PL spectra, the temperature of the charge carriers in the TMD films has been estimated. From the measurement of line-shift and line broadening of Raman spectrum, the different paths for relaxation of hot carriers have been identified. Such in-situ and nondestructive estimation of the temperature of charge carriers as well as the phonons separately is generally difficult for semiconductor under non-equilibrium conditions. The technique can also be easily extended to other systems such as devices subjected to high electric fields.

TMD based planar photodetectors were fabricated to study the different mechanisms that control the performance of TMD based devices. Though MoS_2 is taken as the representative TMD, the observations are valid for other TMDs as well. Electrical response to scanning photo-excitation in monolayer, bilayer, monolayer/bilayer, and monolayer/few-layer/multi-layer MoS_2 devices were studied to elucidate the fundamental mechanisms of photocurrent generation. In uniform monolayer and bilayer devices, hot electron injection from

metal to MoS_2 results in a strong photoresponse when the laser spot is on the source electrode edge on MoS_2 surface. When the laser spot is entirely on the MoS_2 material, between the two electrodes, in the device, the photocurrent generation is found to be small owing to the large exciton binding energy. In the heterostructure devices, a strong photoresponse is observed when the laser is focused right at the heterojunction, which is due to better spatial separation of the photo-generated electrons and holes, along with asymmetric potential barrier at the junction area between the layers due to Type-I band alignment. The double heterojunction devices are found to provide faster photoresponse due to reduced hole trapping effect at the source junction and the device is longer than the hole diffusion length. The insights obtained will be useful in designing fast optoelectronic devices based on two dimensional transition metal Dichalcogenides

A crucial factor dictating any device performance is the magnitude of contact resistance. We have investigated the origin of potential barrier between metal electrode and TMD film and, hence, the nature of carrier injection. We have proposed a new model for the potential barrier in metal-TMD junction. In our devices, amount of semiconductor material is so small that band bending, which is usually cited for contact resistance, is negligible. Devices were fabricated using monolayer MoS_2 and either gold or nickel for electrodes. KPFM measurements revealed the existence of a potential barrier across the electrode-MoS_2 interface which may be modeled as a diode. A separate potential barrier is created in the MoS_2 channel close to the electrode edge due to heavy doping of the portion of MoS_2 just below the metal electrode. This is also modeled as a diode. Our measurements showed that a substantial amount of charge transfer happens across these barriers. To obtain the effective barrier height, Transfer Length Measurements were done with monolayer MoS_2 devices. The electrical measurements are done at varying temperatures to estimate the contact resistance and barrier height. The corresponding Richardson equation, which is used for the measurement of the barrier height of such a Schottky diode, requires appropriate modification before applying it to devices made using 2D materials. At large gate and drain bias, both Au and Ni contacted devices offer an effective contact potential barrier which is very close to zero. This is due to the doping effect of the gate and drain bias voltages, which lowers the horizontal barrier substantially. The contact resistance is limited by the tunneling air gap and the conductivity of the monolayer underneath the electrode. The electrical and KPFM data reveals that with Ni electrode, the charge transfer to MoS_2 film is higher than the case where Au is used as electrode. For zero barrier condition, the fundamental lower

limit for contact resistance may be theoretically calculated using the Landauer approach (Datta 2005). The insights obtained will be useful in designing good quality contacts and, thereby, ensure better performance of the electronic and optoelectronic devices made with TMD materials.

6.2 Conclusions

The main outcome of our investigations may be stated as follows.

I. Linearly polarized light was used to study the hot luminescence from TMDs. Strong polarization resolved hot luminescence characteristics were seen for various TMDs. Normal Photoluminescence (PL) was found to be independent of the orientation of the plane of polarization of the laser beam.

II. Hot PL and normal PL were used to estimate the carrier temperature when the sample was irradiated by laser light. This offers a new non-destructive method for carrier temperature measurement. Raman line width broadening was used for the calculation of lattice temperature. Thus, a detailed picture of carrier excitation by linearly polarized light and carrier relaxation by different mechanisms was obtained.

III. Various processes involved in the photocurrent generation were compared. Hot electron injection from the metal electrode is seen to be a dominant mechanism for photocurrent generation in TMDs. Maximum photocurrent was generated when the laser beam was incident on the edge of the source electrode. Photoelectric effect is very weak in these materials.

IV. In planar heterojunction devices, maximum photocurrent is produced when the laser beam spot is incident on the hetero-junction zone for positive bias voltages. For reverse bias voltages the maximum current is generated when the laser beam spot moves to the source electrode edge.

V. Photodetectors made using heterostructures, instead of monolayers, showed faster photo-response. This is ascribed to the efficient screening of traps in the substrate and also to the splitting of more excitons at the junction area.

VI. The charge transfer from metal to TMDs is the major factor that controls the net photocurrent. It was seen that nickel electrodes provide better charge transfer than gold and devices with Ni electrode show much better characteristics.

VII. Schottky barrier height was measured along with transfer length measurements for devices with both nickel and gold electrodes. Richardson equation was modified for

the case of 2D materials. At higher V_g and $V_{ds,}$ the Schottky barrier practically disappears. This is more prominent in the case of devices with Ni electrodes.

6.3 Scope for future work

The investigations reported in this thesis indicate scope for further studies to exploit the various optoelectronic properties shown by TMDs. A few such studies are proposed below.

I. Real strength of 2D materials lies in the fact that they have extremely thin body. Much more work is needed to explore the possibility of charge transport in the vertical direction in the film in contrast to horizontal transport. An electron-hole pair created in the 2D material will be collected by the metal electrode within no time in the case of a vertical transport device. This could revolutionize the manner in which 2D material based photodetectors are working.

II. It is observed that the substrate on which photo detector devices are fabricated, has an influence on the device performance. Though SiO_2 is used as the preferred substrate, it has the problem of trap creation. Extended work is needed in this regard to find out the effect of other common dielectrics as Alumina, Silicon Nitride, Boron Nitride etch on the device performance.

III. It is observed that metal-TMD junction show increased photo activity. More study is needed in this direction to study the role of metal plasmonics effect in the photocurrent generation. Also, the dependence of polarization of the incident light on the photocurrent generation has to be studied.

IV. Coherent emission from K and K' valleys are observed in the case of hot PL from TMDs with linearly polarized light. This experiment can be extended with circularly polarized light, as circularly polarized light has shown to be used for optical manipulation of valleys(Jones et al. 2013).

V. Binding energy of excitons is relatively high in TMDs. To a certain extent, this deters the electrical performance to TMD based devices as excitons are electrically neutral. So for applications like photo detection, more work is needed to break the excitons in to electron and hole.

VI. More investigations are needed to understand the mechanism of barrier formation in the metal-TMDs interface. This study can help to frame a strategy reduce the contact resistance of this interface.

References

References

Akinwande, D., Petrone, N. and Hone, J. (2014). "Two-dimensional flexible nanoelectronics." *Nat. Commun.*, 5 5678.

Allain, A., Kang, J., Banerjee, K. and Kis, A. (2015). "Electrical contacts to two-dimensional semiconductors." *Nat. Mater.*, 14 (12), 1195–1205.

Anwar, A., Nabet, B., Culp, J. and Castro, F. (1999). "Effects of electron confinement on thermionic emission current in a modulation doped heterostructure." *J. Appl. Phys.*, 85 (5), 2663.

Baugher, B.W.H., Churchill, H.O.H., Yang, Y. and Jarillo-Herrero, P. (2014a). "Optoelectronic devices based on electrically tunable p-n diodes in a monolayer dichalcogenide." *Nat. Nanotechnol.*, 9 (4), 262–7.

Baugher, B.W.H., Churchill, H.O.H., Yang, Y. and Jarillo-Herrero, P. (2014b). "Optoelectronic devices based on electrically tunable p-n diodes in a monolayer dichalcogenide." *Nat. Nanotechnol.*, 9 (4), 262–7.

Bhattacharjee, S., Ganapathi, K.L., Nath, D.N. and Bhat, N. (2015). "Sulfur Treatment for Schottky Barrier Reduction in metal/MoS2 contacts: A new Proposal for Contact Engineering on TMDs." 1–10.

Bhimanapati, G.R., Lin, Z., Meunier, V., Jung, Y., Cha, J., Das, S., Xiao, D., Son, Y., Strano, M.S., Cooper, V.R., Liang, L., Louie, S.G., Ringe, E., Zhou, W., Kim, S.S., Naik, R.R., Sumpter, B.G., … Robinson, J.A. (2015). "Recent Advances in Two-Dimensional Materials beyond Graphene." *ACS Nano*, 9 (12), 11509–11539.

Britnell, L., Ribeiro, R.M., Eckmann, A., Jalil, R., Belle, B.D., Mishchenko, A., Kim, Y.-J., Gorbachev, R. V, Georgiou, T., Morozov, S. V, Grigorenko, A.N., Geim, A.K., Casiraghi, C., Castro Neto, a H. and Novoselov, K.S. (2013). "Strong light-matter interactions in heterostructures of atomically thin films." *Science (80-.).*, 340 (6138), 1311–1314.

Buscema, M., Barkelid, M., Zwiller, V., Zant, H.S.J. Van Der, Steele, G.A. and Castellanos-Gomez, A. (2013a). "Large and tunable photothermoelectric effect in single-

layer MoS 2." *Nano Lett.*, 13 (2), 358–363.

Buscema, M., Barkelid, M., Zwiller, V., Zant, H.S.J. Van Der, Steele, G. a and Steele, G. a (2013b). "Large and Tunable Photothermoelectric Eff ect in Single-Layer MoS 2." *Nano Lett.*, (13), 358–363.

Ceballos, F., Bellus, M.Z., Chiu, H. and Zhao, H. (2014). "Ultrafast Charge Separation and Indirect Exciton Formation in." *ACS Nano*, (12), 12717–12724.

Chakraborty, B., Bera, A., Muthu, D.V.S., Bhowmick, S., Waghmare, U. V. and Sood, A.K. (2012). "Symmetry-dependent phonon renormalization in monolayer MoS 2 transistor." *Phys. Rev. B - Condens. Matter Mater. Phys.*, 85 (16), 161403.

Cheiwchanchamnangij, T. and Lambrecht, W.R.L. (2012). "Quasiparticle band structure calculation of monolayer, bilayer, and bulk MoS2." *Phys. Rev. B - Condens. Matter Mater. Phys.*, 85 (20), 205302.

Chen, J.R., Odenthal, P.M., Swartz, A.G., Floyd, G.C., Wen, H., Luo, K.Y. and Kawakami, R.K. (2013). "Control of Schottky barriers in single layer MoS2 transistors with ferromagnetic contacts." *Nano Lett.*, 13 (7), 3106–3110.

Chen, Z. (2016). "Novel two dimensional material devices : from fabrication to photo-detection ices : from Fabrication to Photo-detection.".

Chernikov, A., Berkelbach, T.C., Hill, H.M., Rigosi, A., Li, Y., Aslan, O.B., Reichman, D.R., Hybertsen, M.S. and Heinz, T.F. (2014). "Exciton binding energy and nonhydrogenic Rydberg series in monolayer WS2." *Phys. Rev. Lett.*, 113 (7), 76802.

Choi, W., Cho, M.Y., Konar, A., Lee, J.H., Cha, G.B., Hong, S.C., Kim, S., Kim, J., Jena, D., Joo, J. and Kim, S. (2012). "High-detectivity multilayer MoS2 phototransistors with spectral response from ultraviolet to infrared." *Adv. Mater.*, 24 (43), 5832–5836.

Chuang, S., Battaglia, C., Azcatl, A., McDonnell, S., Kang, J.S., Yin, X., Tosun, M., Kapadia, R., Fang, H., Wallace, R.M. and Javey, A. (2014). "MoS2 P-type transistors and diodes enabled by high work function MoOx contacts." *Nano Lett.*, 14 (3), 1337–1342.

Dankert, A., Langouche, L., Kamalakar, M.V. and Dash, S.P. (2014). "High-performance molybdenum disulfide field-effect transistors with spin tunnel contacts." *ACS Nano*, 8 (1), 476–482.

Das, S., Chen, H.Y., Penumatcha, A.V. and Appenzeller, J. (2013a). "High performance multilayer MoS2 transistors with scandium contacts." *Nano Lett.*, 13 (1), 100–105.

Das, S., Chen, H.Y., Penumatcha, A.V. and Appenzeller, J. (2013b). "High performance multilayer MoS2 transistors with scandium contacts." *Nano Lett.*, 13 (1), 100–105.

Das, S., Prakash, A., Salazar, R. and Appenzeller, J. (2014). "Toward low-power electronics: Tunneling phenomena in transition metal dichalcogenides." *ACS Nano*, 8 (2), 1681–1689.

Datta, S. (2005). "Quantum Transport : Atom to Transistor.

Duan, X., Wang, C., Pan, A., Yu, R. and Duan, X. (2015). "Two-dimensional transition metal dichalcogenides as atomically thin semiconductors : opportunities and challenges." *Chem. Soc. Rev.*, 44 8859–8876.

Eda, G. and Maier, S.A. (2013). "Two-dimensional crystals: Managing light for optoelectronics." *ACS Nano*, 7 (7), 5660–5665.

English, C.D., Shine, G., Dorgan, V.E., Saraswat, K.C. and Pop, E. (2016). "Improved Contacts to MoS2 Field-Effect Transistors by Ultra-High Vacuum Metal Deposition." *Nano Lett.*, 16 (6), 3824–3830.

Fang, H., Tosun, M., Seol, G., Chang, T.C., Takei, K., Guo, J. and Javey, A. (2013). "Degenerate n-doping of few-layer transition metal dichalcogenides by potassium." *Nano Lett.*, 13 (5), 1991–1995.

Fiori, G., Bonaccorso, F., Iannaccone, G., Palacios, T., Neumaier, D., Seabaugh, A., Banerjee, S.K. and Colombo, L. (2014). "Electronics based on two-dimensional materials." *Nat. Nanotechnol.*, 9 (10), 768–779.

Furchi, M.M., Polyushkin, D.K., Pospischil, A. and Mueller, T. (2014). "Mechanisms of photoconductivity in atomically thin MoS2." *Nano Lett.*, 14 (11), 6165–6170.

Gao, J., Li, B., Tan, J., Chow, P., Lu, T.M. and Koratkar, N. (2016). "Aging of Transition Metal Dichalcogenide Monolayers." *ACS Nano*, 10 (2), 2628–2635.

Guo, Y., Han, Y., Li, J., Xiang, A., Wei, X., Gao, S. and Chen, Q. (2014). "Study on the resistance distribution at the contact between molybdenum disulfide and metals." *ACS*

Nano, 8 (8), 7771–7779.

Han, S.W., Kwon, H., Kim, S.K., Ryu, S., Yun, W.S., Kim, D.H., Hwang, J.H., Kang, J.S., Baik, J., Shin, H.J. and Hong, S.C. (2011). "Band-gap transition induced by interlayer van der Waals interaction in MoS2." *Phys. Rev. B - Condens. Matter Mater. Phys.*, 84 (4), 17–22.

He, K., Kumar, N., Zhao, L., Wang, Z., Mak, K.F., Zhao, H. and Shan, J. (2014). "Tightly bound excitons in monolayer WSe2." *Phys. Rev. Lett.*, 113 (2), 26803.

Hill, H.M., Rigosi, A.F., Roquelet, C., Chernikov, A., Berkelbach, T.C., Reichman, D.R., Hybertsen, M.S., Brus, L.E. and Heinz, T.F. (2015). "Observation of excitonic Rydberg states in monolayer MoS2 and WS2 by photoluminescence excitation spectroscopy." *Nano Lett.*, 15 (5), 2992–2997.

Hippalgaonkar, K., Wang, Y., YuHanyu, Z., Wang, Y., Moore, J. and Zhang, X. (2015). "Record High Thermoelectric Powerfactor in Single and Few-Layer MoS2." *arXiv*,.

Hong, T., Chamlagain, B., Hu, S., Weiss, S.M., Zhou, Z. and Xu, Y.Q. (2015). "plasmonic hot electron induced photocurrent response at MoS2-metal junctions." *ACS Nano*, 9 (5), 5357–5363.

Hong, X., Kim, J., Shi, S.-F., Zhang, Y., Jin, C., Sun, Y., Tongay, S., Wu, J., Zhang, Y. and Wang, F. (2014). "Ultrafast charge transfer in atomically thin MoS2/WS2 heterostructures." *Nat. Nanotechnol.*, 9 (August), 1–5.

Howell, S.L., Jariwala, D., Wu, C.C., Chen, K.S., Sangwan, V.K., Kang, J., Marks, T.J., Hersam, M.C. and Lauhon, L.J. (2015). "Investigation of Band-Offsets at Monolayer-Multilayer MoS2 Junctions by Scanning Photocurrent Microscopy." *Nano Lett.*, 15 (4), 2278–2284.

Huang, Y., Sutter, E., Shi, N.N., Zheng, J., Yang, T., Englund, D., Gao, H.J. and Sutter, P. (2015). "Reliable Exfoliation of Large-Area High-Quality Flakes of Graphene and Other Two-Dimensional Materials." *ACS Nano*, 9 (11), 10612–10620.

Jariwala, D., Sangwan, V.K., Late, D.J., Johns, J.E., Dravid, V.P., Marks, T.J., Lauhon, L.J. and Hersam, M.C. (2013). "Band-like transport in high mobility unencapsulated single-layer MoS 2 transistors." *Appl. Phys. Lett.*, 102 (17), 2–6.

Jo, S., Ubrig, N., Berger, H., Kuzmenko, A.B. and Morpurgo, A.F. (2014). "Mono- and bilayer WS2 light-emitting transistors." *Nano Lett.*, 14 (4), 2019–2025.

Jones, A.M., Yu, H., Ghimire, N.J., Wu, S., Aivazian, G., Ross, J.S., Zhao, B., Yan, J., Mandrus, D.G., Xiao, D., Yao, W. and Xu, X. (2013). "Optical generation of excitonic valley coherence in monolayer WSe2." *Nat. Nanotechnol.*, 8 (9), 634–8.

Kadantsev, E.S. and Hawrylak, P. (2012). "Electronic structure of a single MoS 2 monolayer." *Solid State Commun.*, 152 (10), 909–913.

Kallatt, S., Umesh, G., Bhat, N. and Majumdar, K. (2016). "Photoresponse of atomically thin MoS 2 layers and their planar heterojunctions." *Nanoscale*, 8 15213–15222.

Kang, Y., Najmaei, S., Liu, Z., Bao, Y., Wang, Y., Zhu, X., Halas, N.J., Nordlander, P., Ajayan, P.M., Lou, J. and Fang, Z. (2014). "Plasmonic Hot Electron Induced Structural Phase Transition in a MoS2 Monolayer." *Adv. Mater.*, 26 (37), 6467–6471.

Kim, J., Hong, X., Jin, C., Shi, S.-F., Chang, C.-Y.S., Chiu, M.-H., Li, L.-J. and Wang, F. (2014). "Ultrafast generation of pseudo-magnetic field for valley excitons in WSe2 monolayers." *Science (80-.).*, 346 (6214), 1205–1208.

Kim, M.S., Seo, C., Kim, H., Lee, J., Luong, D.H., Park, J.-H., Han, G.H. and Kim, J. (2016). "Simultaneous Hosting of Positive and Negative Trions and the Enhanced Direct Band Emission in MoSe 2 /MoS 2 Heterostacked Multilayers." *ACS Nano*, acsnano.6b02213.

Komsa, H.P. and Krasheninnikov, A. V. (2012). "Effects of confinement and environment on the electronic structure and exciton binding energy of MoS2 from first principles." *Phys. Rev. B - Condens. Matter Mater. Phys.*, 86 (24), 1–6.

Koppens, F.H.L., Mueller, T., Avouris, P., Ferrari, A.C., Vitiello, M.S. and Polini, M. (2014). "Photodetectors based on graphene, other two-dimensional materials and hybrid systems." *Nat. Nanotechnol.*, 9 (10), 780–793.

Kormanyos, A., Z??lyomi, V., Drummond, N.D., Rakyta, P., Burkard, G. and Fal'Ko, V.I. (2013). "Monolayer MoS2: Trigonal warping, the ?? valley, and spin-orbit coupling effects." *Phys. Rev. B - Condens. Matter Mater. Phys.*, 88 (4), 45416.

Kufer, D. and Konstantatos, G. (2015). "Highly Sensitive, Encapsulated MoS2

Photodetector with Gate Controllable Gain and Speed." *Nano Lett.*, 15 (11), 7307–7313.

Lee, C., Yan, H., Brus, L.E., Heinz, T.F., Hone, J. and Ryu, S. (2010). "Anomalous lattice vibrations of single- and few-layer MoS2." *ACS Nano*, 4 (5), 2695–2700.

Lee, C.-H., Lee, G., Zande, A.M. van der, Chen, W., Li, Y., Han, M., Cui, X., Arefe, G., Nuckolls, C., Heinz, T.F., Guo, J., Hone, J. and Kim, P. (2014). "Atomically thin p–n junctions with van der Waals heterointerfaces." *Nat. Nanotechnol.*, 9 (9), 676–681.

Lee, H.S., Min, S.W., Chang, Y.G., Park, M.K., Nam, T., Kim, H., Kim, J.H., Ryu, S. and Im, S. (2012). "MoS 2 nanosheet phototransistors with thickness-modulated optical energy gap." *Nano Lett.*, 12 (7), 3695–3700.

Lee, J., Mak, K.F. and Shan, J. (2015). "Electrical control of the valley Hall effect in bilayer MoS2 transistors." *Nat. Nanotechnol.*, 11 (January), 1–10.

Léonard, F. and Talin, A.A. (2011). "Electrical contacts to one- and two-dimensional nanomaterials." *Nat. Nanotechnol.*, 6 (12), 773–783.

Leong, W.S., Gong, H. and Thong, J.T.L. (2014). "Low-contact-resistance graphene devices with nickel-etched-graphene contacts." *ACS Nano*, 8 (1), 994–1001.

Li, H.-M., Lee, D., Qu, D., Liu, X., Ryu, J., Seabaugh, A. and Yoo, W.J. (2015). "Ultimate thin vertical p-n junction composed of two-dimensional layered molybdenum disulfide." *Nat. Commun.*, 6 6564.

Lin, Y.-C., Lu, N., Perea-Lopez, N., Li, J., Lin, Z., Peng, X., Lee, C.H., Sun, C., Calderin, L., Browning, P.N., Bresnehan, M.S., Kim, M.J., Mayer, T.S., Terrones, M. and Robinson, J.A. (2014). "Direct Synthesis of van der Waals Solids." *ACS Nano*, 8 (4), 3715–3723.

Liu, Y., Wu, H., Cheng, H.C., Yang, S., Zhu, E., He, Q., Ding, M., Li, D., Guo, J., Weiss, N.O., Huang, Y. and Duan, X. (2015). "Toward barrier free contact to molybdenum disulfide using graphene electrodes." *Nano Lett.*, 15 (5), 3030–3034.

Lopez-Sanchez, O., Alarcon Llado, E., Koman, V., Fontcuberta I Morral, A., Radenovic, A. and Kis, A. (2014). "Light generation and harvesting in a van der waals heterostructure." *ACS Nano*, 8 (3), 3042–3048.

Lopez-Sanchez, O., Lembke, D., Kayci, M., Radenovic, A. and Kis, A. (2013). "Ultrasensitive photodetectors based on monolayer MoS2." *Nat. Nanotechnol.*, 8 (7), 497–501.

Lui, C.H., Frenzel, A.J., Pilon, D. V., Lee, Y.H., Ling, X., Akselrod, G.M., Kong, J. and Gedik, N. (2014). "Trion-induced negative photoconductivity in monolayer MoS2." *Phys. Rev. Lett.*, 113 (16), 1–5.

Majumdar, K., Hobbs, C. and Kirsch, P.D. (2014). "Benchmarking transition metal dichalcogenide MOSFET in the ultimate physical scaling limit." *IEEE Electron Device Lett.*, 35 (3), 402–404.

Mak, K.F., He, K., Lee, C., Lee, G.H., Hone, J., Heinz, T.F. and Shan, J. (2013). "Tightly bound trions in monolayer MoS2." *Nat. Mater.*, 12 (3), 207–11.

Mak, K.F., He, K., Shan, J. and Heinz, T.F. (2012). "Control of valley polarization in monolayer MoS2 by optical helicity." *Nat. Nanotechnol.*, 7 (8), 494–498.

Mak, K.F., Lee, C., Hone, J., Shan, J. and Heinz, T.F. (2010). "Atomically thin MoS2: A new direct-gap semiconductor." *Phys. Rev. Lett.*, 105 (13), 136805.

Mak, K.F., McGill, K.L., Park, J. and McEuen, P.L. (2014). "The valley Hall effect in MoS2 transistors." *Science (80-.).*, 344 (6191), 1489–1492.

Massicotte, M., Schmidt, P., Vialla, F., Schädler, K.G., Reserbat-Plantey, a, Watanabe, K., Taniguchi, T., Tielrooij, K.J. and Koppens, F.H.L. (2015). "Picosecond photoresponse in van der Waals heterostructures." *Nat. Nanotechnol.*, 11 (October), 1–6.

Melitz, W., Shen, J., Kummel, A.C. and Lee, S. (2011). "Kelvin probe force microscopy and its application." *Surf. Sci. Rep.*, 66 (1), 1–27.

Molina-Sánchez, A. and Wirtz, L. (2011). "Phonons in single-layer and few-layer MoS2 and WS2." *Phys. Rev. B - Condens. Matter Mater. Phys.*, 84 (15), 155413.

Mouri, S., Miyauchi, Y. and Matsuda, K. (2013). "Tunable photoluminescence of monolayer MoS2 via chemical doping." *Nano Lett.*, 13 (12), 5944–5948.

Mueller, T., Xia, F. and Avouris, P. (2010). "Graphene photodetectors for high-speed optical communications." *Nat. Photonics*, 4 (5), 297–301.

Navarro-Moratalla, E. and Jarillo-Herrero, P. (2016). "Two-dimensional superconductivity: The Ising on the monolayer." *Nat. Phys.*, 12 (2), 112–113.

Nipane, A., Karmakar, D., Kaushik, N., Karande, S. and Lodha, S. (2016). "Few-Layer MoS2 p-Type Devices Enabled by Selective Doping Using Low Energy Phosphorus Implantation." *ACS Nano*, 10 (2), 2128–2137.

Padilha, J.E., Peelaers, H., Janotti, A. and Walle, C.G. Van De (2014). "Nature and evolution of the band-edge states in MoS2: From monolayer to bulk." *Phys. Rev. B - Condens. Matter Mater. Phys.*, 90 (20), 1–5.

Pei, J., Yang, J., Xu, R., Zeng, Y.H., Myint, Y.W., Zhang, S., Zheng, J.C., Qin, Q., Wang, X., Jiang, W. and Lu, Y. (2015). "Exciton and Trion Dynamics in Bilayer MoS2." *Small*, 11 (48), 6384–6390.

Popov, I., Seifert, G. and Tom??nek, D. (2012). "Designing electrical contacts to MoS 2 Monolayers: A computational study." *Phys. Rev. Lett.*, 108 (15), 1–5.

Pospischil, A., Furchi, M.M. and Mueller, T. (2014). "Solar-energy conversion and light emission in an atomic monolayer p-n diode." *Nat. Nanotechnol.*, 9 (4), 257–61.

Pradhan, N., Ludwig, J., Lu, Z., Rhodes, D., Bishop, M.M., Thirunavukkuarasu, K., McGill, S., Smirnov, D. and Balicas, L. (2015). "High Photoresponsivity and Short Photo Response Times in Few-Layered WSe $_2$ Transistors." *ACS Appl. Mater. Interfaces*, 150519145403006.

Radisavljevic, B., Radenovic, A., Brivio, J., Giacometti, V. and Kis, A. (2011). "Single-layer MoS2 transistors." *Nat. Nanotechnol.*, 6 (3), 147–50.

Ramasubramaniam, A. (2012). "Large excitonic effects in monolayers of molybdenum and tungsten dichalcogenides." *Phys. Rev. B - Condens. Matter Mater. Phys.*, 86 (11), 115409.

Rathi, S., Lee, I., Lim, D., Wang, J., Ochiai, Y., Aoki, N., Watanabe, K., Taniguchi, T., Lee, G.-H., Yu, Y.-J., Kim, P. and Kim, G.-H. (2015). "Tunable Electrical and Optical Characteristics in Monolayer Graphene and Few-Layer MoS2 Heterostructure Devices." *Nano Lett.*, 15 (8), 10.1021/acs.nanolett.5b01030.

Ross, J.S., Klement, P., Jones, A.M., Ghimire, N.J., Yan, J., Mandrus, D.G., Taniguchi,

T., Watanabe, K., Kitamura, K., Yao, W., Cobden, D.H. and Xu, X. (2014). "Electrically tunable excitonic light-emitting diodes based on monolayer WSe2 p-n junctions." *Nat. Nanotechnol.*, 9 (4), 268–72.

Ross, J.S., Wu, S., Yu, H., Ghimire, N.J., Jones, A.M., Aivazian, G., Yan, J., Mandrus, D.G., Xiao, D., Yao, W. and Xu, X. (2013). "Electrical control of neutral and charged excitons in a monolayer semiconductor." *Nat. Commun.*, 4 1474.

Roy, K., Padmanabhan, M., Goswami, S., Sai, T.P., Kaushal, S. and Ghosh, A. (2013a). "Optically active heterostructures of graphene and ultrathin MoS2." *Solid State Commun.*, 175–176 35–42.

Roy, K., Padmanabhan, M., Goswami, S., Sai, T.P., Ramalingam, G., Raghavan, S. and Ghosh, A. (2013b). "Graphene-MoS2 hybrid structures for multifunctional photoresponsive memory devices." *Nat. Nanotechnol.*, 8 (11), 826–830.

Sarkar, D., Xie, X., Kang, J., Zhang, H., Liu, W., Navarrete, J., Moskovits, M. and Banerjee, K. (2015). "Functionalization of transition metal dichalcogenides with metallic nanoparticles: Implications for doping and gas-sensing." *Nano Lett.*, 15 (5), 2852–2862.

Shih, C.J., Wang, Q.H., Son, Y., Jin, Z., Blankschtein, D. and Strano, M.S. (2014). "Tuning on-off current ratio and field-effect mobility in a MoS 2-graphene heterostructure via schottky barrier modulation." *ACS Nano*, 8 (6), 5790–5798.

Shimazaki, Y., Yamamoto, M., Borzenets, I. V., Watanabe, K., Taniguchi, T. and Tarucha, S. (2015). "Generation and detection of pure valley current by electrically induced Berry curvature in bilayer graphene." *Nat. Phys.*, 11 (12), 1032–1036.

Splendiani, A., Sun, L., Zhang, Y., Li, T., Kim, J., Chim, C.Y., Galli, G. and Wang, F. (2010). "Emerging photoluminescence in monolayer MoS2." *Nano Lett.*, 10 (4), 1271–1275.

Sun, Z. and Chang, H. (2014). "Graphene and graphene-like two-dimensional materials in photodetection: Mechanisms and methodology." *ACS Nano*, 8 (5), 4133–4156.

Sze, S.M., D. J. Coleman, J.R. and Loya, A. (1971). "Current transport in metal-semiconductor-metal(MSM) structures." *Sol. Stat. Electron.*, 14 1209–1218.

Tersoff, J. and Hamann, D. (1983). "Theory and application for the scanning tunneling

microscope." *Phys. Rev. Lett.*, 50 (25), 1998.

Tielrooij, K.J., Massicotte, M., Piatkowski, L., Woessner, a, Ma, Q., Jarillo-Herrero, P., Hulst, N.F. van and Koppens, F.H.L. (2015). "Hot-carrier photocurrent effects at graphene-metal interfaces." *J. Phys. Condens. Matter*, 27 (16), 164207.

Tosun, M., Fu, D., Desai, S.B., Ko, C., Kang, J.S., Lien, D.-H., Najmzadeh, M., Tongay, S., Wu, J. and Javey, A. (2015). "MoS2 Heterojunctions by Thickness Modulation." *Sci. Rep.*, 5 10990.

Tsai, D.S., Lien, D.H., Tsai, M.L., Su, S.H., Chen, K.M., Ke, J.J., Yu, Y.C., Li, L.J. and He, J.H. (2014). "Trilayered MoS2 metal -Semiconductor-metal photodetectors: Photogain and radiation resistance." *IEEE J. Sel. Top. Quantum Electron.*, 20 (1), 30–35.

Wang, J.I.J., Yang, Y., Chen, Y.A., Watanabe, K., Taniguchi, T., Churchill, H.O.H. and Jarillo-Herrero, P. (2015). "Electronic transport of encapsulated graphene and WSe2 devices fabricated by pick-up of prepatterned hBN." *Nano Lett.*, 15 (3), 1898–1903.

Wang, Q.H., Kalantar-Zadeh, K., Kis, A., Coleman, J.N. and Strano, M.S. (2012a). "Electronics and optoelectronics of two-dimensional transition metal dichalcogenides." *Nat. Nanotechnol.*, 7 (11), 699–712.

Wang, R., Ruzicka, B.A., Kumar, N., Bellus, M.Z., Chiu, H.Y. and Zhao, H. (2012b). "Ultrafast and spatially resolved studies of charge carriers in atomically thin molybdenum disulfide." *Phys. Rev. B - Condens. Matter Mater. Phys.*, 86 (4), 1–5.

Wi, S., Kim, H., Chen, M., Nam, H., Guo, L.J., Meyhofer, E. and Liang, X. (2014). "Enhancement of photovoltaic response in multilayer MoS2 induced by plasma doping." *ACS Nano*, 8 (5), 5270–5281.

Wickramaratne, D., Zahid, F. and Lake, R.K. (2014). "Electronic and thermoelectric properties of few-layer transition metal dichalcogenides." *J. Chem. Phys.*, 140 (12), .

Wu, C.C., Jariwala, D., Sangwan, V.K., Marks, T.J., Hersam, M.C. and Lauhon, L.J. (2013). "Elucidating the photoresponse of ultrathin MoS2 field-effect transistors by scanning photocurrent microscopy." *J. Phys. Chem. Lett.*, 4 (15), 2508–2513.

Wu, J., Schmidt, H., Amara, K.K., Xu, X., Eda, G. and Ozyilmaz, B. (2014). "Large thermoelectricity via variable range hopping in chemical vapor deposition grown single-

layer MoS2." *Nano Lett.*, 14 (5), 2730–2734.

Xia, F., Perebeinos, V., Lin, Y., Wu, Y. and Avouris, P. (2011). "The origins and limits of metal-graphene junction resistance." *Nat. Nanotechnol.*, 6 (3), 179–184.

Xia, F., Wang, H., Xiao, D., Dubey, M. and Ramasubramaniam, A. (2014). "Two-dimensional material nanophotonics." *Nat. Photonics*, 8 (12), 899–907.

Xiao, D., Liu, G.-B., Feng, W., Xu, X. and Yao, W. (2012). "Coupled Spin and Valley Physics in Monolayers of MoS2 and Other Group-VI Dichalcogenides." *Phys. Rev. Lett.*, 108 (19), 196802.

Xu, Y., Cheng, C., Du, S., Yang, J., Yu, B., Luo, J., Yin, W., Li, E., Dong, S., Ye, P. and Duan, X. (2016). "Contacts between Two- and Three-Dimensional Materials: Ohmic, Schottky, and *p – n* Heterojunctions." *ACS Nano*, acsnano.6b01842.

Yang, L., Majumdar, K., Du, Y., Liu, H., Wu, H., Hatzistergos, M., Hung, P.Y., Tieckelmann, R., Tsai, W., Hobbs, C. and Ye, P.D. (2014a). "High-performance MoS2 field-effect transistors enabled by chloride doping: Record low contact resistance (0.5 kΩ·μm) and record high drain current (460 μa/μm)." *Dig. Tech. Pap. - Symp. VLSI Technol.*, 1–2.

Yang, L., Majumdar, K., Liu, H., Du, Y., Wu, H., Hatzistergos, M., Hung, P.Y., Tieckelmann, R., Tsai, W., Hobbs, C. and Ye, P.D. (2014b). "Chloride molecular doping technique on 2D materials: WS2 and MoS2." *Nano Lett.*, 14 (11), 6275–6280.

Yao, W., Xiao, D. and Niu, Q. (2008). "Valley-dependent optoelectronics from inversion symmetry breaking." *Phys. Rev. B - Condens. Matter Mater. Phys.*, 77 (23), 235406.

Yin, Z., Li, H., Li, H., Jiang, L., Shi, Y., Sun, Y., Lu, G., Zhang, Q., Chen, X. and Zhang, H. (2012). "Single-layer MoS 2 phototransistors." *ACS Nano*, 6 (1), 74–80.

Yoshida, M., Iizuka, T., Saito, Y., Onga, M., Suzuki, R., Zhang, Y., Iwasa, Y. and Shimizu, S. (2016). "Gate-Optimized Thermoelectric Power Factor in Ultrathin WSe2 Single Crystals." *Nano Lett.*, 16 (3), 2061–2065.

Yu, H., Cui, X., Xu, X. and Yao, W. (2015). "Valley excitons in two-dimensional semiconductors." *Natl. Sci. Rev.*, 2 (1), 57–70.

Yu, W.J., Liu, Y., Zhou, H., Yin, A., Li, Z., Huang, Y. and Duan, X. (2013). "Highly efficient gate-tunable photocurrent generation in vertical heterostructures of layered materials." *Nat. Nanotechnol.*, 8 (12), 952–8.

Yuan, H., Wang, H. and Cui, Y. (2015). "Two-dimensional layered chalcogenides: From rational synthesis to property control via orbital occupation and electron filling." *Acc. Chem. Res.*, 48 (1), 81–90.

Zhang, H. (2015). "Ultrathin Two-Dimensional Nanomaterials." *ACS Nano*, 9 (10), 9451–9469.

Zhang, W., Huang, J.K., Chen, C.H., Chang, Y.H., Cheng, Y.J. and Li, L.J. (2013). "High-gain phototransistors based on a CVD MoS2 monolayer." *Adv. Mater.*, 25 (25), 3456–3461.

Zhang, Y., Li, H., Wang, L., Wang, H., Xie, X., Zhang, S.-L., Liu, R. and Qiu, Z.-J. (2015). "Photothermoelectric and photovoltaic effects both present in MoS2." *Sci. Rep.*, 5 7938.

Zhang, Y.J., Oka, T., Suzuki, R., Ye, J.T. and Iwasa, Y. (2014). "Electrically Switchable Chiral Light- Emitting Transistor." *Science (80-.).*, 344 (April), 1–7.

Publications

1. "**Valley Coherent Hot Carriers and Thermal Relaxation in Monolayer Transition Metal Dichalcogenides**"; Sangeeth Kallatt, Govindarao Umesh, and KausikMajumdar; Journal of Physical Chemistry Letters. DOI: 10.1021/acs.jpclett.6b00759

2. "**Photoresponse of atomically thin MoS_2 layers and their planar heterojunctions;**
Sangeeth Kallatt, Govindarao Umesh, Navakanta Bhat and Kausik Majumdar, Nanoscale, 2016, 8, 15213-15222. DOI: 10.1039/C6NR02828D

Bio data

Sangeeth kallatt

Senior Facility Technologist

Center for nanoscience and engineering

Indian institute of Science

Bangalore- India

sangeeth@cense.iisc.ernet.in

Education:-

July 2013- January 2017 : National Institute of Technology Karnataka, Surathkal, India
Ph.D., "**Optoelectronic devices with 2D materials"**

August 2007- September 2008 : Annamalai University, Tamil nadu, India
M.Phil in Physics

November 2006 : University of Calicut, Kerala, India
M.Sc in Physics

Research Experience:-

November 2008- March 2012 : Facility technologist, Center for nanosicence and Eng.
Indian Institute of Science, Bangalore- India

March 2012- Till date : Senior Facility technologist, Center for nanosicence and Eng.
Indian Institute of Science, Bangalore- India

Publications:-

Peer reviewed:-

Sangeeth Kallatt, G Umesh, Kausik Majumdar; "Valley-Coherent Hot Carriers and Thermal Relaxation in Monolayer Transition Metal Dichalcogenides ", The journal of physical chemistry letters 7 (11), 2032-2038

Sangeeth Kallatt, G Umesh, N Bhat, Kausik Majumda, "Photoresponse of atomically thin MoS 2 layers and their planar heterojunctions", Nanoscale 8 (33), 15213-15222

Palash Kumar Basu, Samantha Benedict, **Sangeeth Kallatt**, Navakanta bhat Bhat; "A Suspended Low Power Gas Sensor with In-Plane Heater", Journal of Microelectromechanical Systems 2016

Palash Kumar Basu, **Sangeeth Kallatt**, EA Anumol, Navakanta Bhat, "Suspended core-shell Pt-PtOx nanostructure for ultrasensitive hydrogen gas sensor" , Journal of Applied Physics 117 (22), 224501

Kausik Majumdar, **Sangeeth Kallatt**, Navakanta Bhat, "High field carrier transport in graphene: Insights from fast current transient", Applied Physics Letters 101 (12), 123505

Prasanth Kumar, **Kallatt Sangeeth**, "Chromium nanowires grown inside lithographically fabricated U-trench templates", Nanoscience and Nanotechnology Letters 3 (5), 643-647

Prasanth Kumar, **Kallatt Sangeeth**, "Electric Breakdown Between Nanogap Separated Platinum Electrodes", Nanoscience and Nanotechnology Letters 1 (3), 194-198

Conference proceedings:-

Sangeeth Kallatt, Smitha Nair, MN Vijayaraghavan, N Bhat," Gold Catalyzed Plasma Assisted Growth of Germanium Nanoneedles", Physics of Semiconductor Devices, 713-716

Kallatt Sangeeth, GM Hegde, "Fabrication and characterization of sub 100 nm period polymer gratings for photonics applications", CURRENT SCIENCE 107 (5), 749-752

KS Nagaraj, **Kallatt Sangeeth**, GM Hegde, "Nanostructure patterning on flexible substrates using electron beam lithography , International Conference on Experimental Mechanics 2013 and the Twelfth Asian Conference on Experimental Mechanics

BR Deepu, **Sangeeth Kallatt**, A Suresh, P Savitha, "Metal-assisted chemical vertical etching of Si: Effect of catalyst morphology and oxidant concentration", Emerging Electronics (ICEE), 2014 IEEE 2nd International Conference on, 1-3